DEPARTMENT OF ELECTRICAL AND COMPUTER ENGINEERING
UNIVERSITY OF CYPRUS

OPTOELECTRONIC CHARACTERIZATION AND LUMINESCENT COUPLING EFFECTS IN MULTI-JUNCTION SOLAR CELLS

VASILIKI PARASKEVA

A dissertation submitted to the University of Cyprus in partial fulfillment of the requirements for the degree of doctor of philosophy

January 2017

VALIDATION PAGE

Doctoral Candidate: **Vasiliki Paraskeva**

Doctoral Thesis Title: **Optoelectronic Characterization and Luminescent Coupling Effects in Multi-junction Solar Cells.**

The present Doctoral Dissertation was submitted in partial fulfillment of the requirements for the degree of Doctor of Philosophy at the ***Department of Electrical and Computer Engineering*** *and was approved on the 18th of January 2017 by the members of the* ***Examination Committee.***

Examination Committee:

Research Supervisor:

Prof. George Georghiou

Committee Chair:

Prof. Julius Georgiou

Committee Member:

Prof. Ned Ekins-Daukes

Committee Member:

Prof. Andreas Othonos

Committee Member:

Prof. Marcos Antoniades

DECLARATION OF DOCTORAL CANDIDATE

The present doctoral dissertation was submitted in partial fulfillment of the requirements for the degree of Doctor of Philosophy of the University of Cyprus. It is a product of original work of my own, unless otherwise mentioned through references, notes, or any other statements.

Vasiliki Paraskeva [Full Name of Doctoral Candidate]

……..[Signature]

Abstract (in English language)

Over the past years, photovoltaic (PV) technology has shown rapid development. First generation solar cells which are based on Silicon technology are approaching their efficiency limit. The solution to overcome Shockely-Quesisser limit is the use of new materials concepts such as multi-junction solar cells.

The motivation behind this work and hence its contribution is to determine and improve the characterization conditions for multi-junction solar cells as well as to examine radiative losses in these cells by utilizing several optoelectronic methods. The direct measurement of radiative losses of multi-junction solar cells under a high concentration solar spectrum has not been achieved so far and is needed to improve our understanding of the luminescent emission under actual operating conditions as well as to provide cell designers with an additional tool with which to optimise their device performance. In addition, one of the main aims of the thesis is to provide an insight into unexplored areas associated with those devices such as coupling effects. Such effects could have significant influence on the performance and in particular on the annual energy yield of the solar cells and merits investigation. The impact of shunt resistance, temperature and material design on coupling effects was investigated demonstrating which operating conditions and material structure enhance coupling effects. Another main topic investigated in the framework of the thesis is the examination of the impact of the spectral response of multi-junctions on the long term energy yield of the devices and how the customization of the spectral response of a cell can be advantageous for the performance of the cell.

Due to the series connection of junctions, the External Quantum Efficiency (EQE) measurement of multi-junction solar cells presents additional challenges compared to EQE measurement procedures for single junction ones. This work contributed to the improvement of multi-junction device characterization by reporting the effects of low and high shunt resistance

junctions on EQE for various voltage and light bias conditions. Luminescent coupling effects were then studied. Since most of the effects of luminescent coupling remain unexplored, an investigation of the material properties and operating conditions which enhance coupling is of major importance. Excitation and voltage dependent Photoluminescence (PL) measurements have been carried out at different shunt resistance and structure materials and at different temperatures in order to demonstrate their impact on coupling effects. Subsequently, Electroluminescence (EL) and Photoluminescence (PL) measurements were conducted in order to investigate the presence of luminescent emission of InGaP/InGaAs/Ge at different operating conditions of the tandem. The investigation is essential since it indicates the radiative losses in multi-junction solar cells under concentrated spectrum conditions and provides an indication about the losses apparent at real outdoor testing conditions. Apart from indoor characterization, outdoor investigation of the electrical properties of multi-junction devices has been performed to gain knowledge on multi-junction solar cell performance under outdoor field conditions and to investigate the impact of spectral sensitivity of the cells on the operating efficiencies in the field. Due to the existence of several p-n junctions in a multi-junction device the devices are spectrally sensitive and any changes to their spectral response and spectrum of the testing location can lead to changes in the annual energy yield.

Abstract (in Greek language)

Κατά την διάρκεια των περασμένων ετών, τα φωτοβολταϊκά έχουν επιδείξει μια ραγδαία εξέλιξη και ένα ευρύ φάσμα τεχνολογιών έχει αναδυθεί από τους κατασκευαστές. Τα φωτοβολταϊκά πρώτης γενεάς που βασίζονται στην τεχνολογία πυριτίου έχουν φτάσει στο μέγιστο όριο απόδοσης. Η λύση για την υπέρβαση του ορίου απόδοσης (Shockely-Quesisser limit) είναι η χρήση καινούριων δομών για φωτοβολταικά όπως είναι τα φωτοβολταϊκά πολλαπλών επαφών.

Το κίνητρο για την ετοιμασία αυτής της δουλειάς και συνεπώς η συνεισφορά της ήταν να βελτιώσει και να καθορίσει τις συνθήκες χαρακτηρισμού για τα φωτοβολταϊκά πολλαπλής επαφής καθώς και να μελετήσει τις απώλειες εκπομπής σ' αυτά τα φωτοβολταϊκά με διάφορες οπτοηλεκτρονικές μεθόδους. Η απευθείας μέτρηση των απωλειών εκπομπής κάτω από το ηλιακό φάσμα σε τέτοιου είδους συσκευές δεν έχει επιτευχθεί μέχρι στιγμής και είναι απαραίτητη για να βελτιώσει την κατανόηση μας σε θέματα ακτινοβολούσας εκπομπής κάτω από πραγματικές συνθήκες λειτουργίας όπως επίσης και να παρέχει στους κατασκευαστές φωτοβολταϊκών πληροφορίες που μπορούν να βελτιώσουν την απόδοση της συσκευής. Επιπρόσθετα, ένας από τους κύριους στόχους αυτής της μελέτης είναι να εξερευνήσει καινούρια φαινόμενα που παρουσιάζουν τα φωτοβολταϊκά πολλαπλής επαφής όπως είναι οι οπτικές αλληλεπιδράσεις μεταξύ των επαφών. Αυτά τα φαινόμενα μπορούν να έχουν σημαντική επίδραση στην ενεργειακή απόδοση των φωτοβολταϊκών και συνεπώς στην ολική ετήσια απόδοση τους γι' αυτό και αξίζουν διερεύνησης. Η επίδραση της παράλληλης αντίστασης, της θερμοκρασίας και του σχεδιασμού του ηλιακού κυττάρου στις οπτικές αλληλεπιδράσεις έχει διερευνηθεί επιδεικνύοντας ποιες συνθήκες λειτουργίας και παράμετροι σχεδιασμού ευνοούν τις οπτικές αλληλεπιδράσεις. Ένα άλλο κύριο ζήτημα που διερευνήθηκε στα πλαίσια αυτής της μελέτης είναι η επίδραση της διαφορετικής φασματικής απόκρισης των φωτοβολταϊκών κυψελίδων στην ετήσια απόδοσης τους και πως η εναρμόνιση της φασματικής απόκρισης μπορεί να αποτελέσει πλεονέκτημα για την απόδοση του φωτοβολταϊκού.

Εξαιτίας της σειριακής σύνδεσης των επαφών, οι μετρήσεις της κβαντικής απόδοσης των φωτοβολταϊκών πολλαπλής επαφής παρουσιάζουν επιπρόσθετες προκλήσεις σε σχέση με τις μετρήσεις απόδοσης των φωτοβολταϊκών μίας επαφής. Η δουλειά αυτή βοήθησε στην βελτίωση του χαρακτηρισμού των φωτοβολταϊκών πολλαπλής επαφής με την παρουσίαση της επίδρασης της χαμηλής και ψηλής παράλληλης αντίστασης των φωτοβολταϊκών στις μετρήσεις κβαντικής απόδοσης για διαφορετικές συνθήκες φωτός και τάσης. Μελέτη των οπτικών αλληλεπιδράσεων μεταξύ των επαφών έχει επίσης πραγματοποιηθεί. Καθώς τα πλείστα αποτελέσματα των οπτικών αλληλεπιδράσεων είναι άγνωστα, η μελέτη των μεταλλικών ιδιοτήτων και συνθηκών λειτουργίας που ευνοούν τις οπτικές αλληλεπιδράσεις είναι εξαιρετικής σημασίας. Για το σκοπό αυτό μετρήσεις φωτοφωταύγειας σε διαφορετικές εντάσεις φωτός και δυναμικού έχουν πραγματοποιηθεί σε υλικά InGaP/InGaAs/Ge. Φωτοβολταϊκά με διαφορετικές παραμέτρους σχεδιασμού και διαφορετικής ποιότητας έχουν χρησιμοποιηθεί για να καταδείξουν την επίδραση του σχεδιασμού του ηλιακού κυττάρου και της ποιότητας του στις οπτικές αλληλεπιδράσεις μεταξύ των επαφών. Επιπρόσθετα η επίδραση της θερμοκρασίας στις οπτικές αλληλεπιδράσεις μεταξύ των επαφών έχει μελετηθεί. Επιπλέον, χαρακτηρισμός των φωτοβολταϊκών με οπτοηλεκτρονικές μεθόδους όπως η φωτοφωτάυγεια και η ηλεκτροφωταύγεια έχει γίνει με σκοπό την μελέτη των απωλειών επανασύνδεσης και την εκπομπή των φωτοβολταϊκών πολλαπλής επαφής. Η διερεύνηση αυτή είναι πολύ σημαντική καθώς επιδεικνύει τις απώλειες εκπομπής στα φωτοβολταϊκά πολλαπλής επαφής κάτω από το ηλιακό φάσμα συγκεντρώσεως και δίνει ενδείξεις για τις απώλειες που εμφανίζονται κάτω από πραγματικές συνθήκες λειτουργίας. Εκτός από τον εσωτερικό χαρακτηρισμό, μελέτη των ηλεκτρικών ιδιοτήτων των φωτοβολταϊκών πολλαπλής επαφής έχει πραγματοποιηθεί σε εξωτερικές συνθήκες με στόχο την μελέτη της απόδοσης τους σε πραγματικές συνθήκες λειτουργίας καθώς επίσης και την διερεύνηση της επίδρασης της φασματικής απόκρισης στην απόδοση τους. Εξαιτίας της ύπαρξης πολλών επαφών στα κελλιά πολλαπλής επαφής, οι συσκευές είναι φασματικά πιο ευαίσθητες και οποιαδήποτε αλλαγή στο φάσμα ή στην φασματική τους απόκριση μπορεί να έχει τεράστιες επιπτώσεις στην ετήσια ενεργειακή απόδοση των συσκευών.

Table of Contents

List of Figures

List of Tables

Nomenclature

Abbreviations

µc-Si	Microcrystalline Silicon
AC	Alternative current
AM	Air Mass
As	Arsenide
ASTM	American Standard for Testing and Materials
CCD	Charge-Coupled Device
CPV	Concentrating Photovoltaic
c-Si	Crystalline Silicon
CSOC	Concentrator Standard Operating Conditions
DC	Direct current
DNI	Direct Normal Irradiance
EL	Electroluminescence
EQE	External Quantum Efficiency
FF	Fill Factor
Ga	Gallium
Ge	Germanium
GNI	Global Normal Irradiance
In	Indium
I-V	Current-Voltage
LM	Lattice Matched
MOCVD	Metalorganic Vapor Deposition
MPP	Maximum Power Point
NIR	Near Infrared Region
NIST	National Institute of Standards and Technology
NOCT	Nominal Operating Cell Temperature
P	Phosphide
PL	Photoluminescence
PR	Performance Ratio
PV	Photovoltaics
Si	Silicon
SMARTs	Simple Model of the Atmospheric Transfer of Sunshine
SR	Spectral Response
STC	Standard Test Conditions

UCY	University of Cyprus
UMM	Upright Metamorphic
UV	Ultraviolet
VIS	Visible

Chapter 1

Introduction

1.1 Introduction

Concentrating photovoltaic (CPV) systems use optics such as lenses or mirrors to concentrate sunlight onto highly efficient PV cells. The higher the level of concentration the less semiconductor material is required to harvest the same amount of power. CPV is an emerging technology, with a small market share, but with very promising potential in locations with high direct normal irradiance (DNI).

CPV systems often use very efficient multi-junction devices for solar energy conversion, by utilizing a wider range of the solar spectrum. The basic concept behind such devices is that multiple band-gaps are created within one semiconductor material and the interconnection is provided by tunneling junctions between each pair of subcells. The most popular multi-junction device for CPV applications is the triple-junction structure InGaP/InGaAs/Ge. The semiconductors used in this particular device are made from III-V materials. The latest multi-junction solar cells incorporating four active junctions have recently demonstrated conversion efficiencies in excess of 46% [1].

As such devices continue to set conversion efficiency records there is growing interest in the characterization methods employed for them as well as the radiative losses and recombination processes present. In depth and reliable characterization of such devices is required to gain further knowledge about their properties which can lead to energy yield improvements. The existence of only two terminals in the multi-junction devices makes characterization of each

junction in the tandem difficult to achieve. One of the most common characterization methods of PV cells is External Quantum Efficiency (EQE) which is a conceptually similar term to Spectral Response (SR). Due to the existence of two terminals in a multi-junction device, accurate SR measurements of each junction in the tandem are not a trivial task. In order to examine the conditions where correct SR results from each junction can be obtained in this work, SR was performed at different voltage-light bias conditions. With the use of the aforementioned method, the appropriate conditions that should be present during SR testing were extracted.

Optical interactions between junctions also known as coupling effects were also investigated. Since most of the effects of coupling are unexplored, Photoluminescence (PL) measurements were conducted at different shunt resistance and structure materials as well as at different temperatures in order to investigate coupling. Furthermore, apart from SR and PL, Electroluminescence (EL) measurements were performed in order to investigate radiative losses in multi-junction devices and gain knowledge on how those affect device performance. Significant radiative losses in multi-junction devices can lead to absorption of photons from the bottom junctions and thus coupling effects. Therefore, investigation of the radiative losses can provide an insight into the potential presence of coupling under field conditions. The various characterization methods used are required for the better understanding of material properties and will facilitate new approaches towards the improvement of the design of the particular device structures.

Finally, outdoor monitoring of different technology multi-junction devices was carried out in an attempt to investigate their performance under field conditions. Outdoor results demonstrated for the first time the relative advantages of each cell design and also the impact of SR on the energy yield of multi-junction devices. Therefore variation of the SR of each junction could be quite important for the energy yield improvement of multi-junction devices. In the next subsection the motivation and the objectives as well as the novelty of the work are given in detail.

1.2 Motivation and Objectives

The material properties of multi-junction devices are not yet well known and study of the properties of the optical transitions through various characterization methods will provide a better understanding of the materials and optical interactions between junctions. Therefore, advanced characterization techniques are required in order to enhance our understanding on the quality and thus efficiency of such multi-junction devices. Due to the presence of only two terminals in multi-junction devices the junctions are not accessible separately and thus the SR measurements of those cells present additional challenges compared to the measurement procedure for single junction devices. In the absence of a dedicated international standard procedure for SR measurements of multi-junction devices, appropriate guidelines for the measurement procedure should be developed. Furthermore, a full explanation about the measurement artifacts that occur during the SR procedure is still missing and is very much needed. For this purpose, SR measurements were performed at different voltage-light conditions and the appropriate conditions that should be present during SR measurements were extracted.

The junctions in a multi-junction device are coupled electrically and optically. Since most of the multi-junction devices are made of III-V materials where radiative recombination is the dominant carrier recombination mechanism, optical interactions also known as luminescent coupling effects are expected to have a considerable impact on the electrical properties of III-V devices. Many of the factors that might have significant influence on the effect are still unclear and an extensive investigation of the phenomenon is required in an attempt to gain an understanding about the impact of this effect on the device performance and to find ways to optimize device design taking into account coupling effects. Coupling effects dependence on shunt resistance, material structure, light intensity and temperature are studied and discussed in detail in the thesis.

The presence of coupling effects is strongly related with the radiative recombination of junctions. Higher radiative recombination means more photons extracted from the tandem which thus enhances the probability of absorption of photons from the lower junctions and coupling in the tandem. In an attempt to investigate that possibility, examination of luminescent

emission in multi-junction devices via EL and PL was performed. Investigation of radiative losses in tandem devices is required for the understanding of the impact of losses on the cell operation which consequently can lead to optimization of the material design for maximum efficiency. In order to investigate radiative losses at different operating conditions the luminescent emission was measured using a high intensity solar simulator at different voltage biases, light intensities and temperatures. The comprehensive study of the properties of the optical transitions in multi-junction solar cells and their dynamic processes provided a better understanding of their fundamental optical properties and facilitated new approaches towards the improvement of material quality of particular device structures.

Finally, apart from indoor tests, outdoor investigation of electrical properties of multi-junction devices was performed in an attempt to gain knowledge on multi-junction solar cells performance under outdoor field conditions. This is an important topic in the performance assessment of CPV technologies especially for the novel ones. Outdoor results are essential to further develop our understanding of how differently PV technologies perform under real operating conditions and also to find the spectral response impact on the multi-junction energy yield.

In this work the above mentioned research topics were investigated in order to enhance our knowledge in the field of indoor and outdoor characterization of multi-junction PV cells. SR, EL and PL methods were used for the indoor characterization of cells while continuous outdoor monitoring and evaluation of the energy yield of different CPV cells was carried out.

1.3 Novelty

The optimum voltage-light conditions during SR testing of multi-junction devices are still not well defined. In this work the impact of voltage and light on SR measurements is investigated and ideal conditions that should be present during measurements are demonstrated. Particularly, measurements have been contacted at different light bias intensity and voltage in order to demonstrate the appropriate conditions that should exist during the characterization of each junction in the tandem device.

During SR measurements, luminescent coupling effects were detected. Optical interactions between junctions in a tandem device are quite important for the operation of the cell because they affect the main parameters of the PV cell during operating conditions. Since limited knowledge exists so far about coupling effects, investigation of several parameters that affect coupling is required. The impact of shunt resistance, material structure and temperature on coupling effects is demonstrated for the first time. Specifically coupling effects were studied in different material PV cells and at different temperatures in order to show the type of material and temperature conditions that enhance coupling. The results encountered are of major importance for the cell designers in order to take into consideration the impact of coupling on cell design.

Investigation of radiative losses of multi-junction devices through the examination of luminescent emission under a high intensity solar simulator was considered. The resulting measurements are quite important because radiative losses have a significant impact on the solar cell efficiency and also provide an indication about the presence of radiative losses under outdoor operating conditions.

Since multi-junction cells appear with increased spectral sensitivity, questions arise about the impact of spectral response of the cells upon their operating efficiencies and how the optimization of cell spectral response can improve energy yields. Customizing the spectral response of a cell maybe advantageous for outdoor application and this merits investigation. For this reason, outdoor assessment of different multi-junction cell designs has been considered to investigate the influence of the spectral response of multi-junction PV cells on the energy yield.

1.4 Outline of the proposal

The proposal is divided and organized in 6 chapters. Specifically, chapter 1 is the introduction and includes the motivation, novelty and research objectives of the work. Chapter 2 provides knowledge on the ideal conditions that should exist during SR measurements of multi-junction solar cells in order to minimize the measurement artifacts. Chapter 3 presents the investigation of the optical interaction between junctions (coupling effects). The impact of shunt resistance,

material structure and temperature on coupling effects has been examined. Radiative losses of multi-junction devices using combined EL and PL methods are presented in Chapter 4. Apart from indoor testing, outdoor monitoring of different technology devices is presented in Chapter 5. Chapter 6 contains the conclusions with the summary of the thesis achievements so far and plans for future work. The state of the art in each of the four main research topics is outlined in the respective chapters.

Chapter 2

Spectral response (SR) measurements

2.1 Introduction

The idea of multi-junction devices seems to have been first suggested in 1955 by AD Jackson [2]. However, it was not until 1978 that this idea was first demonstrated experimentally by Moon et al [3] with an efficiency of 28.5% measured in outdoor sunlight using a 17 layer dichroic reflector stack to steer the light of energy 1.65 eV onto an AlGaAs cell and below 1.65 eV onto a Silicon cell.

In spectral response measurements of multi-junctions, the incoming energy spectrum is splitting into multiple segments each of which are treated separately to enable more efficient collection. The junctions have to be stacked in order of descending band-gap since each material is only transparent to those photons with energies less than the band-gap. Therefore, the top material absorbs the highest energy photons. A schematic demonstrating the improvement of solar energy collection is depicted in Figure 1.

The SR or EQE of a PV device is a valuable parameter and is required to calculate the spectral mismatch between the standard reference spectrum and the actual spectral irradiance of the light source in use. This correction can be particularly important for indoor measurements of multi-junction devices on single lamp solar simulators. Due to the series connection of junctions in a tandem, an accurate value of the SR of each junction is difficult to find due to measurement artifacts present during the procedure. These measurement artifacts arise from the inappropriate light and voltage conditions. The main aim of this chapter is to present the ideal

conditions that should exist during SR measurements that minimize the measurement artifacts and give the correct SR values from the junctions. The ideal conditions for SR testing are required for the correct characterization of the material. In an attempt to find the appropriate measurement conditions, the devices were tested at several light and voltage conditions. The results at the different measurement conditions are presented and discussed in detail in this chapter.

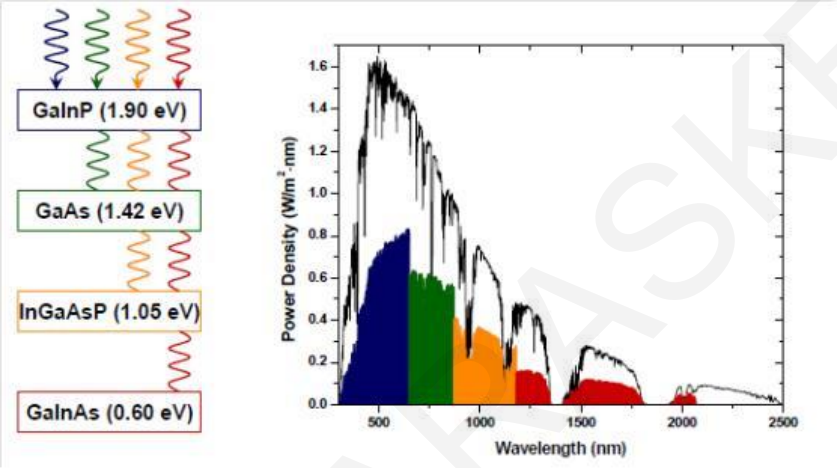

Figure 1: Schematic of the photons that are absorbed in a proposed four junction solar cell (left) and a plot showing the solar spectrum (in black) and the power converted by each of the four junctions (the shaded area) (right). The maximum theoretical efficiency of this device is 55%.

2.2 Equations and definitions

The SR measurement technique is a very useful tool for characterizing a solar cell and through this method the quality of the tested cell can be obtained. Mainly SR describes the sensitivity of the solar cell to optical radiation of different wavelength and is defined by the following (2.1):

$$SR(\lambda) = \frac{I_{sc}(\lambda)}{E(\lambda)} \tag{2.1}$$

where I_{sc} is the short-circuit photogenerated current density of the tested device under spectral irradiance $E(\lambda)$ (in $W/m^2.nm$) and in the wavelength band between λ and $\lambda+\delta\lambda$ (in nm).

The SR is conceptually similar to the external quantum efficiency (EQE). The EQE is defined as the number of measured electrons divided by the number of photons incident on the cell. The relation between the two quantities is given by (2.2):

$$SR(\lambda) = \frac{q\lambda}{hc} EQE(\lambda) \tag{2.2}$$

where q is the electron charge, λ is the wavelength, h is Planck's constant and c is the speed of light. EQE represents the external quantum efficiency. Apart from EQE another type of quantum efficiency exists: the internal quantum efficiency (IQE). The definition of the two types of efficiencies is given by (2.3) and (2.4):

$$EQE = \frac{number\ of\ measured\ carriers}{incident\ photon\ number} \tag{2.3}$$

$$IQE = \frac{number\ of\ measured\ carriers}{absorped\ photon\ number} \tag{2.4}$$

Conservation law requires EQE (λ) ≤ 1. In terms of SR this limit gives the following restriction to possible SR values:

$$SR(\lambda) \leq \frac{q}{hc}\lambda \tag{2.5}$$

By inverting (2.1) and integrating over all wavelengths, the following useful relation for the short-circuit current results

$$I_{sc} = A \int_{\lambda_{min}}^{\lambda_{max}} SR(\lambda) E(\lambda) d\lambda \tag{2.6}$$

where the integral is performed in the wavelength band where SR(λ) is non-zero. The value of λ_{max} is the absorption cut-off of the PV device under examination and is determined by its band gap.

2.3 State of the art

The procedure for measuring the SR of a single-junction PV cell is described in the International Standard IEC 60904-8 "Measurement of a spectral response of a photovoltaic (PV) device" [4] and in the American Standard Test Procedure ASTM E2236-10 [5]. The two procedures are based on the differential spectral responsivity method. Possible sources of uncertainties in determining the absolute SR of a test device are well described in the cited standards and in [6]. In a two-terminal multi-junction PV device due to the series connection of the component junctions, the total incoming spectral irradiance determines which junction limits the total photogenerated current. The method of measuring the SR of a single-junction PV cell described in the previous section is used to determine the SR of the current-limiting junction in the device. For a single-junction device due to the single band-gap nature of the device current limitation is not an issue. However, in multi-junction solar cells in order to measure the SR of the current limiting junction, bias light is necessary to saturate the junctions not under examination. This was first proposed by Burdick and Glatfelter in 1986 [7] during the SR procedure of a two-junction a-Silicon alloy solar cell. Specifically, the authors suggest the use of an appropriate bias light, which is absorbed mainly by the junctions not under examination so that the current of the entire device is limited and determined by the current-limited junction. An increase in the intensity of this bias light would not produce an increase in the overall current, hence the term "saturation" is used.

SR measurements of a triple-junction a-Si/a-Si/a-Si:Ge device were reported for the first time in 1988 by Emery et al [8]. No international standard procedure currently exists for SR measurement of non-concentrator multi-junction cells but the ASTM standard test method E2236-05 [9] describes the procedure for SR measurements of non-concentrator multi-junction devices and discusses the current balance problem, giving indications on how to perform an appropriate spectral mismatch correction on I-V measurements with both a spectrally adjustable and a non-spectrally adjustable solar simulator.

SR measurements of III-V multi-junction cells with the related measurement artifacts observed during the experiments have been described by Meusel et al [10]. In their paper a detailed measurement procedure is provided. Several improvements have followed that paper [11], [12]

the most recent being the work by Siefer et al [13] which proposes a new procedure for correcting observed measurement artifacts during the SR measurement of the bottom Ge junction in a triple-junction InGaP/InGaAs/Ge device. All the above papers underline the importance of applying voltage bias during the measurement of the bottom Ge junction. The same result has been shown recently by Lim et al [14]. SR dependence on bias voltage in multi-junction amorphous Silicon has also been analyzed by Hibbert et al [15].

Recently Lim et al discovered another source of measurement artifacts during the SR procedure of multi-junction devices arising from significant radiative recombination from the junctions [16]. This phenomenon is referred to as luminescent coupling and can cause reduction of the SR signal in the middle InGaAs and bottom Ge junctions. Combined effects of shunt and luminescent coupling on the SR measurements are presented and discussed in [17]. SR measurements were used to identify and investigate optical coupling in III-V multilayer systems [18]. SR measurements of different surface passivation cells were used to investigate coupling effects at different light bias conditions [19].

The temperature dependence of SR of multi-junction solar cells was discussed by Kinsey and Edmonson [20]. Their results were combined with annual spectral irradiance data, showing that a higher performance may be obtained in CPV if multi-junction cells were designed for an effective air mass (AM), higher than standard AM1.5.

The spectral effects on PV device rating are strictly correlated to SR measurements of PV devices and have been presented in several papers [21]–[23]. Investigation of the correlation of SR and long term energy yield is provided in the next chapters of the thesis. Effects of low shunt resistance on dark SRs have also been observed, explained and discussed in detail in [24]–[27].

Full explanation on the measurement artifacts that appear during SR measurements has not been achieved to date. Furthermore, the ideal conditions for SR measurements have not been demonstrated yet either. For that purpose, a high-resolution SR set-up was developed and SR measurements at different light and voltage bias conditions have been carried out. The measurements have exhibited artifacts and the ideal SR testing conditions for the multi-junction

cells have been proposed. The impact of light and voltage at different shunt resistance junctions has also been examined indicating the necessity of voltage bias during the measurement of a low shunt resistance junction. Detailed description of the developed SR set-up as well as preliminary results taken from the system are discussed in this chapter.

2.4 Experimental set-up

An experimental set-up was implemented at the University of Cyprus in order to perform high resolution SR measurements on small size solar cells and investigate the appropriate conditions during SR testing. The SR set-up consists of a light source, a monochromator, chopper, lenses and lock-in amplifiers. A 100 W Quartz Tungsten Halogen lamp provides the light source that is divided by the monochromator in order to produce the monochromatic light input which is then chopped at 75 Hz superimposed on the continuous bias light and measured by digital lock-in amplifiers. The monochromatic light is separated by a beam splitter and allows simultaneous measurement of a small size monitor device and a reference cell of known absolute SR. The monochromatic light is focused on the surface of the cells with a circular spot of 1.5 mm in diameter. The active area of the reference and monitor devices is around 13 mm^2. The area of the test cells differs from cell to cell but for multi-junction solar cells is approximately around 30 mm^2. Low-pass filters are used with a cut-off wavelength of 920 nm and 1020 nm to avoid second order effects. Second order effects are signals produced by lower wavelengths and are apparent above 900 nm. Plano-convex lenses are located between the beam splitter and the sample in order to focus the light onto the cells. The test, monitor and reference cell are kept stable at room temperature. Test, monitor and reference cell currents are measured over load resistors of appropriate (very small) values in order to maintain the devices close to short-circuit conditions. A four-quadrant source meter is connected in series with the test device in order to provide voltage bias during the SR measurements. The schematic of the set-up is depicted in Figure 2.

In the case of SR measurements in a triple-junction PV device, due to the series connection of the component junctions, the total incoming spectral irradiance determines which junction limits the total photogenerated current. A set of coloured light sources is needed in order to saturate the non-measured junctions and subsequently achieve current limitation by the junction

of interest. In order to separate out the top junction a light bias source must be able to flood the middle and bottom junctions. Thus LEDs in the region of response of middle and bottom junction must be applied on the device. Specifically a red and an IR LED are used for the current limitation of the top junction, a blue and an IR are used for the current limitation of the middle one and finally a blue and a red one are used for the current limitation of the bottom junction. Table 1 shows the possible choice of bias light system for the saturation of each junction in a multi-junction device. The spectrum of the light bias used for the saturation of each junction in a multi-junction device during the SR measurements is given in Figure 3. The manufacturer of the violet (405nm) and green (532nm) LEDs is the Global Laser while the manufacturer of the blue LED (465nm) is ENFIS. The rest of the LEDs in the NIR or IR region have been fabricated by Roithner Lasertechnic.

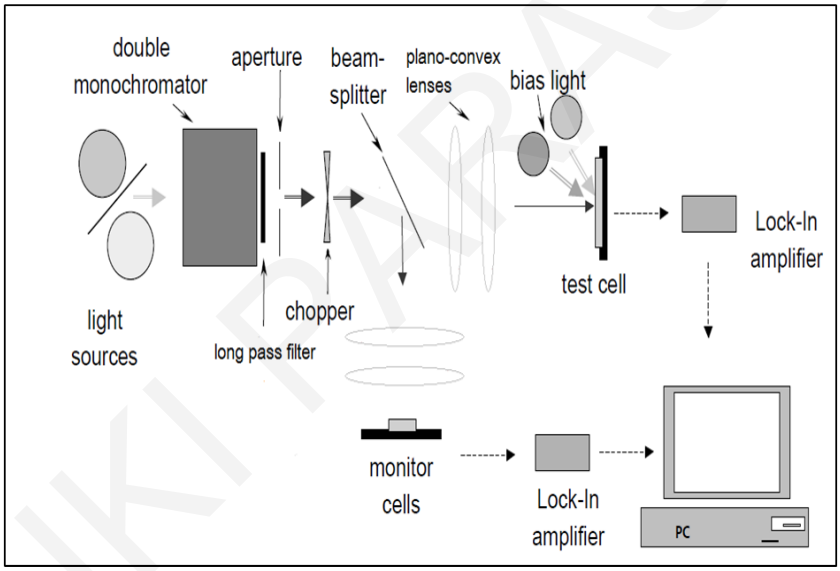

Figure 2: Experimental set-up for SR measurement at the UCY.

Table 1: Approximate region of response of the lamps used for the saturation of each junction in the multi-junction InGaP/InGaAs/Ge device.

Junction	Region of response (nm)	Light bias
InGaP	280-680	LED (405nm, 465nm or 532nm)
InGaAs	550-940	LED (780nm or 808nm)
Ge	870-1800	LED (940nm or 980nm)

The procedure for measuring the SR requires calibration of the system because the actual measurement is essentially a comparison of the test's cell response to a calibrated standard cell's response. Furthermore, the calibration permits a correction for any light intensity change from the time of calibration to the time of actual measurement. To calibrate the spectral response measurement system a reference photovoltaic device is used for which the SR values as a function of wavelength are well known. The reference device used was a NIST traceable calibrated Si photodiode which is sensitive across the visible and into the near infrared spectrum and a Ge photodiode which is sensitive in the near infrared and infrared region. The reference cell is mounted in the position where otherwise the test cell would be located. On the other path a monitor cell is located. Both monitor and reference cell are connected to the lock-in amplifier and the chopper is set to 75 Hz. A labview program initiates the calibration process in which the lock-in amplifier output currents of the reference and monitor cells are measured. From the lock-in output current of the reference and monitor cells at each wavelength, the calculation of the monitor relative SR is performed according to (2.7).

$$SR_{mon} = SR_{ref} \frac{I_{mon}}{I_{ref}} \tag{2.7}$$

Where SR_{mon} and I_{mon} are the spectral response and current of the monitor cell, and SR_{ref} and I_{ref} are the spectral response and current of the reference cell. After the calibration procedure is completed, the SR of the test cell can be measured. The reference cell is removed and replaced by the test cell and the SR of the test cell is calculated from (2.8).

$$SR_{test} = SR_{mon} \frac{I_{test}}{I_{mon}} \tag{2.8}$$

Where SR_{test} and I_{test} are the spectral response and current of the test cell. The wavelength of the incident light is varied from 350 nm to 1800 nm in 10 nm steps for the SR measurement of a triple-junction device and the lock-in amplifier's output is recorded at each step. The process is interrupted at 900 nm where the Silicon photodiode is replaced by the Ge photodiode. The wavelength of the incident light is varied between 350 nm and 1100 nm for the SR measurement of a single Silicon solar cell.

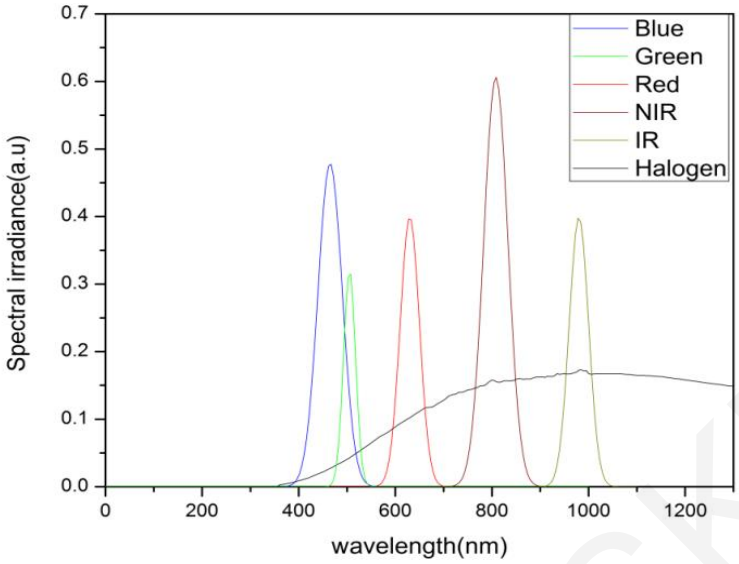

Figure 3: SR measurement set-up: the spectra of the light bias lamps.

2.4.1 Validation of the SR set-up

In order to validate the SR set-up a round robin procedure between the University of Cyprus (UCY) and the University of Applied Sciences and Arts of Southern Switzerland (SUPSI) was performed using c-Si CPV cells. Several cells were tested and measured with the SR set-up and their responses were compared with those found in SUPSI. Figure 4 shows the comparison between the results. A good agreement between the results was observed. Less than 2% relative deviations were found in the range 500-1000 nm and less than 5% elsewhere.

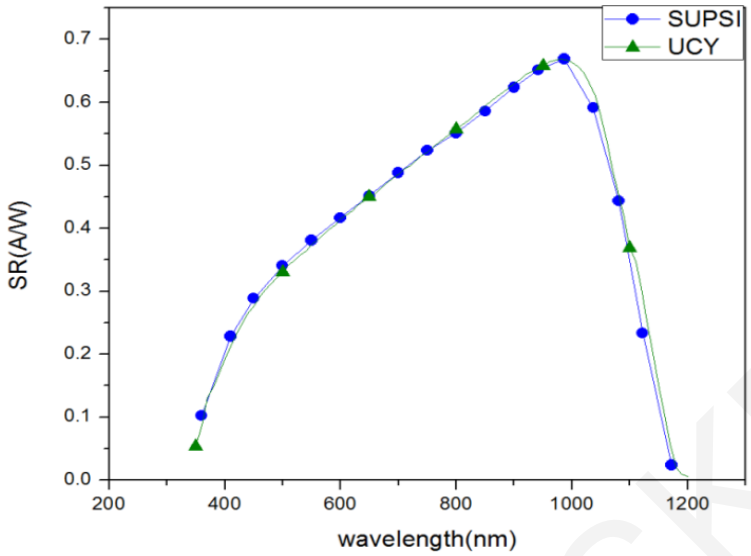

Figure 4: Comparison between SR measurements at SUPSI (blue line) and at UCY (green line).

Furthermore, a comparison between the UCY SR measurements and the SR measurements from the Institute of Physical Electronics in Stuttgart (IPE) was also carried out (Figure 5). These results indicated around 2% difference between SR data demonstrating that the set-up works reasonably well and thus can be used for testing.

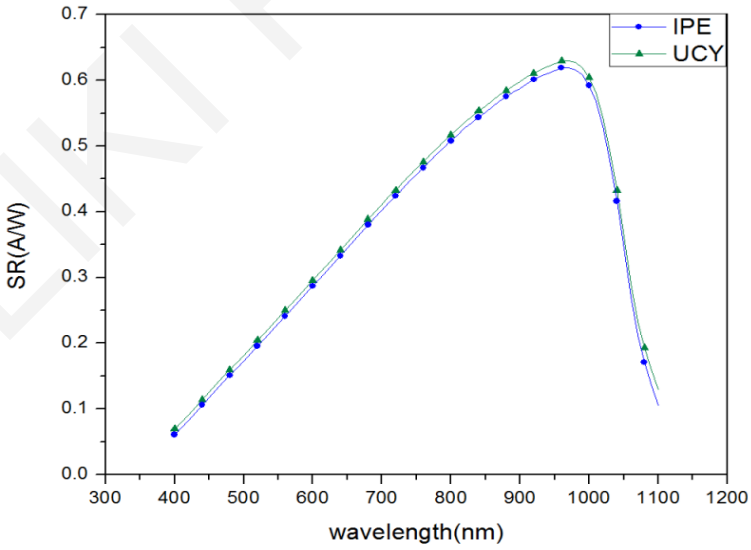

Figure 5: Comparison between SR measurement at IPE (blue line) and UCY (green line).

2.5 EQE measurements-Infinite/finite shunt resistance approximation

Before presenting the EQE measurements of each junction in the multi-junction device at different voltage-light bias conditions, it is important to present how the EQE signal is affected by low or high shunt resistance junctions. The value of the shunt resistance of a junction determines the operating conditions that should exist during EQE measurements and therefore it is an important parameter for this kind of measurements. In this section the one-diode model of a multi-junction device is presented in the case of finite and infinite shunt resistance indicating the strength of EQE signal in each case.

For the extraction of limiting current, we will consider the case of a double junction device for simplicity purposes. The electrical circuit of a double-junction PV device is depicted in Figure 6. From Kirchhoff's current law, the total output current I is equal to the total current flowing through the current limiting i-th junction for example

$$I(V) = I_i(V) = I_{L,i} - I_{sh,i}(V_i) - I_{d,i}(V_i) \tag{2.9}$$

where I_i , $I_{L,i}$, $I_{sh,i}$ and $I_{d,i}$ are the total current flowing through the i-th junction, the photocurrent generated due to light bias, the current flowing through its shunt resistance and its dark current respectively. The latter two terms depend on the voltage drop across the junction $V_{i,}$ which is governed by Kirchhoff's loop rule giving

$$V_i = V - V_{j\neq i} + I.R_s \tag{2.10}$$

Where $V_{j\neq i}$ is the voltage drop across the other junctions and R_s is the series resistance. The dark current follows the Shockley-Read-Hall equation and is given by (2.11)

$$I_{d,i}(V_i) = I_{0,i}\{\exp(\frac{qV_i}{nkT}) - 1\} \tag{2.11}$$

Substituting (2.10) and (2.11) into (2.9) gives the following characteristic equation for the i-th junction in a multi-junction device:

$$I(V) = I_{L,i} - I_{0,i}\left\{\exp\left[\frac{q\left(V - V_{j\neq i} + IR_s\right)}{nk_BT}\right] - 1\right\} - \frac{V - V_{j\neq i} + IR_s}{R_{sh}} \tag{2.12}$$

In the experimental set-up for SR measurements using light bias the photogenerated term is given by

$$I_{L,i} = I_{bias,i} + \delta I \tag{2.13}$$

where $I_{bias,i}$ is the DC component of the bias light and δI is the small AC component from the chopped monochromatic beam.

In the case of the EQE measurement of the top junction in a double junction device only the bottom junction is illuminated. The photogenerated current of the top junction follows (2.14) and is much smaller compared to the photogenerated current of the bottom one. The $I_{bias,top}$ represents the very weak DC component of the stray light.

$$I_{L,top} = I_{bias,top} + \delta I \ll I_{L,bot} \tag{2.14}$$

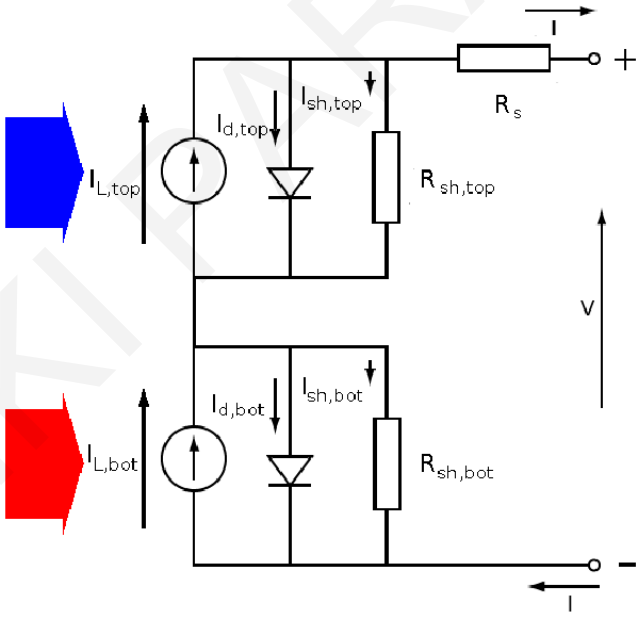

Figure 6: Equivalent circuit of a double-junction device.

When no voltage bias is applied across the tandem, the bottom junction operates close to its open-circuit voltage and the top junction is reversed biased with voltage

$$V_{top} = -V_{oc,bot} \tag{2.15}$$

The chopped monochromatic signal produces in principle an AC variation δV of the forward voltage bias across the bottom junction

$$V_{bot} = V_{oc,bot} - \delta V \tag{2.16}$$

and (2.12) becomes

$$I(V) = I_{bias,top} + \delta I - I_{0,top}\left\{\exp\left[\frac{-q\left(V_{oc,bot} - \delta V\right)}{nk_BT}\right] - 1\right\} + \frac{V_{oc,bot} - \delta V + IR_s}{R_{sh,top}} \tag{2.17}$$

In the infinite shunt resistance approximation, the shunt resistance of the top junction is high enough and thus the last term can be neglected from (2.17). At room temperature and for typical cell parameters the exponential term in (2.17) can also be neglected. $I_{0,top}$ therefore gives a constant contribution to the total current which is filtered out by the lock-in technique. $I_{bias,top}$ is also filtered out by the lock-in amplifiers. Thus the only measurable parameter left is the required ac-component δI. As a result in the absence of shunts in the device the measured limiting current is the small photocurrent from the monochromator (δI) as expected.

However, in the case of the EQE measurement of a low shunt resistance junction the measured current does not equal the desired monochromatic δI current due to the presence of several measurement artifacts. If we take into consideration (2.12) for the top junction the equation becomes

$$I(V) = I_{L,top} - I_{0,top}\left\{\exp\left[\frac{q(V - V_{bot} + IR_s)}{nk_BT}\right] - 1\right\} - \frac{V - V_{bot} + IR_s}{R_{sh,top}} \tag{2.18}$$

The shunt resistance term of the top junction (latter term) cannot be neglected and the bias light at the top junction follows (2.14). The series resistance of the device is zero and the shunt resistance of the bottom junction is assumed to be infinite. In an attempt to measure the top junction, blue monochromatic light is applied on the tandem. Light bias in the response region of the bottom is also applied in order to cause saturation of the junction. As discussed above under these conditions, the bottom junction is in forward bias with voltage

$$V_{bot}(I + \delta I) = V_{bot}(I) - \delta V \tag{2.19}$$

Thus the top junction is in reverse bias at

$$V_{top}(I+\delta I) = -V_{bot}(I+\delta I) = -V_{bot}(I) + \delta V \tag{2.20}$$

The ac-term δV can be calculated by (2.12) for the bottom junction giving

$$V_{bot}(I+dI) = \frac{nk_BT}{q}\ln\left\{\frac{I_{bias,bot}-I_{bias,top}+I_{0,bot}}{I_{0,bot}}\right\} + \frac{nk_BT}{q}\ln\left\{1-\frac{\delta I}{I_{bias,bot}+I_{0,bot}-I_{bias,top}}\right\} = V_{bot}(I) - \delta V \tag{2.21}$$

Thus δV is given by

$$\delta V = -\frac{nk_BT}{q} ln\left\{1-\frac{\delta I}{I_{bias,bot}+I_{o,bot}-I_{bias,top}}\right\} \equiv \frac{nk_BT}{q}\frac{\delta I}{I_{bias,bot}+I_{o,bot}-I_{bias,top}} \tag{2.22}$$

Putting (2.22) into (2.18) and neglecting terms smaller than δI gives

$$I(V) = I_{bias,top} - I_{0,top}\left\{\exp\left(\frac{-qV_{bot}}{nk_BT}\right)-1\right\} + \frac{V_{bot}(I)}{R_{sh,top}} + \delta I\left\{1-\frac{I_{0,top}}{I_{bias,bot}+I_{0,bot}-I_{bias,top}}\exp\left(-\frac{qV_{bot}}{nkT}\right) - \frac{nk_BT}{q}\frac{1}{R_{sh,top}(I_{bias,bot}+I_{0,bot}-I_{bias,top})}\right\} \tag{2.23}$$

At room temperature the exponential terms can be neglected. Assuming also that $I_{0,bot} << I_{bias,top}$ then (2.23) becomes

$$I(V) = I_{bias,top} + I_{0,top} + \frac{V_{bot}}{R_{sh,top}} + \delta I\left\{1-\frac{nkT}{q}\frac{1}{R_{sh,top}(I_{bias,bot}-I_{bias,top})}\right\} \tag{2.24}$$

The lock-in technique filters out the dc term $(I_{bias,top} + I_{0,top} + \frac{V_{bot}}{R_{sh,top}})$ in (2.24) and gives the term $\delta I\left\{1-\frac{nkT}{q}\frac{1}{R_{sh,top}(I_{bias,bot}-I_{bias,top})}\right\}$ which is strongly dependent on the shunt resistance of the top junction. This term may give rise to a decrease in the current signal measured with the lock-in technique at wavelengths where the top junction is expected to respond and a non-zero signal at wavelengths where the top junction is not expected to respond. That extra term is the origin of measurement artifacts present during EQE measurements of low shunt resistance junctions. To eliminate the measurement artifacts arising from the shunt resistance, application

of voltage bias is required to move the operating point of the current limiting device towards short-circuit conditions thus removing the impact of the shunt.

The presence of coupling effects in the bottom junctions creates another additional term in (2.24). If we assume that the middle junction is the current limiting junction in the device, then the underestimation of the EQE signal in the presence of both shunts and coupling effects in the material is

$$x = \left(\underbrace{\frac{nk_BT}{qR_{sh,mid}\left(I_{bias,top} + I_{0,top} - I_{bias,mid} - I_{LC}\right)}}_{shunt\ resistance\ term} + \underbrace{\frac{aI_{0,top}\, exp\left(\frac{qV_{top}}{k_BT}\right)}{I_{bias,top} + I_{0,top} - I_{bias,mid} - I_{LC}}}_{coupling\ term} \right) \quad (2.25)$$

The underestimation of the AC measured signal is due to the low shunt resistance (first term) and the luminescent coupling term (second term). Both terms give rise to a decrease of the measured EQE signal at the wavelength the middle junction is expected to respond. The exponential in the coupling term cannot be neglected at room temperature and at high light biases since the voltage bias of the top junction is not insignificant. At low light bias conditions, the voltage across the top junction is low and the coupling efficiency coefficient α is negligible leading to elimination of the second term. As the light bias of the top junction increases, the first term decreases while the second one increases.

2.6 Preliminary EQE results

After the validation of the EQE system, preliminary measurements of InGaP/InGaAs/Ge junctions have been performed. EQE results for the top junctions InGaP/InGaAs are depicted in Figure 7. Comparison between the EQE measured results with the ones taken by the manufacturer have been compared and demonstrated good agreement. Deviation between both EQE curves has not exceeded 2%. Improvement of the EQE signal from the junctions was observed in the presence of high power LEDs since the signal of the EQE correlates strongly with the bias spectrum applied on the cell under examination.

Further investigation of the ideal conditions that should be present during EQE testing has been undertaken. The results are presented and discussed in detail in the next sections.

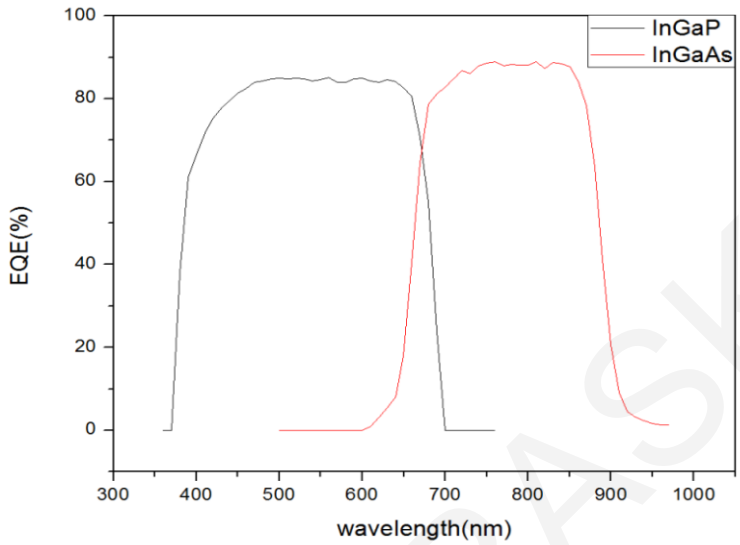

Figure 7: External Quantum Efficiency of the GaInP/GaInAs junctions of a triple-junction device.

2.7 Dark EQE

When during the EQE measurements of a multi-junction device no light bias is applied on the device, the procedure is referred to as Dark EQE. Dark EQE is a useful metric to extract the relative shunt resistance values of each junction in the multi-junction device. The presence of low shunt resistance in the junction creates measurement artifacts that affect the EQE measurements of the photovoltaic device. Consequently, knowledge of the shunt resistance of the junctions can be used to predict the problems that will arise during the measurement of the EQE of the multi-junction device. Depending on the relative magnitudes of shunt resistance in each junction the shape of the dark EQE can vary accordingly. The eight possible shapes of dark EQE are presented and discussed in detail in [25]. Figure 8 presents the measured values of Dark EQE from two different technology triple-junction InGaP/InGaAs/Ge solar cells (C4MJ1 and C3MJ1). C4MJ1 solar cell is a metamorphic fourth generation solar cell with 40% efficiency while C3MJ1 is a third generation solar cell with 38.5% efficiency. The dark EQE from both C4MJ1 and C3MJ1 devices according to [25] corresponds to the case of finite shunt resistance in all junctions of the tandem device. Specifically, the shape of the dark EQE for

both devices as depicted in Figure 8 corresponds to higher shunt resistance in the top junction and very low shunt resistance in the bottom junction. In C4MJ1 device the shunt resistance of the top junction is much higher compared to the shunt resistance of the middle junction since the EQE signal in the response region of the middle junction is very low compared to the one observed in the response region of the top junction. The typical value of the top junction shunt resistance is of the order of MΩ while the shunt resistance of the middle junction is of the order of 10^5Ω. However, in the case of the C3MJ1 device the resistances of the top and middle junctions are very close (both of the order of 10^5Ω), with the shunt resistance of the top junction to be slightly higher compared to the shunt resistance of the middle. The shunt resistance of the bottom junction is much lower compared to the shunts of the top and middle junction and is believed to be around some kΩ.

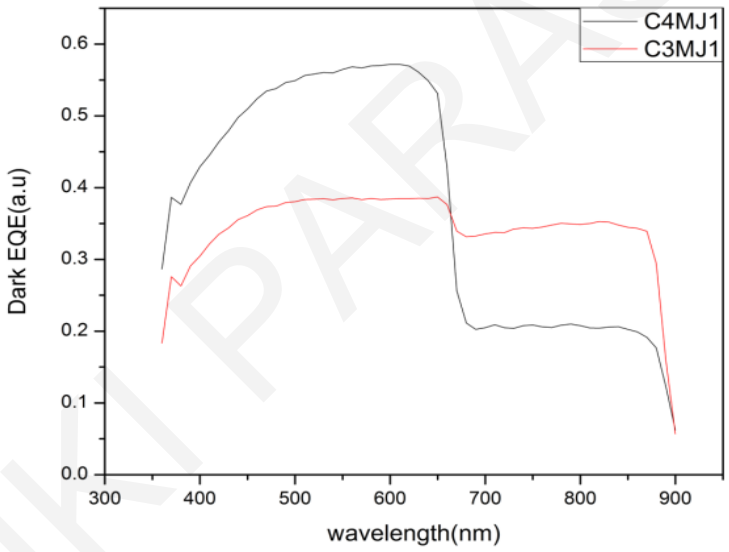

Figure 8: Dark EQE from two different technology cells: C4MJ and C3MJ.

2.8 EQE at high intensity light bias conditions-Impact of voltage bias

Multiple EQE measurements have been carried out at different light and voltage conditions in order to demonstrate the ideal conditions for EQE testing. Measurement artifacts which lead to reduction of the measured EQE signal are often observed during measurements. Thus investigation of the appropriate light and voltage conditions that eliminate the artifacts during measurements is required. The solar cell under study in this section is a lattice matched Azur cell InGaP/InGaAs/Ge with 35.8% efficiency and dimensions of 30 mm^2. The Dark EQE of the

solar cell is similar with the Dark EQE of C4MJ1 cell depicted in Figure 8. Thus in the tandem, the shunt resistance of the top junction is higher compared to the shunt resistance of the middle and bottom junctions. Test device specifications given by the manufacturer are shown in Table 2.

Table 2: EQE measurement of multi-junction cell: test device specification. The data corresponds to 500 sun concentration.

Code	V_{oc} (V)	I_{sc} (A)	V_{mp}(V)	I_{mp} (A)	FF (%)	*n* (%)
A3	3.144	2.151	2.842	2.102	88	39

Initially, EQE measurements at high intensity light bias conditions and different voltage bias were carried out. We assume that high intensity light bias conditions correspond to light bias intensity that produces a photocurrent higher than 1.50 mA/cm^2 in the top junction. High-intensity light bias conditions may be expected to reduce the impact of the low shunt resistance and eliminate the measurement artifact term and thus the reduction of the EQE signal with voltage. The EQE curves were investigated in a broad range of voltage bias values as seen in Figure 9 for both (a) middle and (b) top junctions. Light bias conditions applied for the measurement of the top InGaP junction create a photocurrent of density around 2.17 mA/cm^2 while the light bias used for the measurement of the middle InGaAs junction was set to higher intensities. The photocurrent produced by the top junction in this case is 4.50 mA/cm^2.

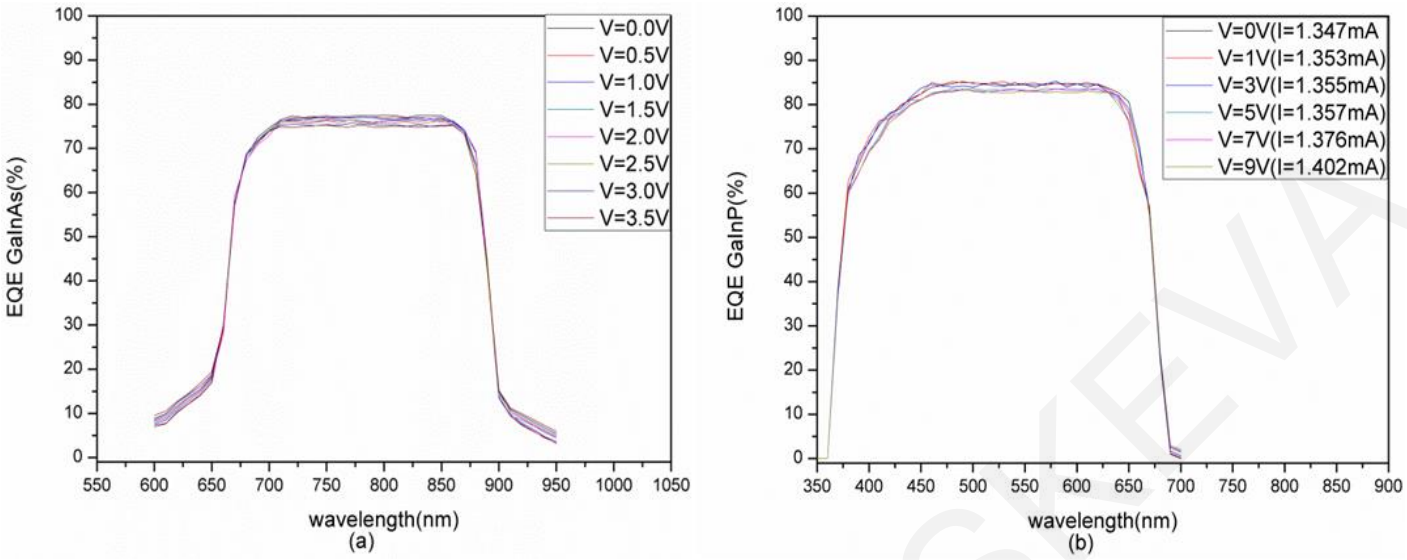

Figure 9: Voltage bias dependence of the EQE in both (a) middle InGaAs and (b) top InGaP junction under high intensity light conditions. High intensity light bias conditions correspond to top junction photocurrents of 4.50 mA/cm^2 for the measurement of the middle InGaAs and 2.17 mA/cm^2 for the measurement of the top InGaP junction.

Voltage bias is required in order to keep the current limiting junction close to short-circuit conditions. In particular, the amount of voltage bias that should be applied to InGaP and InGaAs is 0 V and 1.3 V respectively which represent the sum of the expected forward voltage operating points of the component junctions not being measured. As shown in Figure 9 the application of voltage bias on InGaAs and InGaP is observed to have a small effect on the EQE signal of the junctions. The top junction with the higher shunt resistance seems unaffected by the application of voltage bias whereas the middle junction with the lower shunt resistance is affected more, exhibiting a very small reduction in the EQE signal. The overestimation of the EQE signal in the absence of voltage bias is small in the low shunt resistance junction (InGaAs) and zero in the high shunt resistance junction (InGaP) as expected. These results are confirmed in Figure 10 where the EQE of the middle junction at 800 nm and 950 nm is plotted against voltage bias (the variation between 0 V and 1.3 V is around 1.1%). At very high voltage bias (above 1.5 V), underestimation of the EQE signal in the middle junction is observed at wavelengths in the response region of the junction (800 nm) and overestimation of the signal at wavelengths outside the response region of the junction (950 nm).

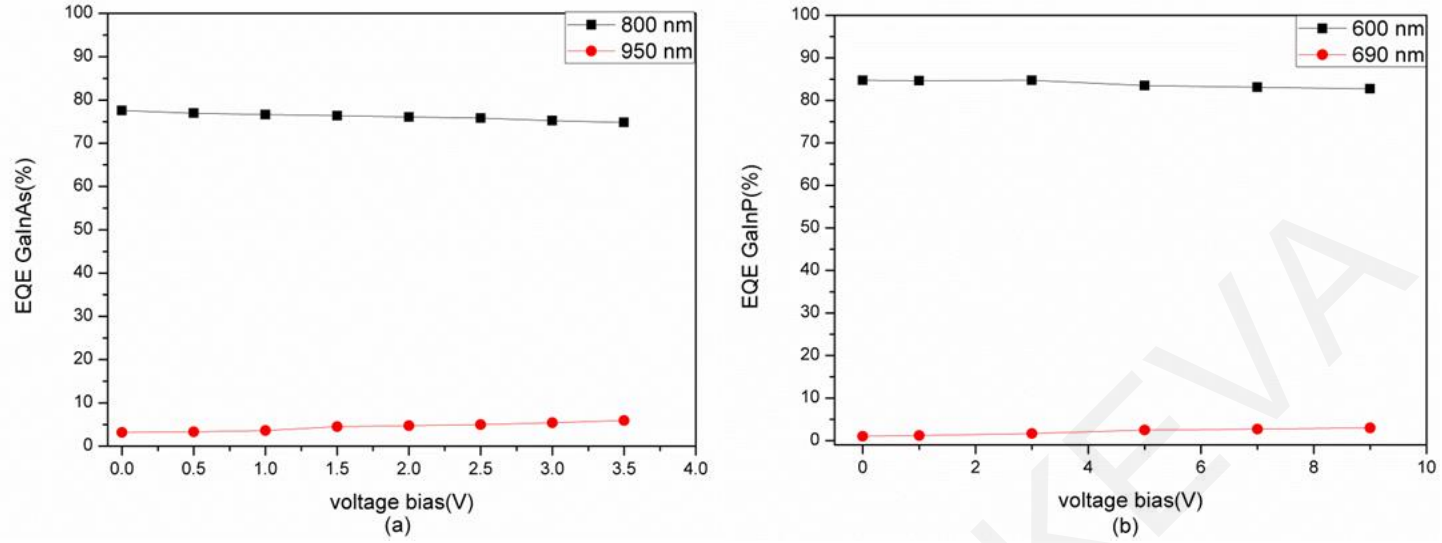

Figure 10: EQE dependence on forward bias voltage of (a) InGaAs middle junction at 800 nm and 950 nm and (b) InGaP top junction at 600 nm and 690 nm. Measurements were taken at 4.50 mA/cm^2 for InGaAs and 2.17 mA/cm^2 for InGaP and correspond to high intensity light bias conditions.

Similarly in the EQE spectrum of the top junction, the variations of the EQE signal due to voltage are negligible as shown in Figure 10(b) due to the high shunt resistance of the top junction. Thus under high intensity light bias conditions the shunt resistance effect is almost irrelevant and voltage bias does not strongly affect the measurements. One other important aspect observed during the measurements under high intensity light conditions is the underestimation of the InGaAs middle junction signal in the response region of the junction. Measurement artifacts are evident in Figure 9(a) for InGaAs middle junction characterized by a lower than expected EQE in the range from 650 nm to 900 nm. EQE values lie around 77% which indicate that the signal was largely underestimated compared to the ideal case where the signal is around 0.9. This is tentatively attributed to luminescent coupling effects mentioned above which are of major influence during the EQE measurements of high quality materials under high intensity light bias conditions. Luminescent effects during the measurement of the middle junction may arise due to significant charge carrier radiative recombination and emission of photons occurring in the top junction, which can be absorbed by the middle junction. Luminescent coupling from the top junction to the middle one can cause measurement artifacts and underestimation of the EQE signal as was indicated in the measurements. The existence of this coupling effect was confirmed by measuring the luminescent emission from the cell during EQE measurements using a fiber-coupled spectrometer. An emission wavelength was observed at 660 nm, which is the region of the energy gap of the top junction

as indicated in Figure 11. The light bias used during the EQE measurement of the middle InGaAs junction was a combination of high intensity blue and infrared LEDs. Luminescent coupling measurement artifacts appearing at intense light bias conditions suggest that these operating conditions are not appropriate for accurate EQE measurements. An extensive study of luminescent coupling effects between junctions in a multi-junction device is provided in the next chapter.

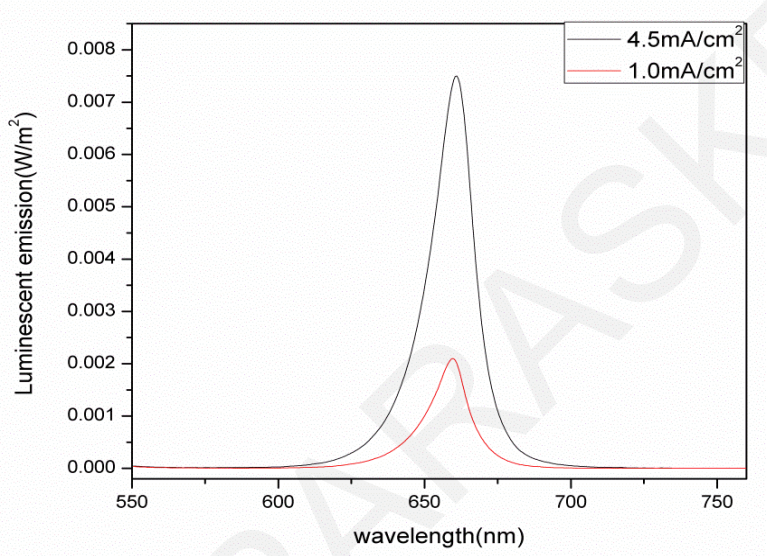

Figure 11: Characteristic luminescent emission from the top junction under ideal (1.0 mA/cm^2) and high intensity (4.5 mA/cm^2) light bias conditions. The difference in radiative recombination emitted from the cell is clearly observed.

2.9 EQE at low intensity light bias conditions-Impact of voltage bias

After EQE testing at high intensity light bias conditions, the effect of voltage bias under low intensity light bias conditions was also investigated. Low intensity light bias conditions correspond to light bias intensity that produces photocurrent of the top junction of 0.39 mA/cm^2. Under these conditions, the voltage is expected to affect EQE especially for low shunt junctions. Therefore, for the middle junction device the impact of voltage bias is expected to be of major influence. As shown in Figure 12(a) overestimation of the EQE signal outside the area of response (e.g. at 950 nm) and underestimation within the region of response (e.g. at 800 nm) are artifacts due to shunts which appear at low light bias conditions. EQE values are lower (≈0.85) than in the ideal case (≈0.9) because of the inability of the bias light to cause current

limitation of the junction of interest. The combination of very low shunt resistance of a junction with suboptimal light conditions gives rise to a very high measurement artifact term with severe effects on the EQE signal. The underestimation of the EQE signal from the middle junction at 1.3 V exceeds 30 % as seen in Figure 13.

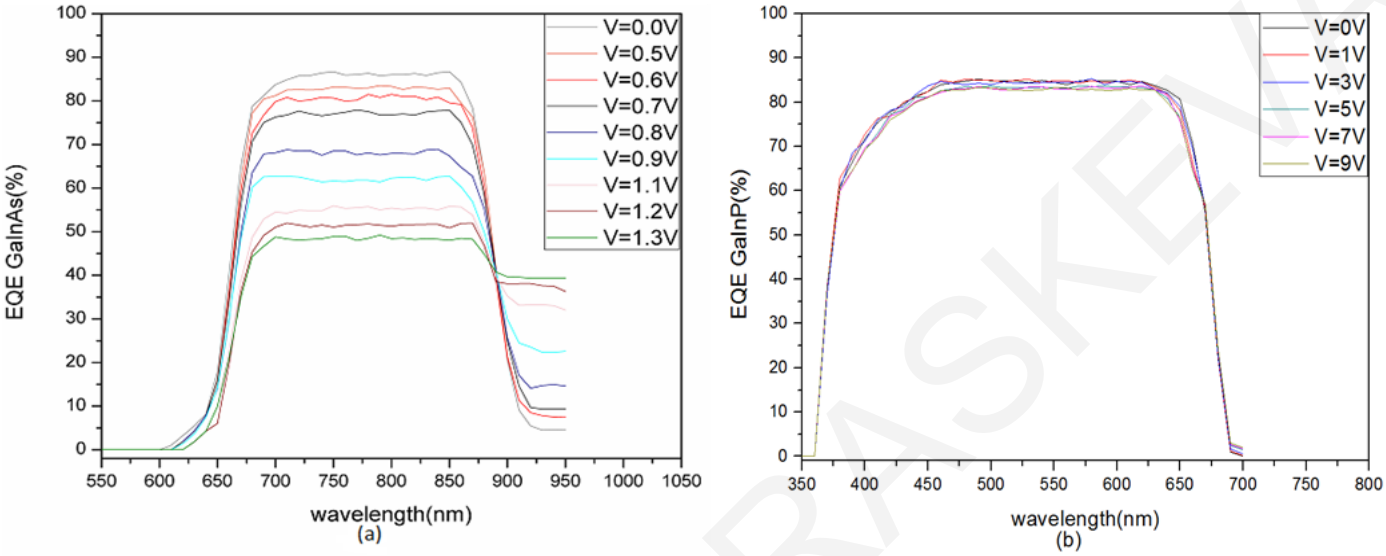

Figure 12: Effect of voltage bias on the EQE of (a) middle InGaAs and (b) top InGaP junctions under low intensity light conditions. Low intensity light bias conditions correspond to generated photocurrent of 0.39 mA/cm^2.

For the top InGaP junction, voltage bias effects are negligible (see Figure 12b) similarly to the case of high intensity light conditions.

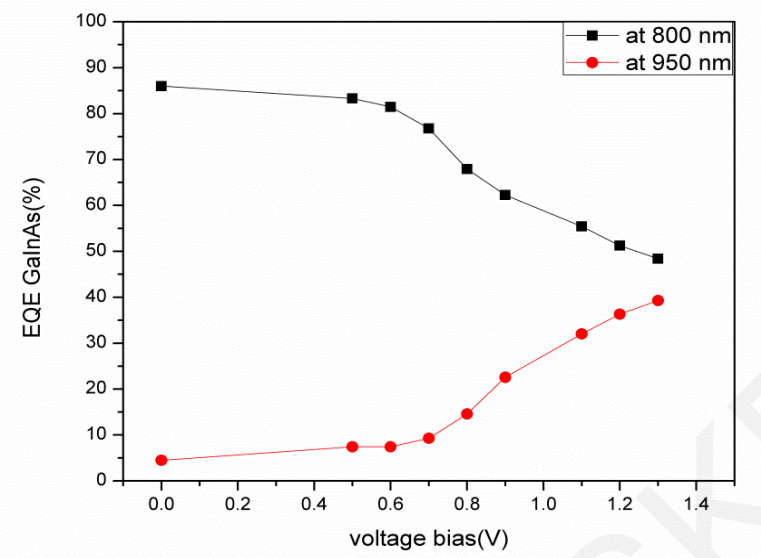

Figure 13: EQE dependence on forward bias voltage of InGaAs middle junction under low intensity light bias conditions. The underestimation of the signal at high voltage bias is evident.

2.10 EQE at high intensity light bias conditions-Impact of shunt resistance

In order to investigate the impact of shunt resistance at high light bias intensity where coupling occurs, EQE measurements have been performed in two GaInP/GaInAs/Ge solar cell devices at high light bias conditions. The solar cells have been manufactured by Azur and have dimensions around 30 mm^2. The two devices are identical but with top and middle GaInP/GaInAs junctions of different shunt resistances. Different shunts and therefore defect states exist in both devices affecting the measured EQE in the presence of coupling effects. The intensity of the light bias controls the amount of recombination current flowing through the top GaInP junction and therefore influences the amount of luminescent current directed to the middle GaInAs junction. The shunt resistance of the middle junction was investigated with spectrally resolved Electroluminescence (EL) and Dark EQE methods. EL indicates the radiative recombination in each junction while dark EQE provides information about the current leakage through junctions as mentioned previously. The impact of shunts was also investigated through I-V curves of each device at different light bias conditions.

A number of identical cells have been investigated and the two devices which presented the largest differences in spectroscopic EL and dark EQE were chosen to indicate the effect of the shunt. The comparison was undertaken on identical multi-junction devices in order to clearly investigate the effect of the shunts and no other parameters. The spectroscopic EL from the two

different quality devices (labeled as C1 and C2) which presented the largest differences is depicted in Figure 14. The magnitude of the radiative recombination in the junctions provides a measure of the material quality of each junction in the photovoltaic device. Consequently, knowledge of the material quality of the junctions can be used to extract conclusions about the correlation of material quality and thus shunt resistance, with luminescent coupling effects.

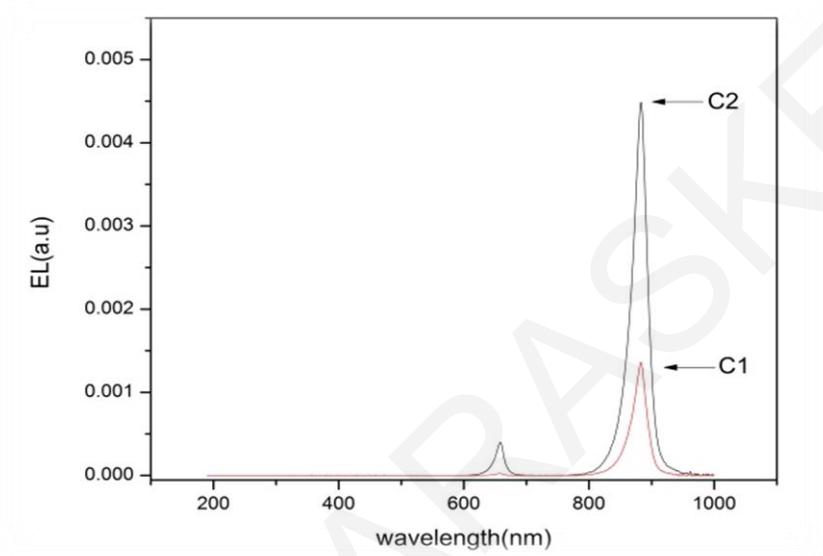

Figure 14: Spectroscopic EL emission from two different samples. The difference in radiative recombination between the two samples is clearly observed.

Two main peaks are apparent in the EL spectrum in Figure 14 and indicate the band gap region of the two top junctions GaInP and GaInAs. Figure 14 demonstrates that the radiative recombination in device C2 is considerably higher compared to the radiative signal emitted by cell C1 highlighting the higher material quality of sample C2. The radiative signal from the top GaInP junction will determine the magnitude of the coupling current directed towards the middle InGaAs junction. Since higher radiative current is apparent in sample C2, larger coupling current is probable to be present in that sample. The presence of significant non-radiative recombination in a device and lower shunt resistance causes additional paths for the current and lowers the coupling signal.

Dark EQE measurements have also been carried out in an attempt to extract the relative value of the shunt resistance of each junction in the devices (Figure 15). The EQE signal from C2 is

lower compared to C1 indicating lower leakage current and thus higher shunt resistance in both –top and middle- junctions.

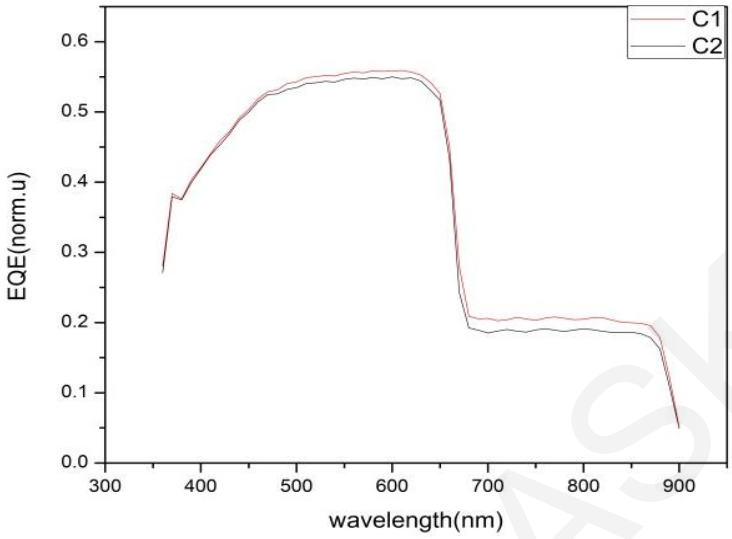

Figure 15: Dark EQE from two different samples.

Next, the output current in the GaInAs middle junction from both samples was measured by current limitation of the junction. The characteristic I-V curves of the devices were measured at light bias conditions that cause current limitation on the middle junction. The results are depicted in Figure 16. The samples were excited by a 450 nm LED that excites the top GaInP junction and a laser module at 980 nm that excites the bottom Ge junction. The beam size of the IR module is 5 mm in dimeter and it is much lower compared to the dimension of the cells which is around 30 mm^2. The output current is actually the sum of the coupling current directed towards the middle junction and the shunt current of the junction (the detailed description of that relationship is given in the next chapter). The I-V curves in Figure 16(a) were measured under light bias conditions that produce photocurrents of the top junction around 1.7 mA/cm^2. The measured output generated photocurrent for cell 1 is 15 $\mu A/cm^2$ and for cell 2, 12 $\mu A/cm^2$ at voltage bias of 0 V. The output current of C1 is higher at reverse bias conditions due to the higher shunt current in the device. Under these light bias conditions, coupling effects start to become evident. The top junction photocurrent is the measured output current of the solar cell when a light bias is applied in the response region of the GaInAs junction (808 nm) in order to cause the GaInP junction to be current limiting.

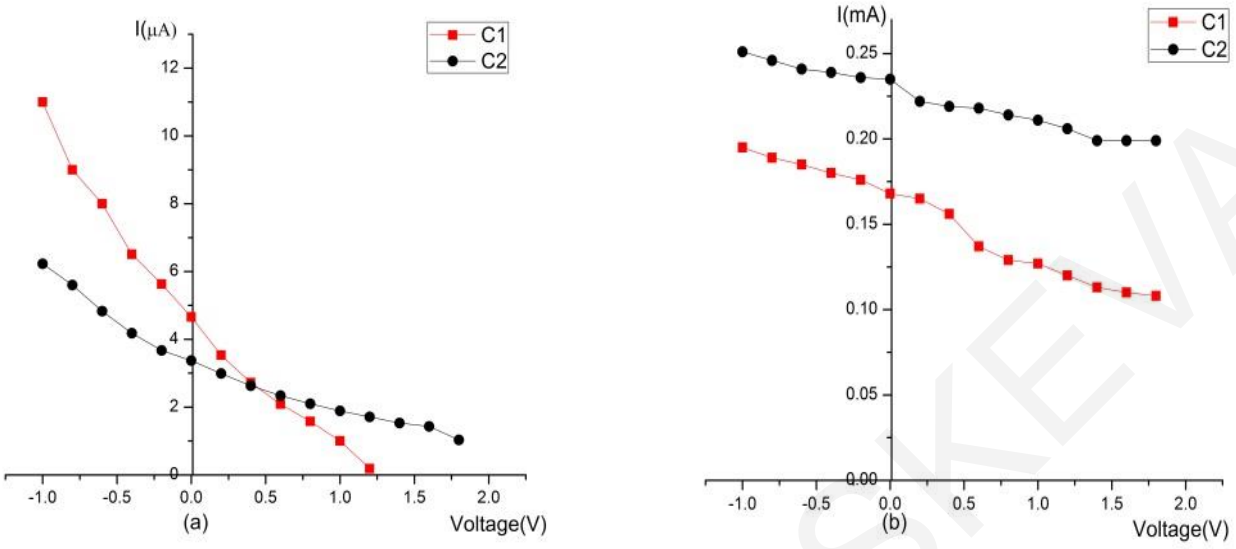

Figure 16: Measured I-V curves for devices C1 and C2 for photocurrents of the top junction of (a) 1.7mA/cm^2 and (b) 12mA/cm^2.

The I-V curves of Figure 16(b) were taken at higher light bias conditions. In this case, light bias conditions produce a photocurrent of the top junction which is approximately equal to 12 mA/cm^2. The output generated photocurrent for C1 is 0.55 mA/cm^2 while for C2 is 0.77 mA/cm^2 at a voltage bias of the device of 1.2 V. Figure 16(b) shows that the transition towards higher light bias causes a significant increase of the output current and thus of coupling current especially in the high quality material. The current of the high quality material C2 is higher at all voltage biases indicating that the coupling effects are dominant at all applied voltages while the shunt resistance effects are eliminated. The data shows that cell C2 is more affected by coupling and for that reason coupling effects are expected to be enhanced in high quality material devices. Therefore, higher coupling current directed towards GaInAs is expected to cause more pronounced measurement artifacts during EQE measurements. At the same light bias conditions of Figure 16(a) the EQE measurements of the middle GaInAs junction in both devices were found to be identical (see Figure 17a). This indicates that in those conditions the effects of the shunt and coupling are negligible due to the use of appropriate light and voltage biasing. The EQE of both devices was then measured under higher light bias conditions in order to examine the impact of shunt resistance on coupling effects. The light bias conditions

used in that case are the ones used in Figure 16(b) where strong coupling effects exist. The results are depicted in Figure 17(b).

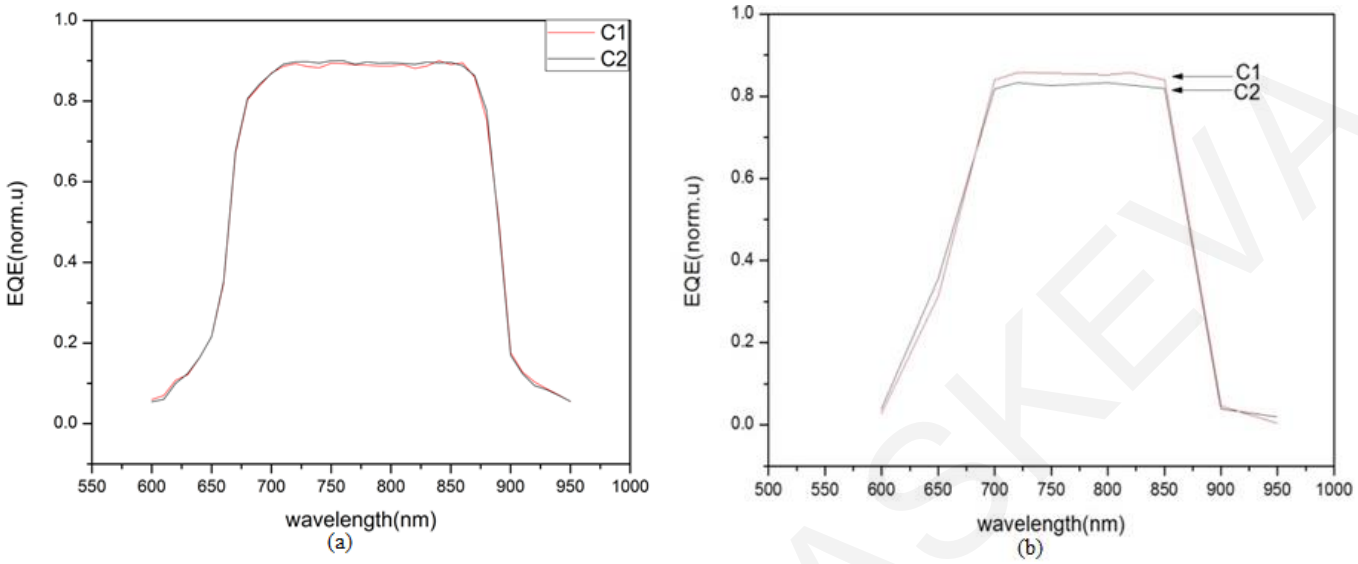

Figure 17: EQE values of GaInAs for devices C1 and C2 under (a) ideal and (b) high light bias conditions. The voltage bias applied to the devices is 0.6 V.

As can be observed in Figure 17(b) the EQE signal in the high shunt device is marginally lower compared to the signal of the lower shunt device. This occurs in all wavelengths within the response region of the GaInAs junction. The difference between both signals is around 2.5% and it is believed to be attributed to different coupling effects present in both materials. The EQE reduction of the high shunt resistance device is larger at high intensity light bias conditions and thus the opposite behaviour is observed compared to EQE at low light bias conditions. Therefore, at higher light bias intensity the impact of coupling causes underestimation of the EQE signal and the reduction is more pronounced in higher quality materials. The impact of coupling effects in two different quality materials will be examined further in the next chapter using the PL method.

2.11 Spectrometric characterization

Spectrometric characterization of the solar cell was then performed, in order to establish the appropriate light bias conditions for current limitation of the junction under investigation. Spectrometric characterization of the triple-junction device was investigated under variable light bias pointing out the effects of current limitation and current matching of the junctions.

This method has been introduced as a valuable tool for the investigation of the behaviour of the I-V parameters of a multi-junction solar cell to variations of the incident spectrum. Spectrometric characterization was achieved by performing a series of I-V measurements while varying the intensity of a blue LED in combination with a multi-wavelength light source rich in infrared wavelengths and of constant light intensity. The cell used in this case was a GaInP/GaInAs/Ge with dark EQE similar to that obtained in Figure 15. It is well known that the light I-V curve of a triple-junction cell reflects the shape of the current limiting junction and therefore this method gives valuable information about the current matching of the junctions [28]. A set of electrical parameters such as short-circuit current (I_{sc}), maximum power point current (I_{MPP}), maximum power point power (P_{MPP}) and fill factor were extracted from the I-V characteristics as shown in Figure 18.

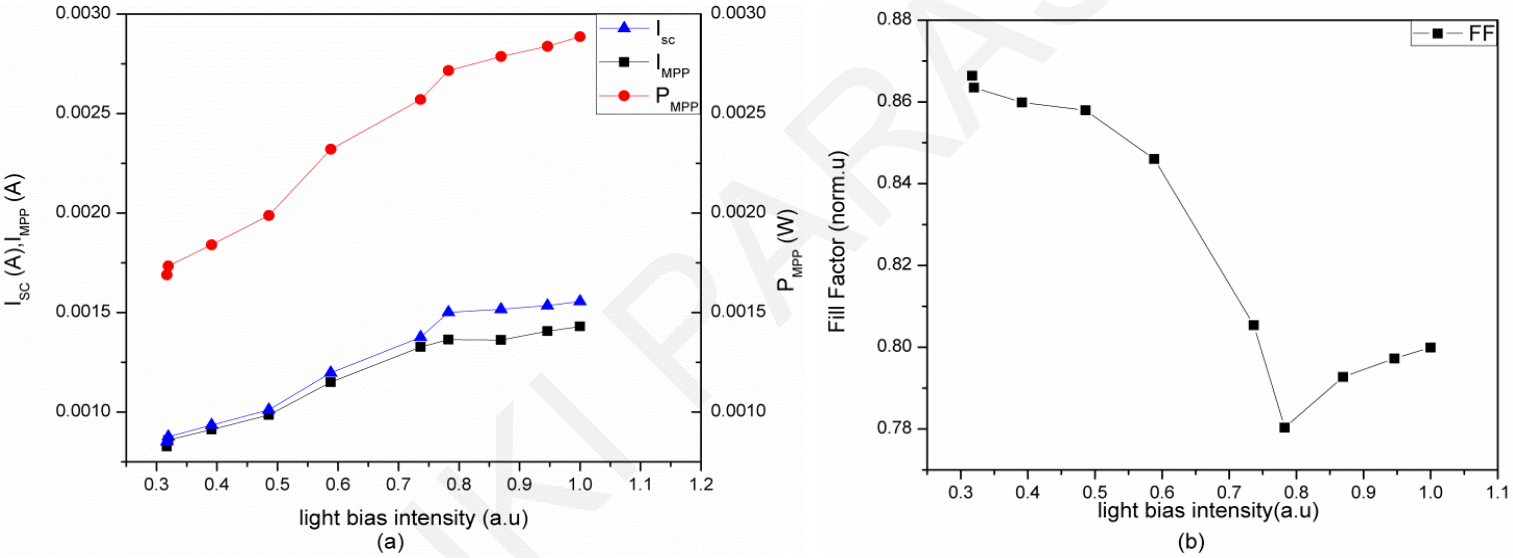

Figure 18: Cell parameters extracted from I-V curves under variable blue light bias intensity. The light intensity was controlled by the voltage applied to the LED power supply.

Spectrometric characterization was previously presented in the literature in the case of constant total irradiance [29]. In our measurements the total incoming bias light irradiance is not kept constant so the short-circuit current and the maximum power point current of the device are expected to increase continuously as the irradiance of the incoming light increases. Even in these conditions the local minimum of the fill factor and the change in the increase rate of short-circuit current (I_{sc}) and maximum power point current (I_{MPP}) are still clearly visible in the current matching point and this is in agreement with previously published work [7], [15].

The current match of the two junctions holds at 0.78 a.u light bias intensity where the minimum of the fill factor and the change in the rate of currents coincide. For values lower than that, the top junction was current-limiting, since the blue bias light was not strong enough to cause a correct current balance and the light source saturates the bottom junctions. For current values higher than the current matching point, the middle junction was current limiting since bias light conditions cause saturation of the top and bottom junction. The short-circuit current plot in Figure 18(a) shows a typical behaviour for the case where the middle junction has a low shunt resistance, indicated by the large difference between maximum power point current and short-circuit current. Due to the low shunt resistance of the middle junction, the I-V curve has non-ideal properties and the current drops fast, which explains the large difference between the short-circuit and the maximum power point current. This confirms the dark EQE results (Figure 15) and proves that the middle junction is of lower shunt resistance. Therefore this study demonstrates that spectrometric characterization can be another method of identification of the magnitude of the shunt resistance in the device.

The transition from the top to the middle current limiting junction at the same light bias intensity used in Figure 18 can be observed clearly with EQE measurements (see Figure 19).

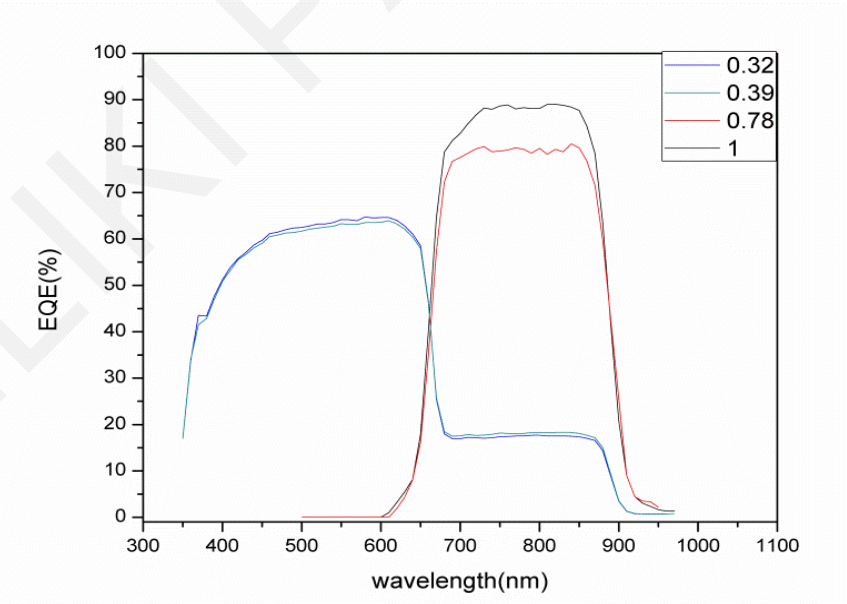

Figure 19: Measured EQE under variable blue light bias intensity: EQE is shown for four different light bias intensities. The transition from the top to the middle current limiting junction is evident.

Initially, before the current matching point, the top junction was current limiting as shown in Figure 19. After the current matching point the middle junction is measured. Transition from the top junction to the middle occurs at 0.78 a.u light bias intensity and is in agreement with spectrometric characterization measurements.

Conclusions

In summary, EQE measurements of GaInP/GaInAs have been investigated at various voltages and light biases and subsequent suggestions for improved test methods of SR/EQE measurements were made. Results have shown that voltage bias applied to the multi-junction cell has a strong effect only in the cases when the junctions have low shunt resistance. Ideal light bias conditions have been found to be the light bias values that cause top junction photocurrents between 0.45 mA/cm^2 and 1.5 mA/cm^2. Reduction of the EQE signal has been obtained at high light bias conditions due to coupling effects. The EQE reduction has been found to be higher in the higher material quality samples. Finally, dark EQE and spectrometric characterization have been found to be very valuable methods for the investigation of the shunt resistance of each junction in the tandem devices and they are recommended to be used prior to EQE measurements.

Chapter 3

Luminescent coupling effects in InGaP/InGaAs/Ge solar cells

3.1 Introduction

During EQE measurements of multi-junction devices presented in the previous chapter, underestimation of the results was found due to coupling effects. Luminescent coupling refers to the phenomenon in which a significant amount of photons originating from radiative recombination can be absorbed by the bottom junctions. Specifically, under high bias conditions in high quality materials, radiative recombination centres can be created at the top junctions and can become of major importance. Higher carrier recombination causes emission of photons that can be absorbed by the bottom junctions thereby enhancing the current output of the bottom junction. The rate of band-to-band recombination is higher for direct band gap materials and thus coupling effects are expected to have significant influence in GaInP/GaInAs tandem devices resulting in a considerable change of junction photocurrents. Limited knowledge exists so far on the influence of the coupling effects on PV cell performance. As a result, the characterization methods of EL and PL have been used to establish the impact of shunt resistance, material structure and temperature on the coupling current. Investigation of coupling is necessary since this might have a significant influence on the efficiency and the energy yield of solar cells.

3.2 State of the art

The presence of luminescent coupling was first observed by Lim et al [16] during EQE measurements in the middle GaInAs junction of a multi-junction GaInP/GaInAs/Ge device. Their investigation demonstrated the reduction of the EQE signal of the middle junction due to the presence of significant amount of photons directed towards the junction. The same authors extended their investigation to the combined effects of shunt and luminescent coupling on measurement artifacts appearing during EQE measurements [17]. Thus these effects can be important during EQE measurements of multi-junction solar cells at high bias conditions and have the potential to affect the measured current-ratio of the junctions. The EQE method was also used to demonstrate the effect of surface passivation and light bias on coupling effects [19].

As it is well known, the efficiency of a multi-junction device is at its maximum when there is current matching between junctions in a tandem. Due to coupling the junctions may operate away from current matching conditions since the current of the current limiting junction might increase significantly. Previous calculations showed that under optimal conditions (the spectrum conditions at which the junctions were designed to be current matched) monolithic tandem devices without radiative coupling performed marginally better [30]. However, under non-optimal conditions the stack with coupling performed reasonably well compared to the tandem without coupling.

Recently, spatially-resolved EL in the triple-junction GaInP/GaInAs/Ge solar cell was used to demonstrate the junction coupling effect [31]. Using a combination of monochromatic light sources quenching of the EL images of the top GaInP junction was observed due to optical interactions between junctions. The authors used the same method to extract the photo-voltages of the junctions in the tandem device [32].

Furthermore, apart from experimental investigation of coupling, modelling of current-voltage characteristics of a multi-junction device in the presence of coupling was carried out. An analytical model for the current-voltage characteristics of a multi-junction solar cell in the presence of luminescent coupling was developed by Freidman et al [33]. The same authors

demonstrated that luminescent coupling affects critical aspects of the cell design that include the optimal junction thicknesses and band-gaps and has an impact on the dependence of the cell performance on the spectral content of the light illuminating it [34]. A combined measurement and analytical approach to characterize the short-circuit current including the effects of luminescent coupling was presented in [35]. Furthermore, a study of the effects of luminescent coupling on the measurement of the junction photocurrents for a series-connected III-V multi-junction solar cell was reported in [36].

Despite the work that has already been performed on coupling, many of the factors affecting the optical interactions between junctions are still unclear and should be investigated in an attempt to improve material design taking into account coupling effects. Thus, the effects of shunt resistance, material structure and temperature have been investigated for the first time demonstrating the impact of material quality and design as well as temperature on coupling effects. The results are presented and discussed in detail in this chapter. The examination has been implemented using a multiple-wavelength PL set-up.

Furthermore in an attempt to investigate the impact of shunts on coupling effects, a new model of the shunts in multi-junction solar cells has been developed. In particular, a physical model of a PV cell incorporating local shunts has been developed demonstrating the impact of shunts under solar cell operation.

3.3 PL analysis of coupling effects-Impact of shunt resistance

Excitation power dependent PL measurements of GaInP/GaInAs/Ge solar cell devices of different material quality were carried out in order to demonstrate the effect of shunt resistance on luminescent coupling effects.

Excitation power dependent PL measurements were carried out under high intensity bias light in the wavelength region of the top (300 to 660 nm) and bottom (980 to 1700 nm) junction in order to cause current-limitation in the middle junction and measure the coupling current directed towards it. During excitation power dependent PL measurements, the samples were excited by the 450 nm LED that excites the top GaInP junction and an infrared laser module (IR) at 980 nm which excites the bottom Ge junction. The blue LED output was varied and

produced a bias photocurrent of 1-5.7 mA/cm^2 at a voltage bias of 1.2 V. The light bias of the IR laser, which caused saturation of the Ge bottom junction was kept constant and was of much higher intensity compared to the other light sources. The beam size of the IR laser is 5 mm is diameter. The detailed diagram of the set-up is provided in Figure 20. Measurements showed that under these light bias conditions the shunt current leakage is eliminated and coupling effects start to be present. In an attempt to investigate the coupling effects at even higher light bias conditions a green laser module with fixed intensity was added. The beam size of the green laser is 3 mm in diameter. In that case the bias photocurrent of the top junction fluctuated between 5.4-9 mA/cm^2. The PL signal was captured by a Silicon (Si) based spectroradiometer which covers the ultraviolet and visible region. During excitation power dependent PL measurements, a fixed voltage bias was applied to the solar cell devices whilst the luminescence and bias current outputs were measured. All the measurements were carried out at room temperature.

The cells under investigation were concentrator lattice matched GaInP/GaInAs/Ge triple-junction devices with the same dimensions but different shunt resistances and structural parameters. The cell's manufacturers are Azur and Spectrolab and they have dimensions of 30 mm^2. Since the cells were fabricated by different manufacturers it is expected that different tunnel junction thicknesses, barrier and window layers will exist in the devices. The two different series of triple-junction devices were labeled as A, S. A cells correspond to cells manufactured by Azur while S cells are cells manufactured by Spectrolab. The detailed specifications of the cells can be found in [37], [38]. Comparison between the measurements in the lattice matched series A and S devices was performed in order to indicate the effect of coupling efficiency on different shunt resistance devices.

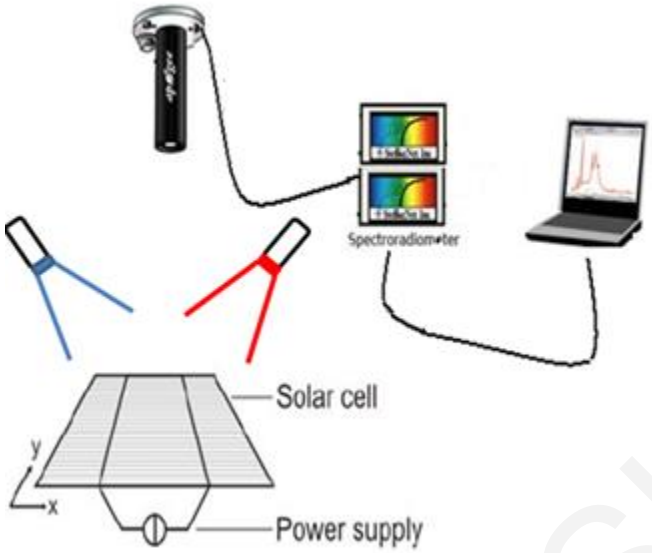

Figure 20: Experimental set-up of the excitation dependent PL used for the investigation of shunts.

3.3.1 Electrical model of a multi-junction device

Before the experimental investigation of the cells, a model was developed to interpret the resulting data. The equivalent circuit of a two junction device under bias light conditions during PL measurements, which takes into account the radiative coupling effects, is presented in Figure 21. In order to measure the luminescent coupling current in the middle junction, the junction should be the current-limiting one in the tandem. For that purpose the cell should be investigated with the PL method. The main point of this analysis is to indicate the impact of the shunt resistance on luminescent coupling effects. For simplicity the model ignores the bottom layer and it is assumed that the main interaction under investigation is between the top and middle subcells in a triple-junction device. Shunt resistance is missing from Figure 21 since the application of voltage bias reduces the impact of the shunt resistance and thus the device behaves as an ideal solar cell with infinite shunt resistance. The circuit corresponds to the case where the top junction is saturated due to strong bias light and the middle one exhibits coupling effects due to excess recombination current flowing towards the GaInAs. In order to cause saturation of the top junction, a blue bias light was applied to the device.

The currents shown in the circuit are the dark (recombination) current for the top junction ($I_{rec,top}$), the top junction photocurrent ($I_{bias,top}$) due to light bias and the output current of the

solar cell (I_{out}). The middle junction photocurrent ($I_{bias,mid}$) corresponds to the stray light from the environment applied on the middle junction but is very weak so it can be neglected ($I_{bias,top}>>>I_{bias,mid}$). A portion of the recombination current of the top junction is absorbed by the GaInAs junction and generates the photocurrent I_{LC}.

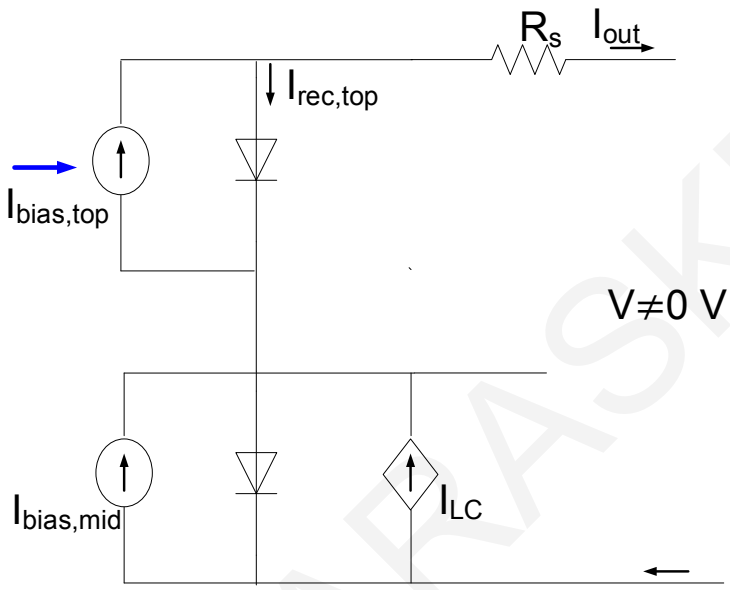

Figure 21: Circuit model of a double junction in the absence of shunt resistance.

The dark-recombination current of the top junction contains a radiative and a non-radiative part. Band-to-band radiative and non-radiative processes in the neutral region and at high forward bias can be expressed by (3.1).

$$I_{rec,top} = I_{01,top}[\exp\left(\frac{qV_{top}}{k_B T}\right) - 1] \tag{3.1}$$

Where $I_{01,top}$ is the saturation current of the top junction and V_{top} is the voltage of the top junction. When the top junction is illuminated photons from the GaInP junction are emitted near the band gap and absorbed by the middle junction device. This means that part of the recombination current of GaInP is flowing through the middle GaInAs layer and is converted to luminescent current I_{LC} causing coupling effects. Therefore I_{LC} is a function of I_{rec}

$$I_{LC} = aI_{rec,top} \tag{3.2}$$

The coefficient α is referred to as coupling efficiency coefficient and determines the amount of recombination current converted to coupling current. The coupling efficiency is determined by the ratio between radiative and non-radiative processes in the device. Devices with different density of shunts are expected to have different coupling efficiency coefficient.

The arrows in Figure 21 indicate the polarity of each junction. Due to strong bias light applied in the wavelength region of the top junction, the junction is strongly forward biased while the middle one is reversed biased. The blue light bias causes the top junction to operate near its open- circuit voltage. Because the GaInP is forward biased a portion of the $I_{bias,top}$ recombines in the subcell as I_{rec} and the remaining current is extracted from the subcell as I_{out} according to the (3.3):

$$I_{out} = I_{bias,top} - I_{rec,top} = I_{bias,top} - I_{01,top}[\exp\left(\frac{qV_{top}}{k_B T}\right) - 1] \tag{3.3}$$

Furthermore, another expression for the output current (I_{out}) when we take into consideration the reverse bias middle junction becomes

$$I_{out} = I_{bias,mid} + I_{LC} \approx I_{LC} \tag{3.4}$$

The GaInAs is not externally biased and the photocurrent of the middle junction ($I_{bias,mid}$) can thus be neglected. The recombination current of the middle junction is neglected since the GaInAs junction is in reverse bias in those conditions. The luminescent coupling current is added to the bias photocurrent since both currents have the same direction as obtained in Figure 21. The simple form of (3.4) holds with the assumption that the current-voltage (I-V) curve of the GaInAs junction has an almost flat slope around the operating point. In general we have found this to be the case for the GaInAs junction when there is an external applied voltage of 1.2 V on the device. Application of voltage bias of 1.2 V has shown to move the operating point of GaInAs to the tail of the exponential curve, where the linear form is valid and the influence of shunts is smaller.

The presence of shunts in the device alters the equations described above since shunt sites cause alternative paths for the current, thus lowering the amount of emission and coupling

current. The equivalent circuit of a double-junction device taking into consideration shunt effects is shown in Figure 22. Shunt resistance is of major influence when the voltage of the device is absent and for that reason zero voltage was applied on the device. As mentioned above the application of voltage bias removes the shunt resistance effects since it moves the operating point of the current-limiting junction towards short-circuit conditions.

(3.3) in the presence of shunts is modified as follows

$$I_{out} = I_{bias,top} - I_{rec,top} - I_{sh,top} \tag{3.5}$$

While (3.4) in the presence of shunts becomes

$$I_{out} = I_{bias,mid} + I_{sh,mid} + I_{LC} \approx I_{sh,mid} + I_{LC} \tag{3.6}$$

As shown in (3.6) the presence of shunt current causes alternative paths for the current and thus the coupling current should be reduced. As a result it is expected that junctions with different shunt resistances will yield different coupling efficiency and currents.

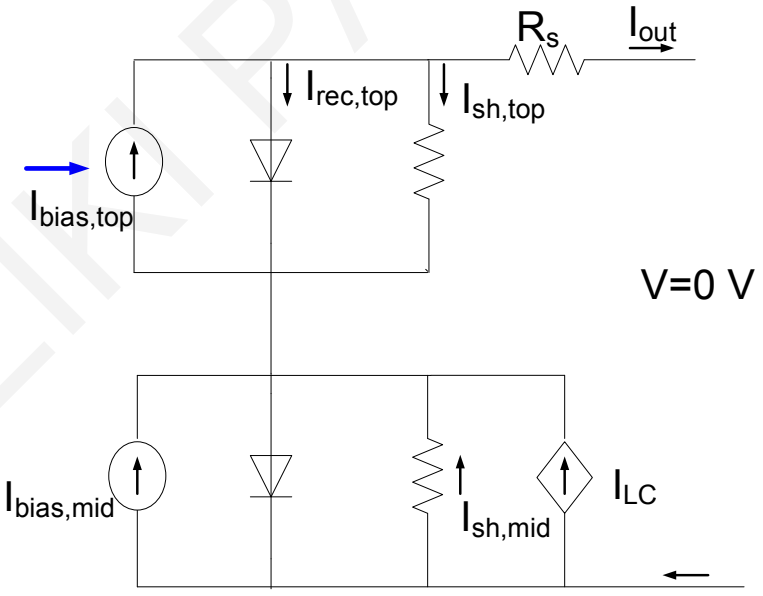

Figure 22: Equivalent circuit model of a double junction at zero voltage bias where the shunt resistance is of major influence.

3.3.2 Physical Model of junction in the presence of shunts

A physical two-dimensional axisymmetric model was also developed to investigate the impact of the shunts vertically in the device. This approach takes into consideration the impact of local ohmic shunts unlike the circuit model presented above which assumes homogeneous shunting in the cell. COMSOL was used for the solution of the current continuity equations for electrons and holes coupled with Poisson's equation for the solution of the electric field. The model simulates the middle $Ga_{0.99}In_{0.01}As$ junction. Due to the very low amount of Indium present in the middle junction, the GaInAs material was treated as GaAs. In the simulations only the current limiting GaAs junction was considered since modelling of all the junctions of the multi-junction device is a very complex task. Modelling of the GaAs junction with different shunt density has been performed in order to obtain the luminescent emission which will subsequently be compared with the experimental results thus indicating the impact of shunts on luminescent emission and therefore coupling current in different shunt resistance devices.

In an attempt to develop a realistic model for GaAs, the detailed doping concentration as well as the height of the junction is required. Two different series of devices were investigated in this chapter. Figure 23(a) shows the schematic and detailed doping concentrations of the GaAs junction investigated in this section and it corresponds to the structure of the S series devices used in this work. The junction has a n-p design with overall height of 2 μm. Figure 23 (b) shows the two-dimensional structure of the GaAs junction. The height of the simulated junction was set to 2 μm as in the real device. However, a smaller area of the device was considered for calculation simplicity. Thus, the radius of the simulated junction was chosen to be 15 μm. The depletion region as can be clearly observed in the graph lies at z=0.2 μm from the surface. In the two-dimensional illustration of Figure 23(b) the defect is shown to cross the depletion region and to have a radius of 7.5 μm. In order to build a reliable model for the defect states in a semiconductor we treat them as degenerate semiconductors with metallic behaviour (tunnel junctions). This approach is reasonable since in defects the conductivity of the material increases locally and can resemble the presence of a metal in the region. The carrier concentration inside the shunts was chosen to be 10^{22} cm^{-3} for our simulation. We selectively place strongly p-doped acceptor states ($N_A=10^{22}$ cm^{-3}) in the p-region and n-doped donor states ($N_D=10^{22}$ cm^{-3}) in the n-region. The higher doping densities inside the defects were simulated

with two Gaussian distributions in each region (n and p) which overlap in the depletion region. The Gaussian peaks in the n and p regions of the junction were selected to be at z=0.15 μm and z=0.25 μm from the surface respectively. Both Gaussian distributions were selected to have the same doping concentration and standard deviation of 0.1 μm. Thus, the height of the defects was set to 0.2 μm (from z=0.1 μm to z=0.3 μm from the surface). In this way, defects cross the depletion region and are in contact with neutral regions on both sides as shown in Figure 23(b). The net doping concentrations along the z-axis at r=9 μm (outside defect) and at r=3 μm (inside defect) are presented in Figure 24(a) and Figure 24(b) respectively. Direct recombination was used in the bulk (region outside defects) while inside the defects Auger recombination was considered.

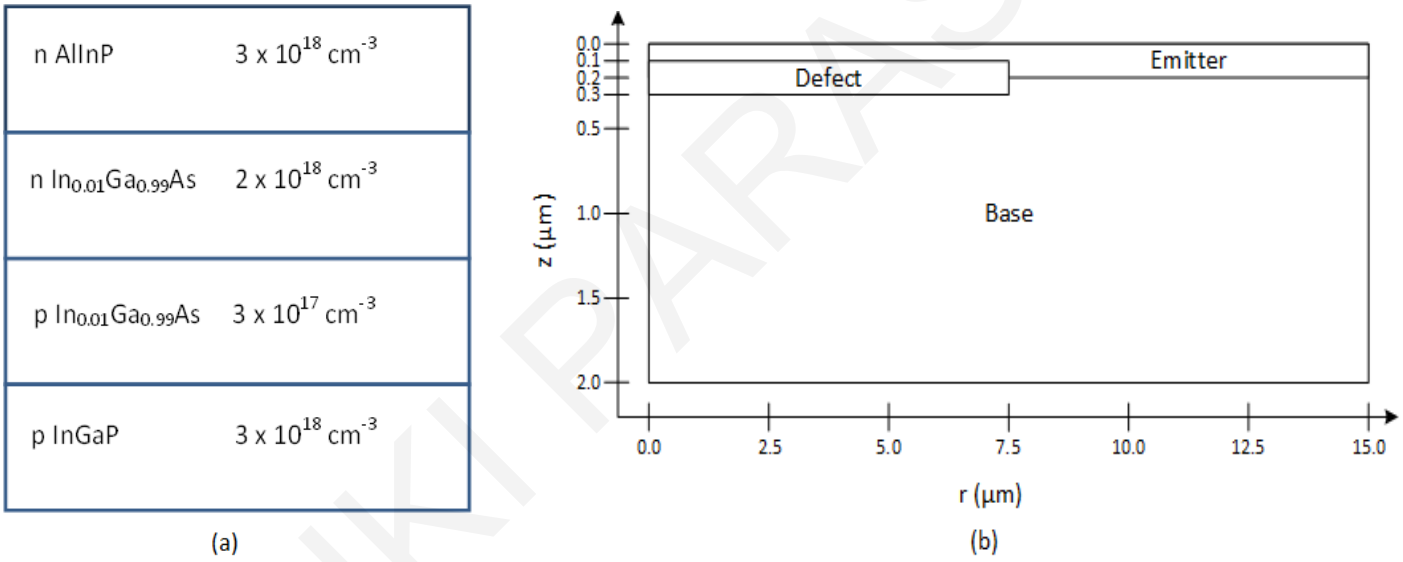

Figure 23: (a) Schematic illustration of the investigated GaInAs middle-junction and (b) two-dimensional illustration of the modelled junction. The defect has a radius of 7.5 μm and height of 0.2 μm.

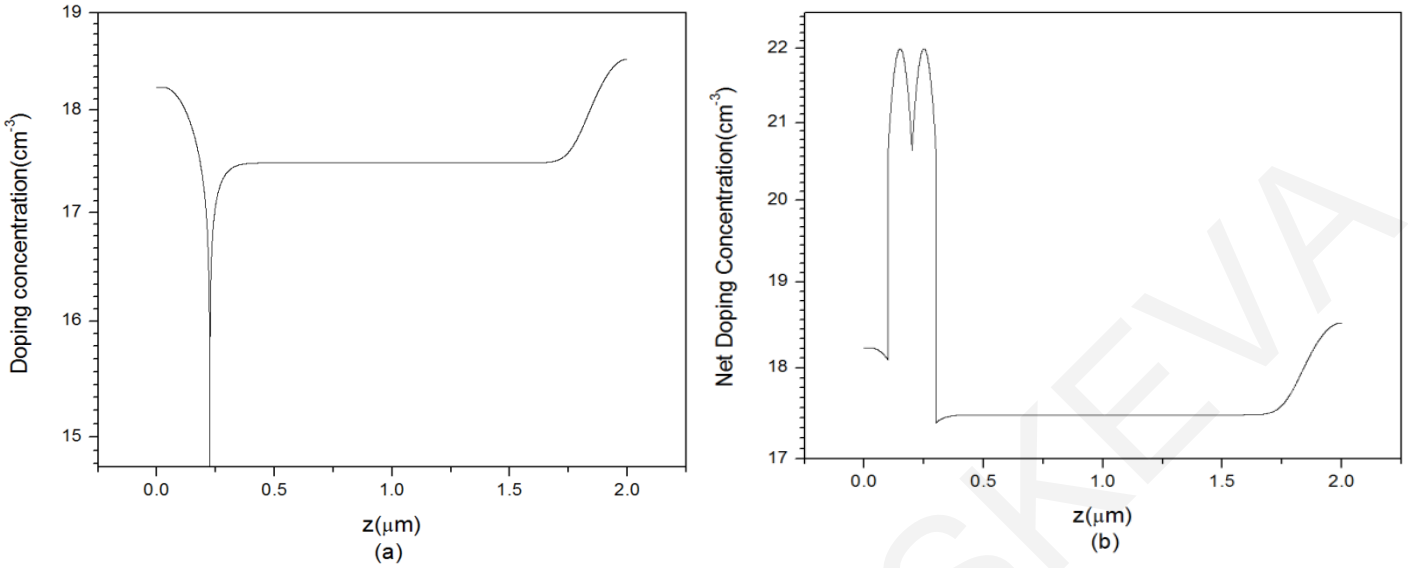

Figure 24: Doping concentration at radial distance of (a) r=9 μm and (b) r=3 μm. The doping concentration is presented in logarithmic scale.

For the simulation of the p-n junction the current-continuity equations for the description of electrons and holes coupled with Poisson's equation for the solution of the electric field have been solved. Drift-diffusion equations define the electron and hole current densities, J

$$J_n = -q\mu_n n\nabla V + qD_n\nabla n \tag{3.7}$$

$$J_p = -q\mu_p p\nabla V - qD_p\nabla p \tag{3.8}$$

where n and p are the electron and hole concentrations respectively, D_n, μ_n and D_p, μ_p are the diffusion coefficients and mobilities of electrons and holes respectively, and V is the electric potential. The current continuity equations are given by

$$\frac{\partial n}{\partial t} = -\frac{1}{q}(\nabla . J_n) - U_n \tag{3.9}$$

$$\frac{\partial p}{\partial t} = -\frac{1}{q}(\nabla . J_p) - U_p \tag{3.10}$$

The electric field is given from Poisson's equation

$$\nabla . (\varepsilon\nabla V) = -q(p - n + N_D^+ - N_A^-) \tag{3.11}$$

where N_A and N_D are the doping concentrations of the ionized acceptors and donors in the p- and n-type side respectively and ε is the material permittivity.

The boundary conditions are illustrated on the modelled structure in Figure 23(b). The Newmann boundary conditions represent zero current flow at the two sides.

$$\hat{n}.\overrightarrow{J_n} = 0 \tag{3.12}$$

$$\hat{n}.\overrightarrow{J_p} = 0 \tag{3.13}$$

Continuous hetero-junction exists at the interface between defect and actual semiconductor material since current continuity equations exist in both areas but with different doping profile. The same holds for the interface between the n- and p-side of the junction.

$$D_1 = D_2 \tag{3.14}$$

$$E_1 = E_2 \tag{3.15}$$

A constant mobility for the electrons and holes has been taken into consideration. The diffusion coefficients are estimated from Einstein's relation. The model parameters are given in Table 3.

Table 3: Basic model parameters used in simulation.

Model Parameter	Value
Base doping (N_A)	3x 10^{17} cm^{-3}
Emitter doping (N_D)	2x$10^{18}$$cm^{-3}$
Defect thickness (d)	0.2 μm
Electron mobility (μ_n)	8500 cm^2/V.s
Hole mobility (μ_p)	400 cm^2/ V.s

The two-dimensional model was used to obtain the changes axially (z-axis) in the vicinity of the defects. The voltage, electric field, chemical potential and recombination rate on the z-axis at radial distances of r=3 μm (inside the defect) and r=9 μm (outside the defect) can be observed in Figure 25. Since the defect has a radius of 7.5 μm, at r=3 μm the shunt region is crossed while at r=9 μm radial distance the region of the bulk without the defect is considered. Thus, at r=3 μm the depletion region is surrounded by a defect state as Figure 23(b) shows. The voltage bias was set to 0.9 V in order to excite the junction close to its open-circuit voltage and cause forward bias in the GaAs junction. Forward biasing of the device is required in order to cause luminescent emission from the junction, which can then be simulated. The electric potential changes significantly in the presence of a defect in the device (see Figure 25a). At radius r=3 μm, the electric potential is reduced in the region z=0.25 μm while it is increased at z=0.15 μm. These two points lie within the defect state. Thus the electric potential inside the

defect in the n-region is increased while inside the defect in the p-region is reduced. The increased doping concentration in the defect causes increase of the potential difference between the two-sides (n and p) of the junction inside the depletion region. The increase is around 0.43 V. The electric field across the z-axis for the two radial distances (3 and 9 μm) is shown in Figure 25(b). At radius r=3 μm, where the defect is located, the electric field inside the depletion region increases significantly (around three orders of magnitude higher) compared to the field present outside the defect at 9 μm. The increase of the electric field inside the depletion region is related to the increase of the doping concentrations inside the shunts locally. In the region outside the shunts (r=9 μm) the electric field in the depletion region is very small. Furthermore, at the edges of the defect state (at z=0.1 μm and z= 0.3 μm) a negative electric field is apparent. The electric field inside the defect indicates also the depletion width narrowing due to higher doping densities. As shown in the inset of Figure 25(b) the depletion region width outside the shunt sites is broad (peak width of 150 nm) while in the region of the shunt at r=3 μm it appears to be only 1.6 nm. Therefore, the introduction of a defect in a material causes local reduction of the depletion region width. Furthermore, the results in Figure 25(c) show the impact of the defect on the chemical potential of the junction. The chemical potential inside the depletion region equals the forward voltage (0.9 eV) everywhere in the device since quasi Fermi levels are flat in the inner of the space charge region [39]. In the defect region, the chemical potential reduces significantly outside the depletion region along the z-axis and this indicates that the upper and lower layers of the shunt are affected significantly. Therefore the potential in the presence of defects is reduced significantly on the z-axis inside as well as outside the defects thus affecting the local potential in the other layers (top and bottom). Thus, the shunt in the middle junction affects the local bias of the top and bottom junctions locally. The recombination rate was also investigated in the presence and absence of shunts as shown in Figure 25(d). The results show an increase in the recombination rate in the depletion region at the radial distances where the shunt is located (r=3 μm) due to the increase of the chemical potential just inside the depletion region. Another important observation is that in the presence of shunts, the recombination rate outside the depletion region along the z-axis is reduced considerably. In the presence of defects (at r=3 μm) a sharp decrease of the recombination rate is present along the z-axis outside the depletion region due to the drop of the chemical potential.

The model of a GaAs junction in the presence of shunts in the depletion region was further utilized for the investigation of the impact of voltage bias and degeneracy on the electrical and physical parameters around the defect.

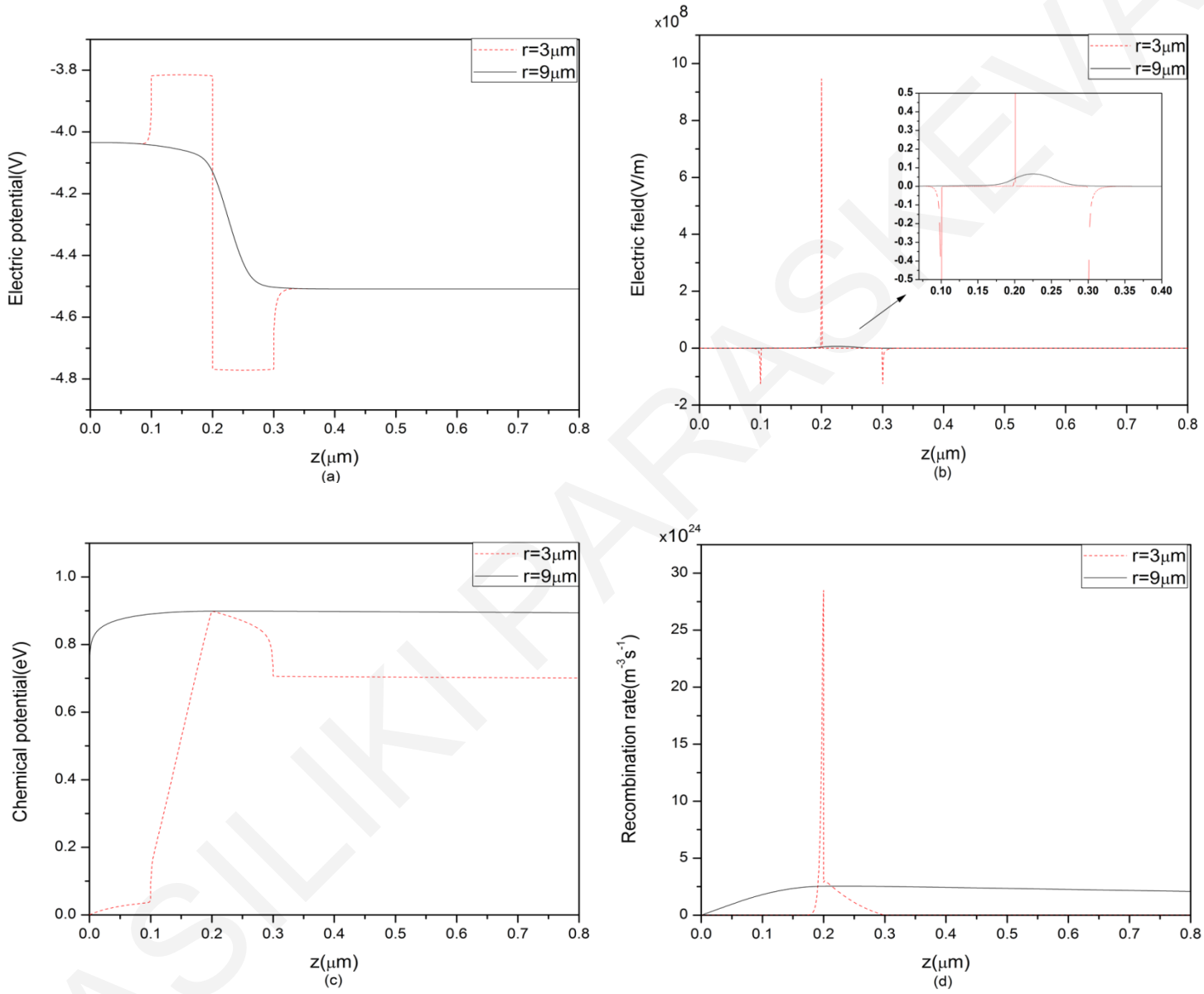

Figure 25: Modelling results of the (a) electric potential (b) electric field (c) chemical potential and (d) recombination rate at a radial distance of 3 μm and 9 μm indicating the changes for each parameter in the z-axis. The radius and the height of the simulated shunt are 7.5 μm and 0.2 μm, respectively.

3.3.2.1 Physical Model of junction in the presence of shunts -Impact of voltage bias

An investigation of the electric parameters of the solar cell over a broad voltage range has been explored. Application of different voltage bias on the device will provide information about the local changes of the field around the defects in the presence of different potential.

The built-in potential of the junction is around 1.4 V in the region outside the defect and 1.9 V in the region inside it since the higher dopant concentration in the defect region increases the built-in potential. Voltage bias in the range between 0.1 - 0.9 V was applied to the junction and the chemical potential, electric potential, electric field and space charge density were examined in the local surroundings of the defects and outside them. The temperature of the device was set to 298 K and the doping concentration of the defect to 10^{22} cm^{-3}. Figure 26(a) and Figure 26(b) present the chemical potential across the z-axis and at radial distances of r=9 μm (outside defect) and r=3 μm (inside defect) respectively at different voltage bias.

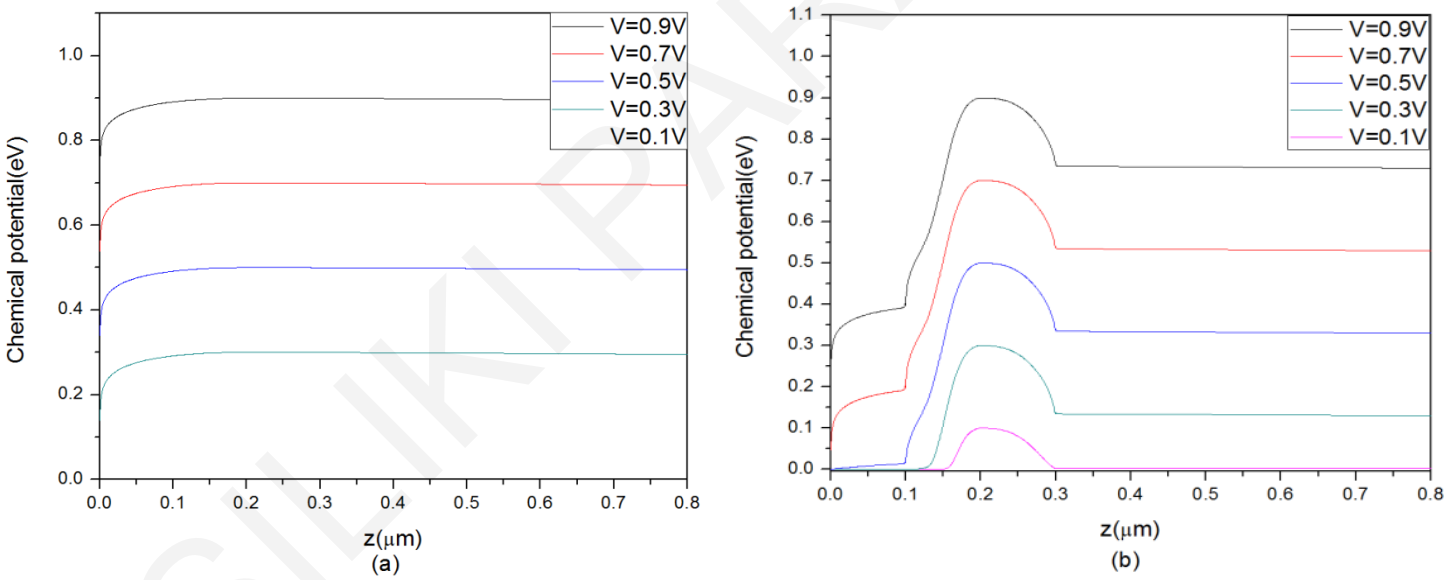

Figure 26: Chemical potential along z-axis (a) outside defects (r=9 μm) and (b) in the region of the defects (r=3 μm) with the application of different forward voltage bias.

As found in the previous investigations the chemical potential in the absence of defect states remains almost constant across the z-axis and has values roughly equal to the applied voltage while at radial distances where the defect is present, the chemical potential reduces significantly across the z-axis due to the presence of the defects. Even though similar chemical potential reduction appears for all voltage biases, the amount of reduction compared to the

initial chemical potential is larger at lower voltage biases indicating that in those conditions the impact of defects in their local surroundings is more pronounced. The reduction of the chemical potential in the region of the defect was found to decay exponentially against the voltage bias (see Figure 27). For comparison purposes the chemical potential reduction against voltage bias at radial distance of r=9 μm outside the defect is plotted on the same graph. The chemical potential reduction in the region outside the defects is much lower compared to the chemical reduction inside. Therefore the chemical potential reduction is affected significantly by the presence of shunts in the solar cell. The maximum reduction was obtained at lower applied voltages in all regions under investigation. According to [40] the effect of the shunt on the local potential is more pronounced for smaller than for higher injection current densities and therefore higher applied voltages in good agreement with the simulated results presented here.

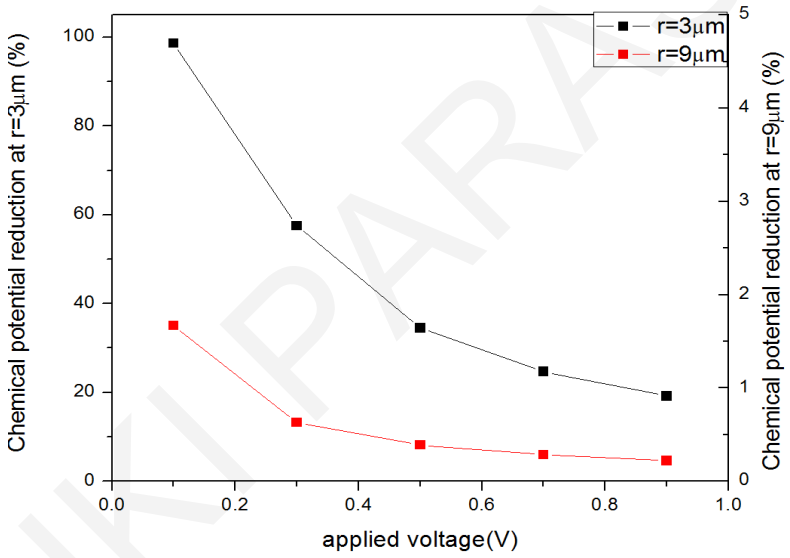

Figure 27: Chemical potential reduction along the z-axis at different forward voltage bias in the region inside and outside the defect. It is clearly observed that the impact of the defect on the chemical potential becomes higher at lower voltage bias.

The electric potential was also examined in the region outside and inside the defects at different voltages (see Figure 28(a) and Figure 28(b)). The electric potential represents the difference between the built-in potential and applied potential (voltage bias). The electric potential changes with the application of different voltage bias in both radial distances under investigation. The electric potential increases in the presence of lower applied voltage since the device at lower applied voltage is at lower forward bias conditions.

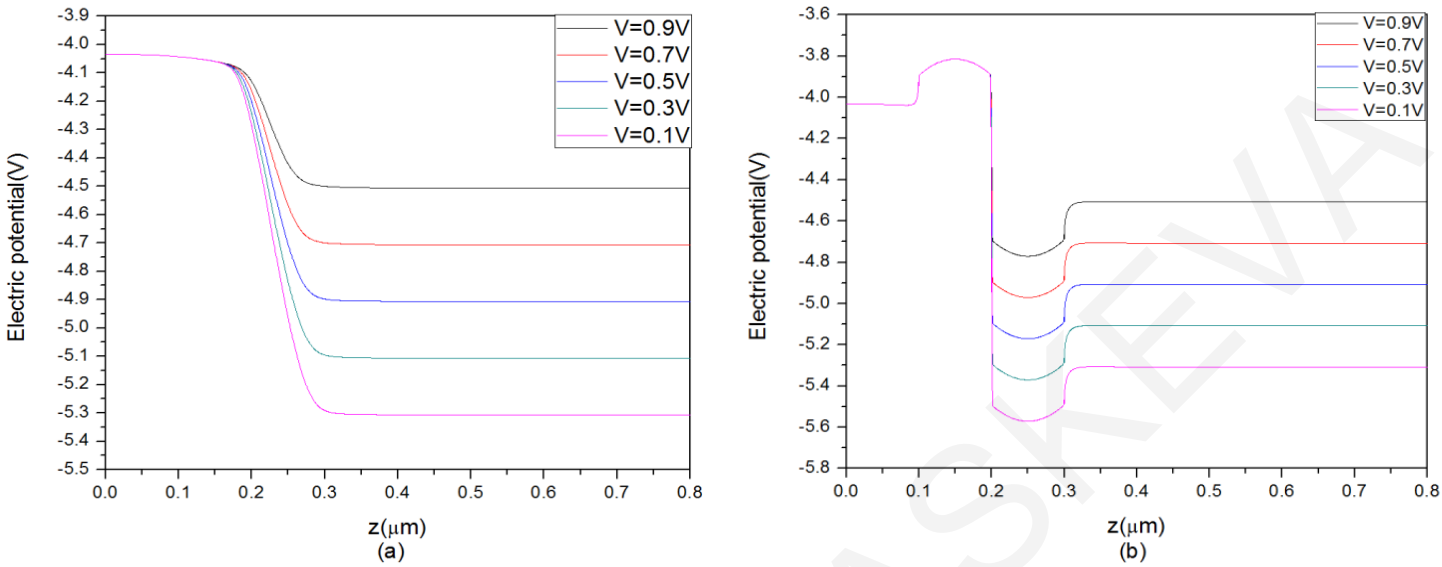

Figure 28: Electric potential along the z-axis at different forward voltage bias and at radial distances of (a) r=9 μm and (b) r=3 μm.

As can be seen in Figure 28(a) and Figure 28(b) the electric potential on the emitter in both radial distances under investigation remains the same for all voltage biases while this varies with the voltage bias on the base. The different electrical potential on the p-side of the depletion region is attributed to the fact that the applied voltage changes on the p-side of the device. Specifically, the voltage of the n-side (front contact) is always set to 0 V and different voltage is applied on the p-side (back contact).

Furthermore the electric field at different radial distances and voltages was examined. As shown in Figure 29(a) and Figure 29(b) higher increase of the electric field intensity inside the depletion region is apparent at lower applied voltages due to the higher electric potential and thus wider depletion region. As depicted by the results in Figure 29 the electric field increases more with the applied voltage in the region of the defects and thus the defect region is more sensitive to the change of the applied voltage. The electric field at the edges of the defect state (z=0.1 μm and z=0.3 μm) does not exhibit any changes with the application of different voltage. The space charge density at different radial distances and voltages is shown in Figure 30.

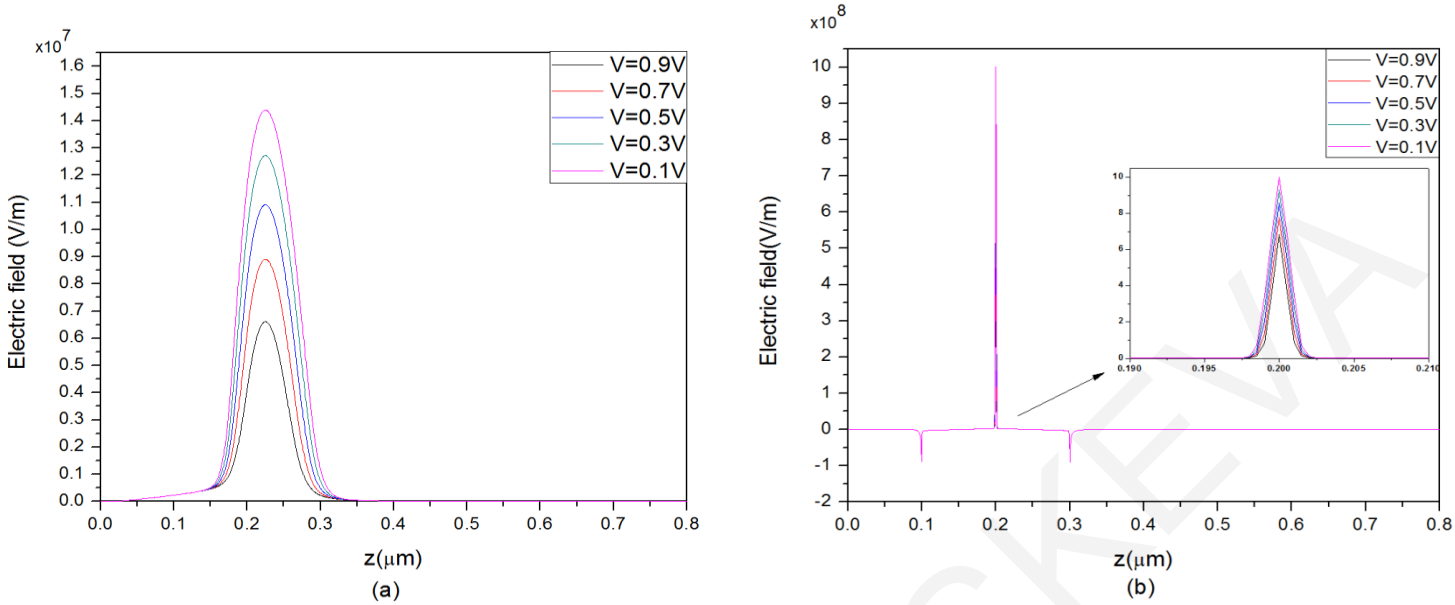

Figure 29: Electric field along the z-axis at different forward voltage bias and at radial distances of (a) r=9 µm and (b) r=3 µm

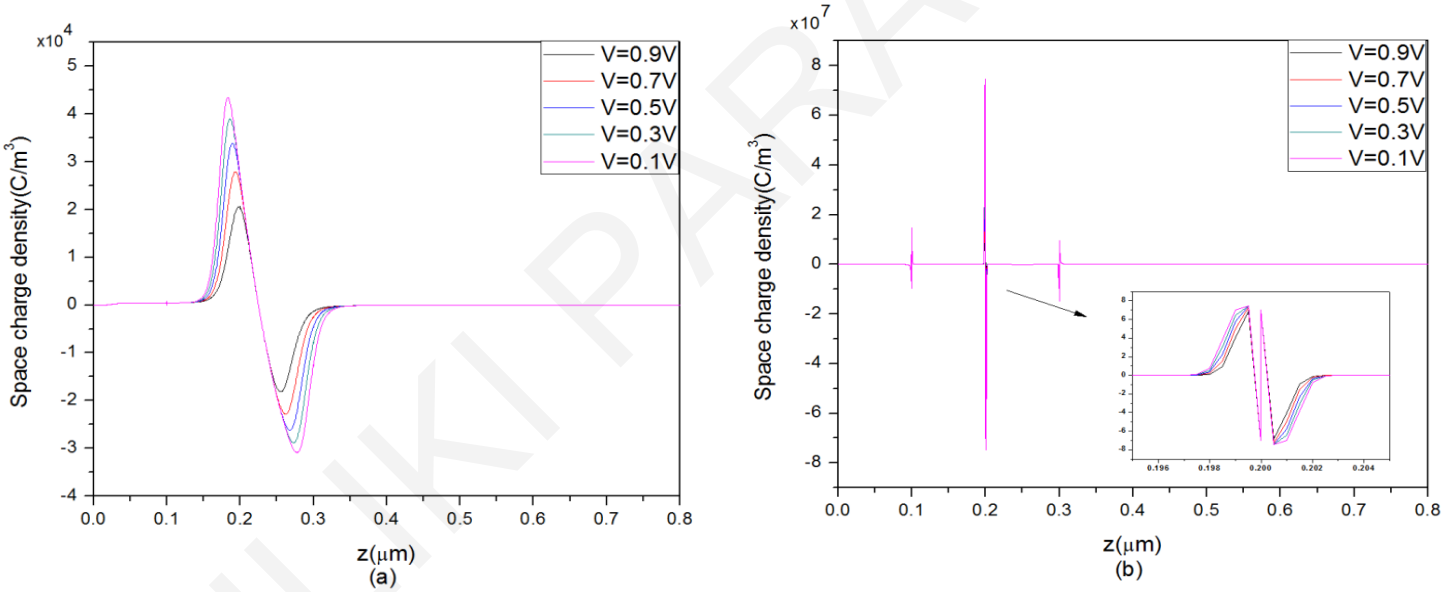

Figure 30: Space charge density along z-axis at different voltage bias and at radial distances of (a) r=9 µm and (b) r=3 µm.

Results have shown that in all radial distances the space charge density changes with the application of different voltage bias due to the change in minority carrier concentration. The space charge density at radial distances outside the shunts changes less with voltage compared to space charge density at radial distances where the defect is located. So shunts introduce more sensitivity on the voltage dependence of space charge density in agreement with the electric field results.

Results for the space charge density in Figure 30 indicate also the widening of the depletion region width at lower application voltages. The depletion region width increases in the presence of lower applied voltage. The widening is lower at radial distances inside the defect sites. Since higher dopant concentration exists in the defect side, the change in applied voltage will not cause significant change to the depletion width.

3.3.2.2 Physical Model of junction in the presence of shunts -Impact of doping density

Different doping densities of defects were used next in order to examine the effect of doping on the electric field around the defects. Since the model used for the simulation of defects treats the defect states as degenerate semiconductors then the doping density determines the degeneracy of the defect state and the impact of the defect on its surroundings. Weak shunts correspond to degenerate semiconductors with lower doping densities (10^{19} cm^{-3}) while stronger ones correspond to semiconductors with higher doping concentration (10^{23} cm^{-3}). Defects with five different doping concentrations were investigated (10^{19}, 10^{20}, 10^{21}, 10^{22} and 10^{23} cm^{-3}). Apart from these doping concentrations, a concentration of 10^{18} cm^{-3} was also examined. This concentration approaches the case where no defect is introduced in the device. The results for the electric and chemical potential and also the electric field and space charge density in the region of the defect are depicted in Figure 31. The temperature of the device was set to 298 K and the voltage bias applied on the device was 0.9 V in order to excite the junction close to its built-in potential. The chemical potential reduction as shown in Figure 31(a) is more pronounced at a higher doping density of defects indicating that as the doping density increases the influence of the defect on its surroundings becomes more pronounced. Particularly, reduction of the chemical potential along the z-axis is greatly enhanced at a doping density of 10^{23} cm^{-3}. Chemical potential reduction in that case reaches 46% and thus the impact of shunts on the device becomes more important. The chemical potential reduction is correlated with the quasi-Fermi levels E_{Fn} and E_{Fp}. As the doping density increases, the difference of quasi-Fermi levels becomes lower.

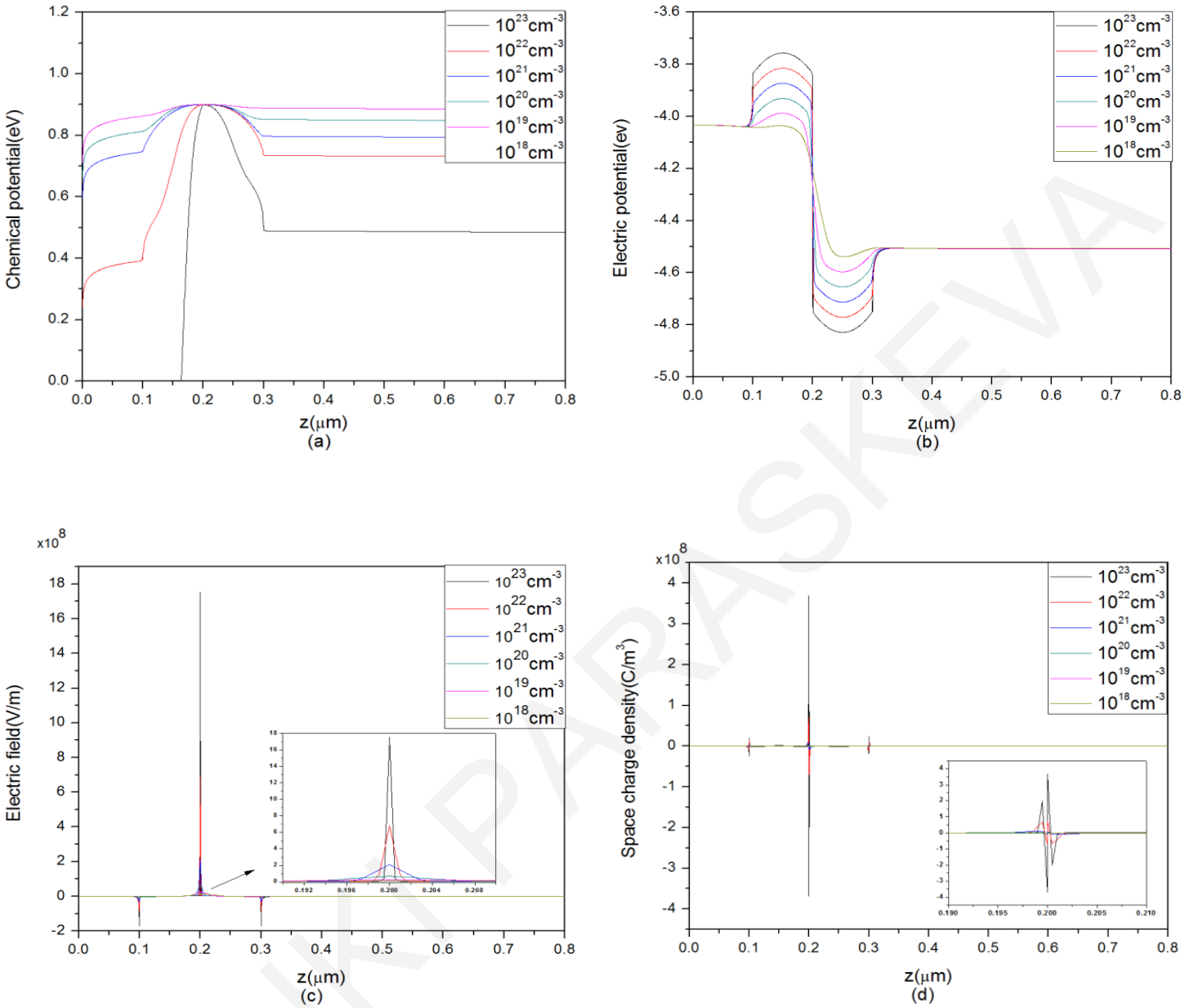

Figure 31: Modelling results for the (a) chemical potential (b) electric potential (c) electric field and (d) space charge density along the z-axis in the region of defects (r=3 μm) for different doping concentrations.

The electric potential increases due to the presence of defects as mentioned before. Higher built-in potential is exhibited in the depletion region in the presence of defects with higher doping profile resulting in higher electric potential (see Figure 31(b)). Although these changes in the fields are local they affect the total potential of the device.

Furthermore, the electric field has been examined at different doping concentrations of the defect state as depicted in Figure 31(c). The electric field in the depletion region significantly decreases as the doping concentration of the defect decreases. Moreover, a narrower electric

field is observed at higher doping densities since the depletion region width is inversely proportional with the doping concentration. The negative electric field at the edges of the defect state changes also, with lower electric field present at higher doping concentrations.

The space charge density has also been investigated over a range of doping concentrations. The increase of the doping density of donors and acceptors causes an increase of the space charge density as shown in Figure 31(d). The higher the doping density, the higher the increase of the space charge density is.

The above results demonstrate the impact of weak and strong shunts on their local surroundings. Higher doping concentrations inside the degenerate semiconductor (defect) have a higher impact on the field close to the defect. Thus, as the metallic behaviour of the defect increases, the influence of the defect on its surroundings becomes more pronounced. The results are in agreement with previous publications that indicate the higher voltage reduction in the region of shunts with decreasing shunt resistance [41].

After the investigation of the impact of the shunts on the local surroundings, the luminescent emission from two different shunt resistance devices was estimated by simulation in order to validate the experimental results. The devices were set to forward bias conditions in order to increase recombination and thus light emission. Voltage biases close to the open-circuit voltage have been used to cause forward bias on the GaAs junction and maximize recombination current. Previous studies of spontaneous emission demonstrated the relation between radiative recombination emission with voltage bias and chemical potential [42]. The different number of defects present in the two devices is expected to affect the luminescence emitted by the devices.

According to the reciprocity theorem [40], [43] the EL intensity φ_{em} of a p-n junction solar cell emitted at any position of the solar cell surface is given by:

$$\varphi_{em}(E_\gamma, r, \varphi) = Q_e(E_\gamma, r, \varphi)\varphi_{bb}(E_\gamma)\exp(\frac{qV(r,\varphi)}{k_B T}) \quad (3.7)$$

where Q_e is the local External Quantum Efficiency (EQE) at a given photon energy E_γ, kT/q is the thermal voltage and φ_{bb} represents the spectral photon density of a black body [40]. The voltage V(r,φ) at a given position represents the internal junction voltage at that specific

position and reflects the resistive losses. Taking into consideration the local potential at any position (r,φ) on the surface, the luminescent emission will be estimated. It is expected that materials with different defect density will demonstrate different voltages and luminescent efficiency and thus the emission from a junction in the forward bias region can be simulated by correctly regarding local ohmic shunting in the tandem device.

In order to predict luminescent emission under forward bias, the potential at any point of the device should be known. Different amounts of shunts were introduced in the model in order to simulate different shunt resistance devices and the potential at each point was calculated. Dark EQE measurements from two multi-junction solar cells (labelled S5 and S3) have demonstrated that device S5 has higher shunt resistance while device S3 has lower shunt resistance (the specifications of the cells and the experiments are provided in detail in the next section 3.3.3). Thus the device with the high shunt resistance (low shunt density) was assumed to be S5 while the device with the lower shunt resistance (high shunt density) was assumed to be S3. Interactions between different shunt sites were neglected. The luminescent emission was then calculated according to (3.8). (3.7) can be simplified to (3.8) with the assumption that the exponential dependence of the internal junction voltage V(r,φ) variations has a much stronger impact on the luminescent intensity than possible variations of quantum efficiency (Q_e) [40]. Thus luminescent emission depends only on the local variations of the voltage.

$$\varphi_{em}(r,\varphi) \sim \iint \exp\left(\frac{qV(r,\varphi)}{k_B T}\right) r dr d\varphi \tag{3.8}$$

Simulated results for the emission from the devices demonstrates that the device with the higher defect density presents slightly lower luminescent emission compared to the one with lower density of defects (see Figure 32a). Higher defect density causes higher reduction of the potential and further lowers luminescent efficiency which determines the number of photons directed towards the bottom junction and thus the optical interactions between junctions and coupling effects. The simulated luminescent emission from the solar cells is plotted against recombination current. The results validate the experimental results taken from both devices (see Figure 32b) demonstrating the influence of shunt sites in the luminescent emission efficiency of the device. The small differences between the simulated luminescent emission from the two devices might be due to the fact that in our simulations only a very small number

of shunts was considered. The difference between the numerical and experimental recombination current results is attributed to the fact that different material was forward biased as explained earlier and also different excitation power was used each time. For the simulations, GaAs was forward biased with voltage only, whereas during the experimental procedure GaInP was excited with voltage and light simultaneously. After the modelling procedure, measurements on different shunt resistance devices have been performed in order to detect the impact of shunts on coupling effects (see next section).

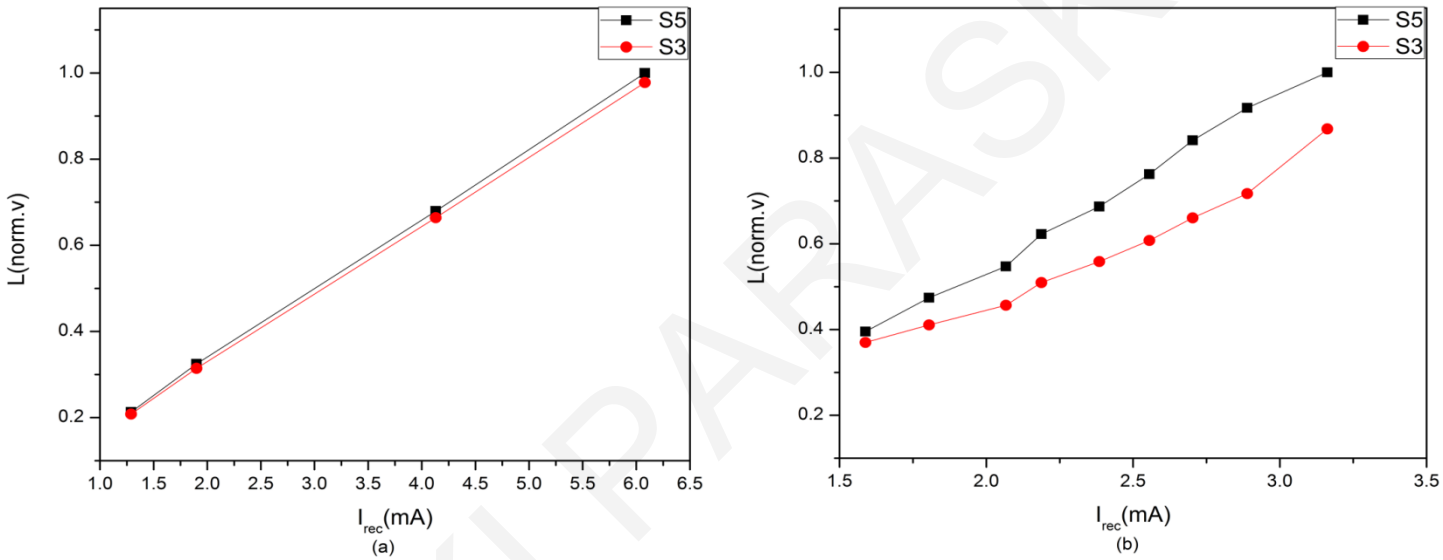

Figure 32: (a) Simulated luminescent emission (L) of the middle GaAs junction against recombination current for devices S3 and S5. The luminescent emission was integrated over the surface for a specific photon energy. (b) Experimental integrated luminescent emission (L) of the top InGaP junction against recombination current for the same devices.

3.3.3 PL results-Impact of shunt resistance

Prior to the PL investigation of the cells, dark EQE is required in order to extract the relative magnitude of the shunt resistance in the cells and thus the material quality. The magnitude of the shunt resistance in the junctions provides a measure for the material quality of each junction in the photovoltaic devices. Consequently, knowledge of the shunt resistance of the junctions can be used to extract conclusions about the correlation of shunt resistance and therefore material quality with luminescent coupling effects.

The two different series of triple-junction GaInP/GaInAs/Ge devices (A, S) have been examined with dark EQE method. A number of cells of the A and S series has been investigated and the two devices from each series which presented the largest differences in dark EQE were chosen to indicate the effect of the shunt. The comparison was undertaken for the devices that belonged to the same series in order to clearly investigate the effect of the shunts and no other parameters. Dark EQE of the four selected devices is presented in Figure 33. The dark EQE signal above 900 nm which is the wavelength region of Ge is almost zero in all cells and it is not presented in the graph.

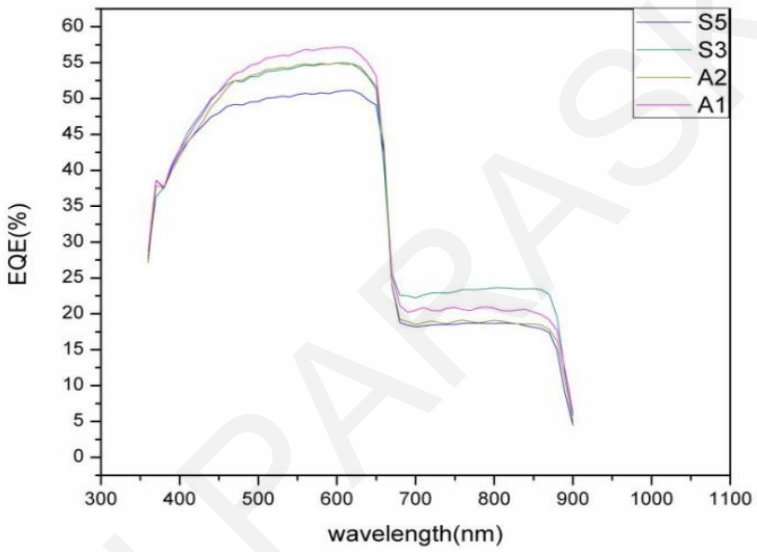

Figure 33: Dark EQE of four different multi-junction devices. The effect of different shunt resistances in the dark EQE signal of the devices is clearly observed.

Previous investigation of dark EQE [25] in triple-junction devices has shown that dark EQE measurements of the four devices in Figure 33 refer to the case of high shunt resistance in the top junction and low shunt resistance in the middle and bottom junction: the dark EQE of the device is a consequence of current leakage through GaInAs and Ge, giving rise to an increased EQE in the wavelength region of the top junction due to low shunt resistance of the middle and bottom junction. The shunt resistance of the top junction is much higher than that of the middle and bottom one, as inferred by the very small EQE signal observed in the response region of the middle and bottom junction in the dark measurements. The presence of different shunts in devices of the same series results in different radiative efficiency between cells and different coupling currents.

Devices A2 and S5, which presented lower dark EQE compared to their counterparts of the same series as shown in Figure 33, are of better quality and their equivalent circuit approaches the electrical circuit in the absence of shunt resistance shown in Figure 21. This assumption is very crude since the shunt resistances of those devices are finite but it can be used for the purposes of comparison. However the equivalent circuit of cells with lower quality materials such as A1 and S3 (indicated by the higher dark EQE signal) approaches the circuit in the presence of shunts in Figure 22 and should include shunt resistances in both junctions. The impact of the shunt resistance of both top and middle junction is significant for coupling effects since the presence of shunts creates additional paths for the current and acts to lower the coupling current.

In order to directly measure the coupling current in the four devices examined before, the voltage and current of the devices was measured during voltage dependent PL measurements. The results are depicted in Figure 34(a) and Figure 34(c). Voltage dependent PL was performed at fixed light intensity conditions of the blue and infrared light sources. Under these conditions the output current of the device is the limiting current of the reversed biased middle InGaAs junction. The output current of InGaAs at each point of the curve is the coupling current plus the shunt current from the defects (3.6). The characteristic I-V curves of the devices were measured at light bias conditions of the top junction sufficient to generate 1.95 mA/cm^2 bias photocurrent at a voltage bias of 1.2 V. Furthermore, luminescent emission of the top junction at the band-gap edge (at 660 nm) was captured against recombination current (see Figure 34(b) and Figure 34(d)). The luminescent emission of the top junction determines the amount of coupling that gets directed towards the middle GaInAs junction. The coupling emissions of all devices were measured during excitation dependent PL at different light bias conditions of the top junction ranging from 5.4 - 9 mA/cm^2 and in the presence of voltage bias of 1.2 V. The recombination current was calculated from (3.3) since bias photocurrents and output currents can be measured directly. The shunt current was assumed to be zero for calculation simplicity. $I_{bias,top}$ represents the output current of the solar cell when a light bias is applied in the response region of the GaInAs junction (808 nm) in order to cause the GaInP junction to be current limiting. The procedure is described in detail in [28].

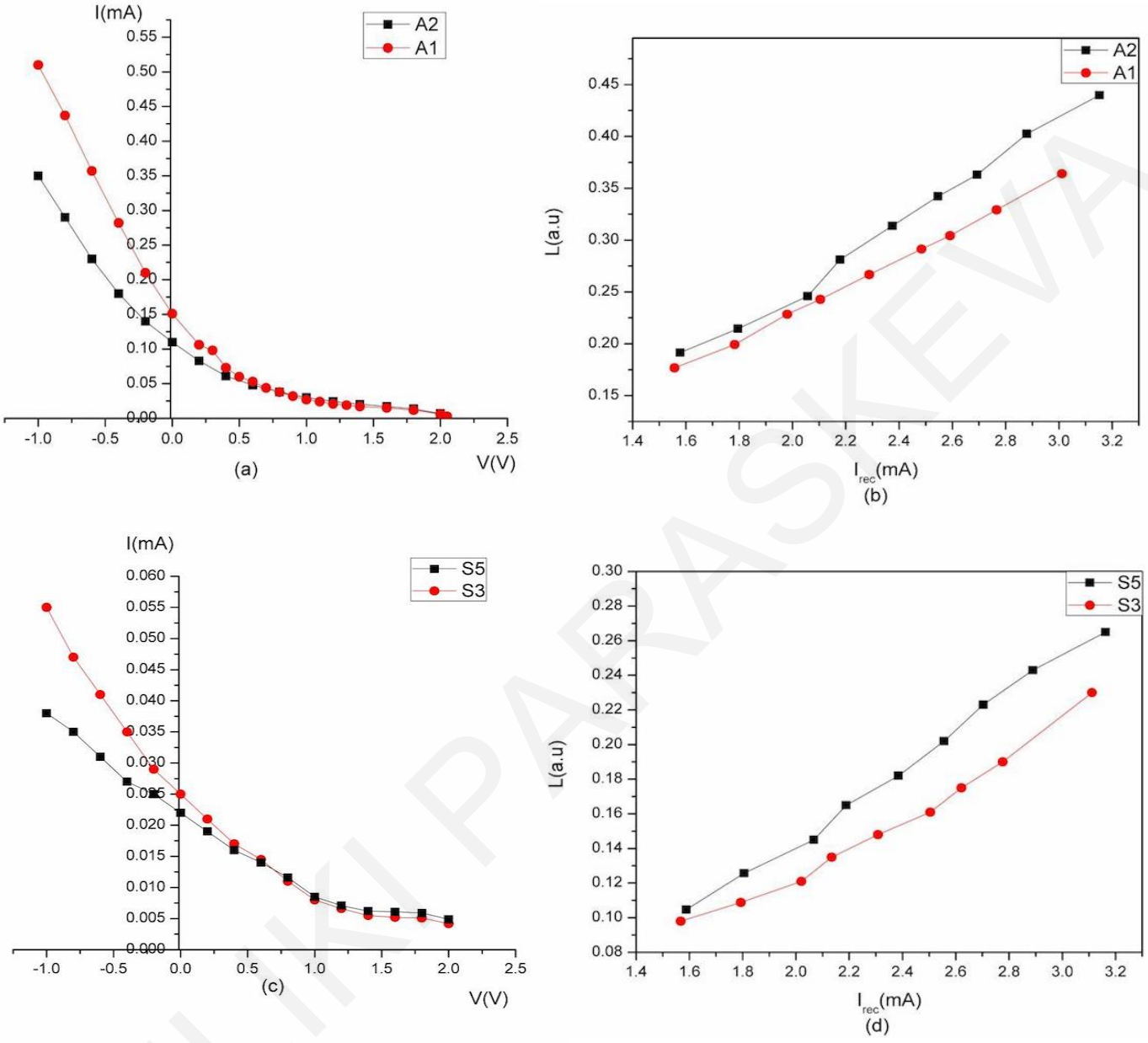

Figure 34: Measured I-V curves of the tandem solar cell for devices (a) A1 and A2 and (c) S3 and S5. Integrated luminescent emission (L) against recombination current for photocurrents of the top junction between 5.4-9mA/cm^{2}and in the presence of voltage bias of 1.2V for devices (b) A1 and A2 and (d) S3 and S5.

The low shunt resistance devices (A1 and S3) present higher output currents at low voltage biases (V<1V) compared to higher shunt devices (A2 and S5) due to the presence of shunts. At higher voltage bias (above 1 V), where the effect of the shunt is eliminated, the output current equals the coupling current (see 3.4). At voltages above 1 V and specifically at 1.2 V the output current, as can be observed in Figure 34(a) and Figure 34(c), is slightly higher in the high quality devices indicating higher coupling currents in those devices. This confirms the results

of Figure 34(b) and Figure 34(d) where luminescent emission from the better material quality samples is higher. However it should be noted that the difference in quality between materials of the same series is very small and large differences in coupling currents cannot be observed.

From Figure 34(a) and Figure 34(c) it is shown that application of a voltage bias of roughly 1.2 V can put the operating point of the junction under test close to short-circuit conditions and eliminate the shunt currents. The output current of the devices in that case follows (3.4) and the coupling efficiency coefficient can be easily calculated from (3.2). The coupling efficiency term represents the amount of recombination current that ends up as coupling current in the lower GaInAs junction. The currents were measured at various photocurrents ranging between 5.4-9 mA/cm^2. The coupling efficiency coefficient for the A series devices was found to be around 2.3% while for the S series it was around 1%. Linear fitting of the coupling current against recombination current as shown in Figure 35 gives a higher value for the coupling coefficient in the higher shunt resistance devices A2 and S5. The insets in Figure 35 give the slope of the fitting line along with its standard error. The slope corresponds to the coupling efficiency coefficient. Lower shunt devices (A1 and S3) give a slightly lower value for the coupling coefficient indicating that lower amount of recombination current results as coupling in the lower junctions.

All four cells under investigation present non-ideal I-V curves as depicted in Figure 34 indicating finite shunts. This evidence suggests that devices with almost ideal properties will have different coupling efficiency than that observed in Figure 35. Another important aspect observed in Figure 35 is the different coupling efficiency values obtained for the two different series devices. The S series devices show lower coupling efficiency indicating lower optical interaction between junctions. The different structural characteristics of each series devices are expected to play a crucial role in absorption and carrier generation recombination of carriers as well as in the transfer of carriers between junctions. The impact of the material structure on coupling effects will be investigated and discussed in detail in section 3.5.

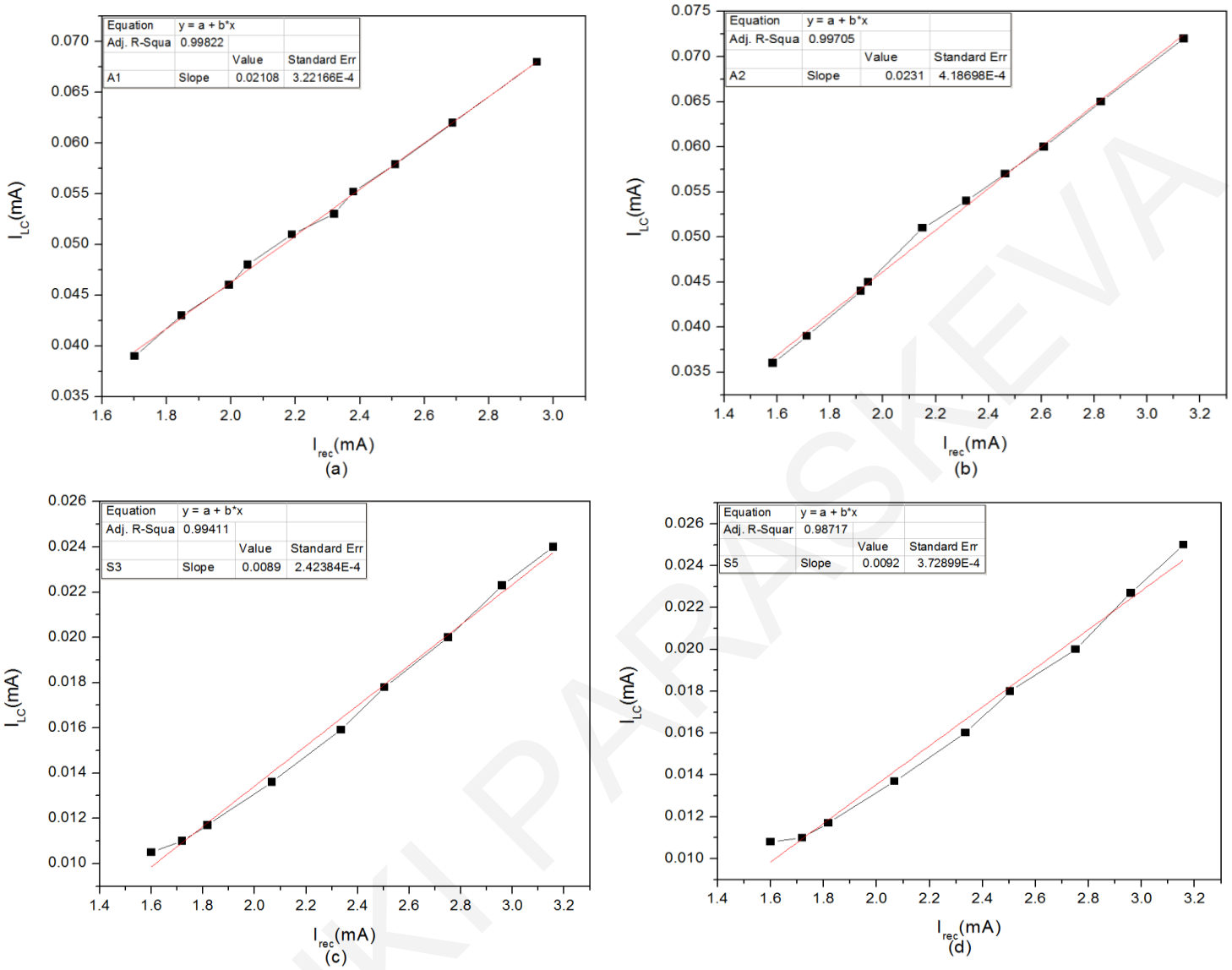

Figure 35: Coupling current against recombination current for photocurrents of the top junction between 5.4- 9 mA/cm^2 and at voltage bias of 1.2 V for device (a) A1 (b) A2 (c) S3 and (d) S5. The slope of the graphs corresponds to the coupling efficiency coefficient (α). Smaller values of (α) are present in lower quality materials.

3.4 PL analysis of coupling effects-Impact of temperature

The impact of the temperature on luminescent coupling effects has also been examined using voltage dependent PL measurements. These measurements have been carried out under fixed light bias conditions of the blue and infrared light sources in order to measure the characteristic current-voltage curve of the middle junction as well as to observe the temperature dependence of the cell. The selected light bias conditions in that case have been set in order to cause weak coupling effects in the device.

It is well known that the saturation current and therefore the generated recombination current depend on the energy gap and temperature [39]. The temperature factor is expected to have a significant impact on the recombination current. Temperature effects are significant since concentrator cells work far from the STC conditions and at temperatures that can exceed 80°C. For the investigation of the effect of temperature, voltage dependent PL was performed at a fixed light intensity of the blue and infrared light sources as mentioned above. Thus, the output current from the middle junction is measured over a wide range of voltage bias.

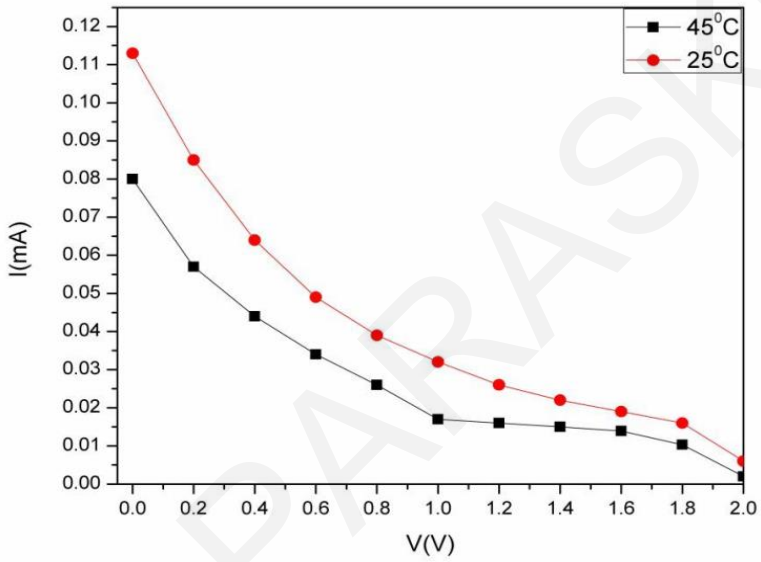

Figure 36: Characteristic I-V curve of GaInAs current limiting cell at different temperatures. Reduction of output current is observed at higher temperatures.

The characteristic curve of the device at different temperatures as displayed in Figure 36 demonstrates a reduction of the current of the order of 30% at voltage bias above 1V. Therefore the coupling current reduces by around 30% at higher temperatures. Reduction of the coupling current is related to the increase of the non-radiative processes in the device.

3.5 PL analysis of coupling effects-Impact of material structure

Excitation power dependent PL and voltage dependent PL of GaInP/GaInAs/Ge solar cell devices of different material structures have also been studied in order to demonstrate the impact of material design on coupling effects. Coupling effects from a lower bandgap junction to a higher bandgap junction can be possible in a multi-junction device due to the series connection of the junctions.

The experimental set-up used for the multiple wavelength PL measurements was based on two laser diodes with emission at 520 nm (green) and 785 nm (NIR) that were focused with a spot of 60 μm on the TJ solar cell surface. The emitted light by the samples was detected by a spectrometer sensitive in the wavelength range of 475-1030 nm, which covers the emission region of both the InGaP top cell and the InGaAs middle one. The experimental set-up is provided in Figure 37.

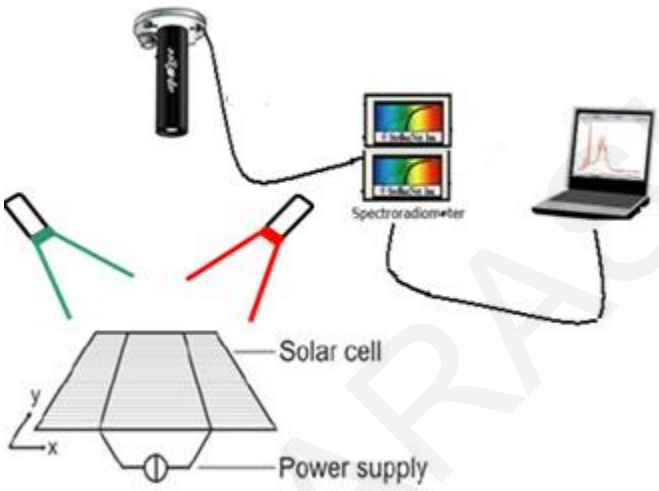

Figure 37: Double wavelength PL set-up used for the investigation of the material structure on coupling effects.

Initially, measurements were taken in the presence of only the green light source in order to obtain the luminescent emission of the top InGaP junction of the samples under visible light. Furthermore, these measurements demonstrated the material quality of the top InGaP junction of the different samples. Then, PL measurements were carried out in the presence of two excitation laser sources, the green and the NIR one. The green light was set at a fixed power (9.2 mW), while the NIR source power varied between 0-15 mW. The top junction emission was collected again in order to establish the amount of coupling in each sample. Measurements in the absence of voltage (open-circuit conditions) and in the presence of voltage were carried out. The voltage applied on the device was selected to be in the range 0 - 2 V which is lower than the open-circuit of the cells which is around 3 V.

Three samples were examined (labelled A, B, C). The detailed structure of the three samples is reported in Table 4. The samples under investigation were InGaP/InGaAs/Ge lattice matched

TJs, grown in the n-on-p configuration on (001) 6° off towards the (110) direction Ge substrates [44]. The cells exhibit different window, emitter and base layer thicknesses in the top InGaP junction. The In content of the InGaP compound is very similar for all the samples and close to the lattice match value (49.5%) as measured by high resolution X-Ray Diffraction. The top layer in all the samples under investigation has a band-gap at 1.8 eV and therefore absorbs in the wavelength region between 300-690 nm. The doping has been changed only in the emitters of the top and middle cells, keeping all the other doping values in the remaining structure the same. Furthermore, the thicknesses of the middle junction emitter and base layers were identical for all the three samples. The emitters of the middle cells were deposited with 1% of Indium content. However, in the case of samples B and C, 10 % of aluminium was added in the emitter layer in order to get a quaternary material (AlInGaAs). This is indicated in Table 4 by adding (Al) in the middle emitter raw. Also, the spacer thickness in sample A is lower than that apparent in samples B and C. The middle layer absorbs in the wavelength region between 600-880 nm.

Table 4: Structure of the TJ devices under examination

Sample	A		B		C	
Structure	**Thickness (μm)**	**Doping**	**Thickness (μm)**	**Doping**	**Thickness (μm)**	**Doping**
	top cell (InGaP)					
window	0.025		0.02		0.02	
emitter	0.15	n_2	0.085	n_2	0.085	$n_2/2$
spacer	0		0.05		0.05	
base	0.8		0.84		1.48	
	Middle cell (InGaAs)					
window	0.03		0.03		0.03	
emitter	0.085	n_1	0.085(Al)	n_1	0.085(Al)	$n_1/2$
spacer	0.0038		0.03		0.03	
base	3		3		3	

The three samples have been characterized with a solar simulator under G173 D spectrum with a concentration of 500 suns. The electrical results are reported in Table 5.

Table 5: Electrical performances of the samples under evaluation.

Sample	A	B	C
I_{SC} (A)	5.23	6.70	5.48
V_{OC}(V)	2.97	2.94	2.97
FF	76.7	87.7	87.0
Efficiency (%)	23.8	34.5	28.3

Initially, the spectrum at the band-gap edge of the top InGaP junction was taken in the presence of fixed green light power for all samples under examination. The top junction emission in the presence of a green light source indicates the strength of radiative recombination as discussed above. Our previous investigations demonstrated that a higher radiative signal from the top junction was found to create a higher coupling current to the junction below in materials with identical structure [45]. Therefore the investigation of radiative recombination of the samples is essential. The emission spectrum for all the samples at a voltage bias of 1 V and fixed green light intensity of 9.2 mW is depicted in Figure 38.

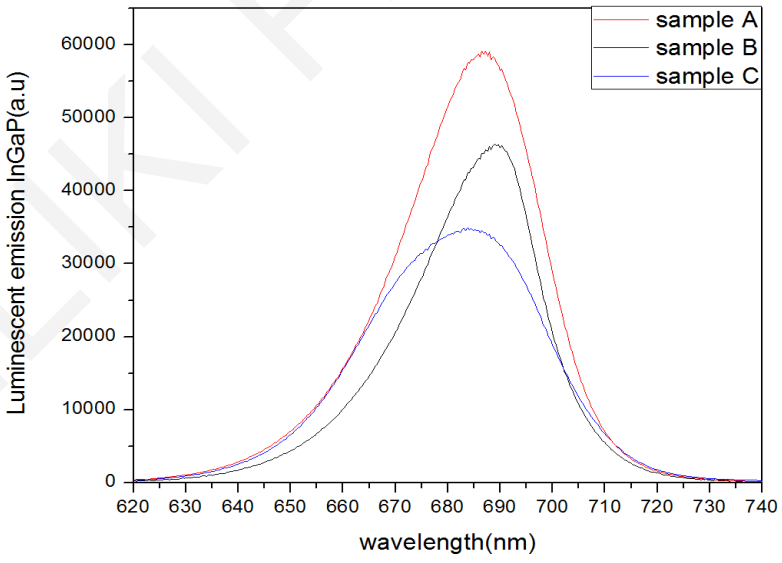

Figure 38: Luminescent emission spectrum of InGaP junction in all samples under investigation. The results were taken in the presence of a fixed green light intensity of 9.2 mW and at a voltage bias of 1 V.

The number of carriers in the top junction (which is determined by the thickness and doping of the layer) is expected to influence the luminescent emission since more carriers in the top junction contribute to a higher luminescent signal. Also, the defect density can lead to a significant reduction of the radiative emission and can have a major influence on the luminescent emission.

The highest radiative signal was obtained in sample A and it should be correlated with the thicker emitter, since at 520 nm the green laser intensity is reduced to 1/e after penetrating 0.18 μm, therefore most of the luminescence comes from the heavy doped n-type emitter. On the other hand, in samples B and C, the emitters are much thinner and a lot of carriers are generated and radiatively recombine in the low doped p-type base, giving rise to lower PL signals. Sample C presents a lower radiative signal in comparison to sample B due to the lower emitter doping level. Also the lower material quality of sample C (in comparison with sample B) seems to contribute to the lower radiative signal. The Full Width Half Maximum (FWHM) of a spectrum can be used for the material evaluation of the sample under study [46]. According to the FWHM values the highest material quality is sample B while the lowest one is sample A.

The emission from the middle junction in the presence of a green light source and voltage bias of 1 V was not detected since under those bias conditions the middle junction is reverse biased. In an attempt to examine the middle junction emission in the presence of a green light source, measurements with green light excitation have been repeated for a voltage bias of 2.5 V. Under these conditions the voltage excitation of the device is very high so the middle junction becomes forward biased and it is possible to obtain its luminescence. The middle junction peak intensity reduces in the presence of increasing green light power for the voltage value of 2.5 V (see Figure 39). This reduction is due to the increasing coupling effects from the top to the middle junction at higher green laser powers. As the green light power increases the photo-voltage of the top junction also increases (since the green light lies in the response region of the top junction). This consequently reduces the forward voltage of the middle junction since both junctions are connected in series and therefore the middle junction emission reduces. Similar observation was obtained recently although in that case reduction of the top junction EL emission was observed in the presence of increasing NIR light [31]. Both cases demonstrate the impact of coupling on luminescent emission from the samples.

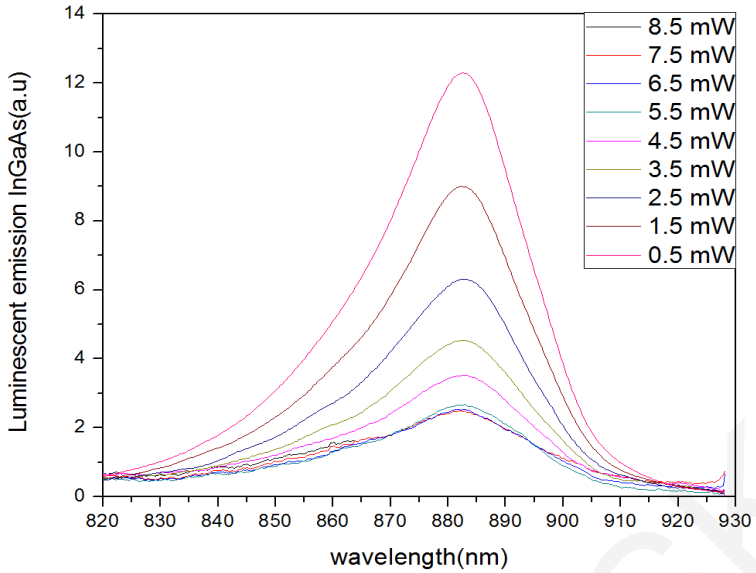

Figure 39: Luminescent emission from the middle InGaAs as a function of green light power and at a voltage bias of 2.5 V in sample A.

Subsequently, in order to study the coupling from the middle to the top junction, in the presence of a fixed green light power source, a NIR source of varying intensity was added and the luminescent signal from the band-edge of the top junction was acquired at each NIR irradiance value. The reduction of the top junction emission will indicate coupling effects and will demonstrate which material structure enhances coupling. The top junction emission from all the samples at a voltage bias of 1 V is depicted in Figure 40.

Comparing the top junction emission reduction with increasing NIR power in the samples in Figure 40, it can be obtained that the reduction of the top junction emission in sample A is significantly lower compared to the reduction obtained in the remaining samples. In order to compare the differences in top junction emission reduction which indicate the amount of coupling in the samples, in Figure 41 the luminescent emission quenching of the top junction is plotted in normalized units for different NIR power. In all the samples under examination, quenching of the integrated top junction emission is obtained by increasing the NIR laser intensity due to coupling effects from the middle to the top junction. The NIR light lies in the response region of the middle InGaAs junction and thus increases the photovoltage of that layer. Due to the series connection of the junctions the voltage increase of the middle junction causes reduction of the forward voltage of the top one and the emission of the top junction decreases.

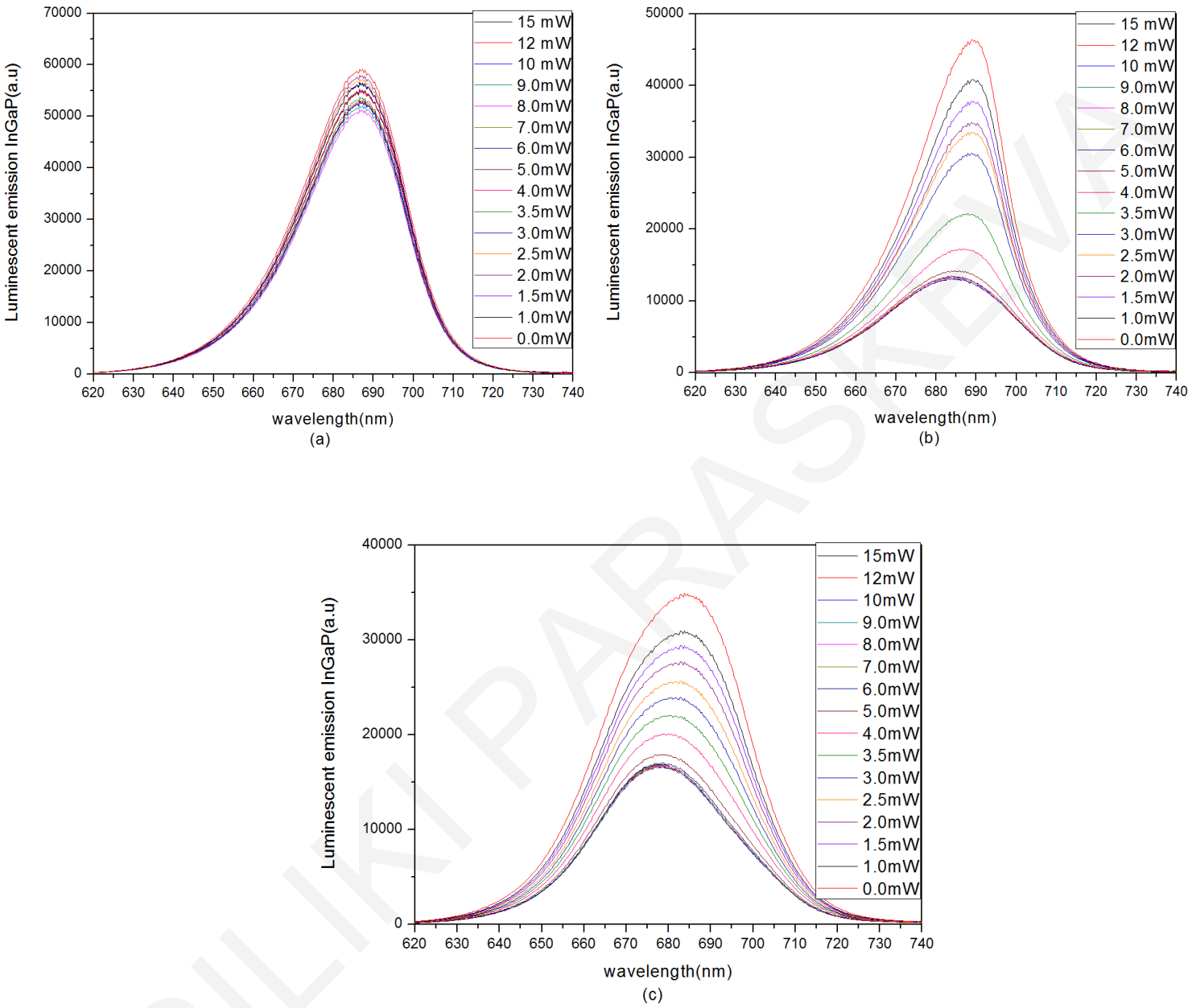

Figure 40: Luminescent emission from the InGaP junction as a function of NIR laser power, by keeping the green laser power constant (9.2 mW) at a voltage bias of 1 V for samples (a) A, (b) B and (c) C.

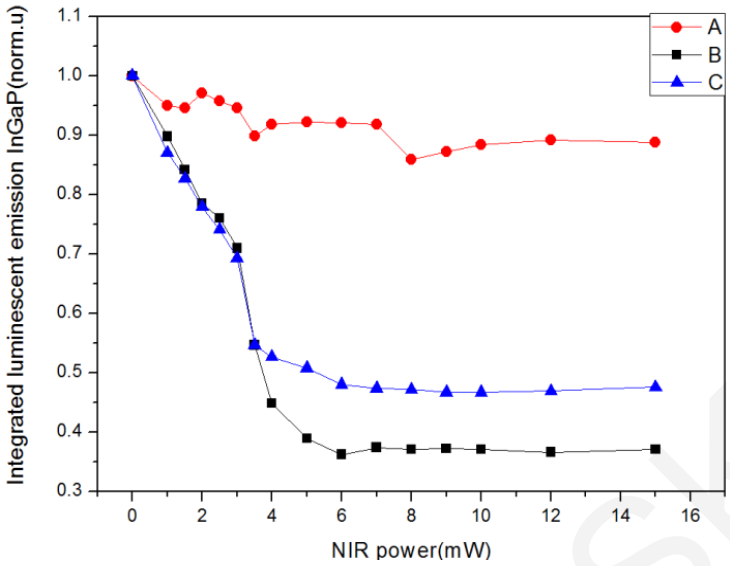

Figure 41: Luminescent emission quenching of the top junction in the presence of fixed green light power (9.2 mW) and varied NIR light power at a voltage bias of 1 V for all samples under investigation.

As depicted in Figure 41 the luminescent emission reduction of the top junction in sample A is the lowest indicating lower coupling at all NIR light bias intensities. A possible interpretation is related with the different emitter type and spacer thickness in the middle cell. The presence of a homojunction (n-InGaAs/p-InGaAs) and a thinner spacer in the middle junction of sample A generates a lower increase in the middle junction photovoltage with varying NIR light than that obtained in the n-AlInGaAs/p-InGaAs heterojunction of samples B and C resulting in lower voltage reduction on the top cell and consequently lower reduction in the top junction emission of sample A. The low material quality of sample A could also contribute to lower coupling effects in the device.

The luminescent emission reduction of the top junction in samples B and C is much higher compared to that obtained in sample A thus indicating that coupling is much higher in those samples due to the presence of the heterojunction and thicker spacer thickness as discussed above. The reduction of the top junction emission in samples B and C as a function of the NIR laser power is divided into two regions. In the first region (0-4 mW) no distinct difference in the top junction emission reduction in the two samples can be observed. However, at NIR intensities in the range 4-15 mW, the top junction emission reduction of sample B becomes significantly higher compared to that of sample C. Therefore, at NIR intensities above 4 mW

coupling effects are more pronounced in sample B. The difference in the top junction emission reduction and thus coupling effects at higher NIR intensities might be attributed to the different doping levels of the emitter in the middle InGaAs junction. Once the middle junction becomes forward biased, the presence of a higher doping in the emitter of the middle junction in sample B results in a higher amount of carriers involved and therefore in a higher increase of the middle junction photovoltage. This results in a higher reduction of the top junction forward bias and thus a larger drop in the top junction emission. The presence of higher doping in the emitter of the top junction in sample B also results in a larger reduction of the top junction forward bias and thus contributes to higher coupling effects in the sample. Furthermore, the higher material quality of sample B contributes to the higher coupling effects present in the sample. More radiative carriers are involved in the middle junction in that sample resulting in a higher increase of the photovoltage of the middle junction and thus larger drop of the forward bias of the top junction. This is confirmed by the diode equation, which clearly indicates that the photovoltage of a junction depends on the material quality of the junction [31].

The luminescent emission quenching of the top junction at different NIR light power was also examined at voltage biases of 0 V and 2 V. The results are similar with those depicted in Figure 41 and indicate no significant voltage dependence of the top junction emission reduction on the voltage bias. The independence of the top junction emission quenching from the voltage bias indicates that the operating voltage of the top junction remains the same.

One major characteristic of the emission curves of the samples shown in Figure 40 is the exponentially dropping edges. Examination of the slopes of the dropping edges at each light bias intensity showed that the slope of the energetically lower dropping edge changed more with increasing NIR light compared to the slope of the energetically higher dropping edge. This observation can be clearly seen in Figure 42 and it was obtained for all samples under investigation, indicating that the distribution of excited carriers inside the top junction changes significantly, owing to the reduction of the top junction operating voltage. Another important observation concerns the fact that the change of the energetically lower dropping edge is much higher in sample B compared to the one observed in samples A and C, demonstrating that the number of excited carriers near band-gap changes significantly in sample B with the change of NIR power. This might be related with coupling effects in the samples. The higher change in

carriers just below band-gap with NIR light power in sample B is a result of higher coupling effects between top and middle junction in accordance with Figure 41. On the other hand, sample A appears to have the lowest change in the slope of the energetically lower dropping edge demonstrating the smaller change in the number of carriers in that region due to lower coupling effects in the sample in good agreement with the experimental results of Figure 41.

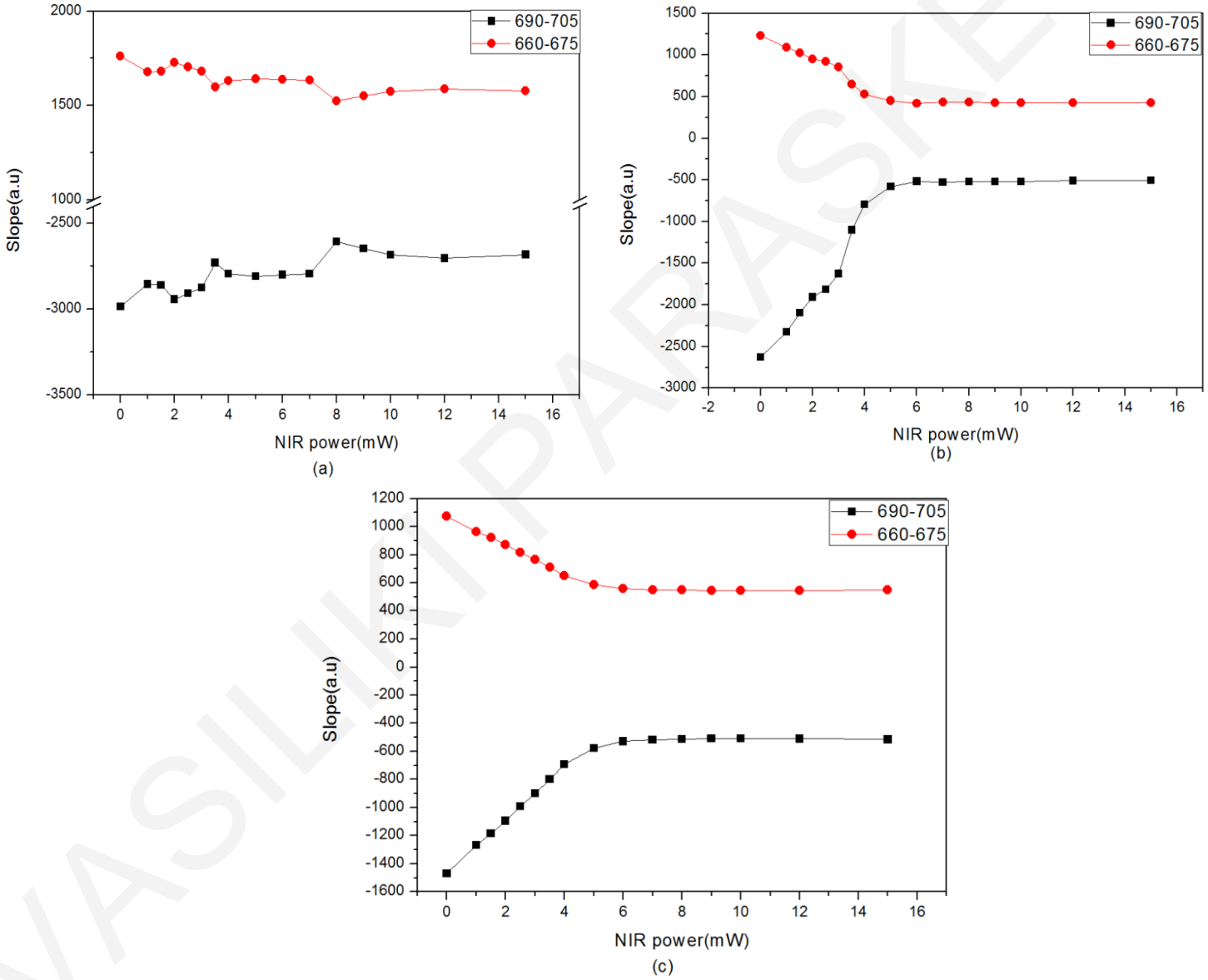

Figure 42: Slope of the lower and higher dropping edges of the PL emission of the top InGaP junction for samples (a) A (b) B and (c) C. The slopes correspond to a voltage bias of 1 V.

The luminescent emission of the middle junction was also investigated as a function of voltage bias. The InGaAs junction integrated PL intensity of sample A is presented in Figure 43. A linear behaviour is observed up to a NIR power of 4.5 mW, followed by an exponential behaviour at higher laser powers. This can be explained by the fact that the middle cell becomes forward biased when the NIR power reaches 4.5 mW. No significant voltage dependence of the integrated middle junction emission was detected in agreement with the top junction emission results.

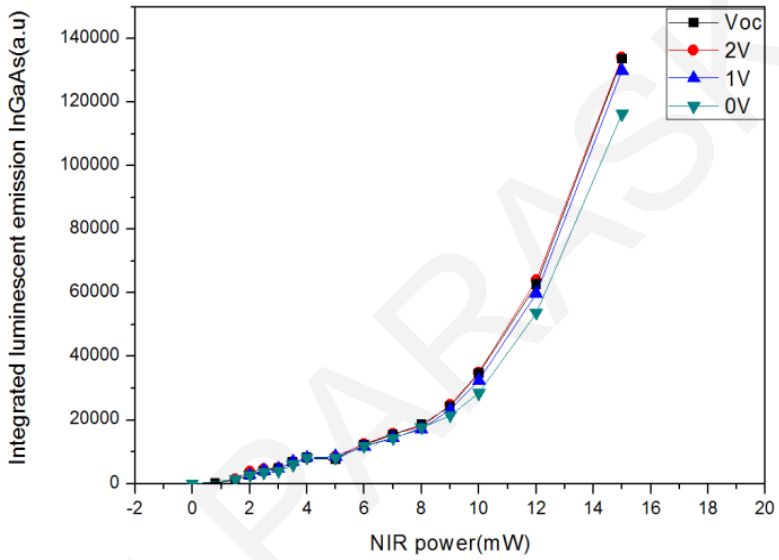

Figure 43: Integrated PL emission of the middle InGaAs junction in the presence of fixed green light power (9.2 mW) and variable NIR light power at different voltage bias in sample A.

Investigation of the PL emission of the cells and its correlation with the short-circuit current was also considered. In previous publications, spectrometric characterization was performed on the cells in the presence of varying total irradiance [29]. This method indicates the current matching point between the junctions through the change in the increase rate of the short-circuit current. In order to investigate the current matching by changing the NIR light intensity and by keeping the green light intensity fixed, the short-circuit current was collected in these conditions alongside the luminescent emission from both middle and top junctions. The results for samples B and C are depicted in Figure 44(a) and Figure 44(b) respectively. A clear change in the increase rate of the short-circuit current can be obtained in both samples indicating the current matching point of the junctions. The change in the increase rate of short-circuit current

coincides with the change in the reduction rate of the luminescent emission of the top junction and the change in the increase rate of the luminescent emission of the middle junction and it is in good agreement with recently published results [47], [48]. The transition point of the short-circuit current and the luminescent emission of the top and the middle junctions in both samples is apparent at NIR intensities around 4.5 mW. At NIR intensities lower than 4.5 mW the luminescent emission of the top junction drastically reduces while the emission from the middle junction increases linearly along with the short-circuit current. However, at NIR intensities above 4.5 mW the top junction emission remains constant while the middle junction emission increases significantly. At the same time the short-circuit current remains constant or increases slightly. These observations provide evidence that at NIR intensities below 4.5 mW the tandem device could be middle junction limited while above that value could be top junction limited. The transition from middle to top current limited junction can explain the observations in emission and current. The observations hold if we assume that the bottom junction is shunted.

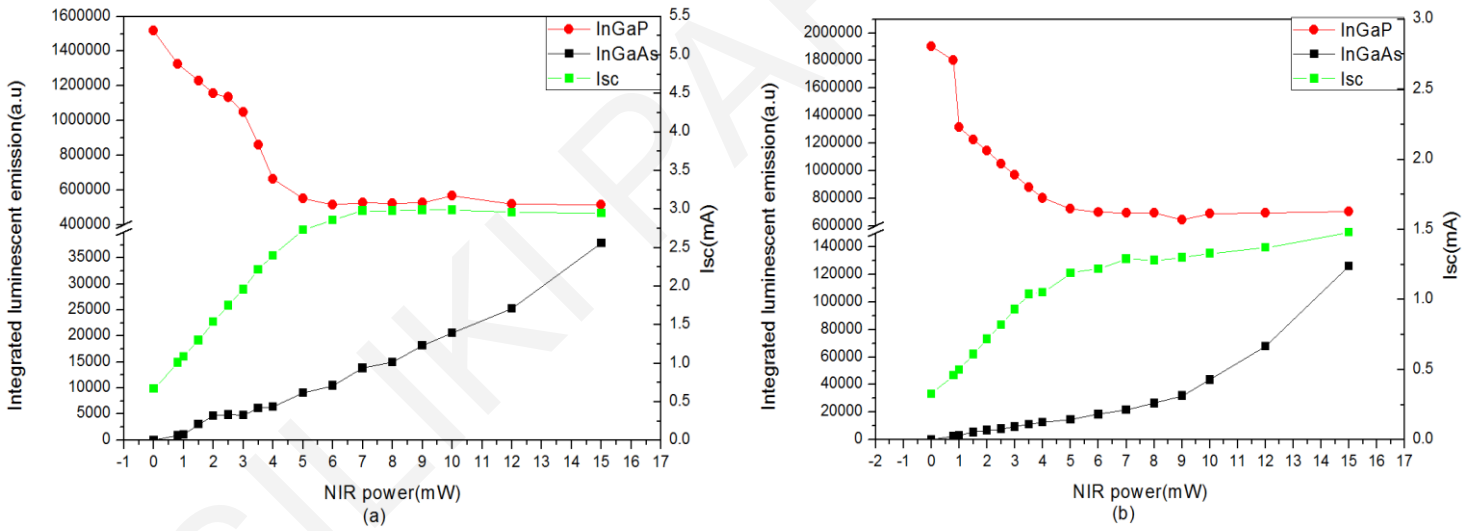

Figure 44: Integrated PL of the top InGaP and middle InGaAs junction alongside the short-circuit current of the tandem InGaP/InGaAs/Ge in the presence of varying NIR intensity in the samples (a) B and (b) C.

Double wavelength PL measurements on different structure devices have demonstrated the impact of material design on coupling effects. Solar cells with higher doping levels in the emitter of the top and middle junctions were found to enhance coupling from the middle to the top junction. Furthermore, the presence of heterojunction in combination with thicker spacer

thickness was found to promote significantly coupling effects in a tandem device. Samples with n-AlInGaAs/p-InGaAs heterojunction in the middle junction and thicker spacer thickness demonstrated higher reduction of the top junction luminescence in the presence of NIR light due to enhanced coupling effects.

Conclusions

In summary, detailed investigation of the effect of shunt, material structure and temperature on coupling has been performed in this section giving an insight into how those parameters influence the coupling current directed towards bottom junctions. High quality material was found to promote coupling effects while temperature was found to reduce them. The presence of heterojunction in combination with thicker spacer thickness was found to affect significantly coupling effects as well. Furthermore, a physical model of the defects in a solar cell was build and used to simulate the emission from different material quality samples. The results are in agreement with the experimental ones thus validating the physical model.

Chapter 4

Luminescent emission of multi-junction solar cells

4.1 Introduction

Most of III-V materials used in multi-junction devices are direct band-gap semiconductors where radiative recombination is the dominant carrier recombination mechanism. Thus radiative losses in such devices are significant and are expected to reduce the device performance. Furthermore, radiative losses give an indication of the presence of coupling in a tandem device and therefore their examination will provide useful insight into the presence of coupling effects. As a result in order to study radiative losses under high intensity conditions, combined EL and PL measurements under a solar simulator have been carried out. Such measurements have not been achieved to date and are required. This is deemed necessary in order to improve our understanding on the luminescent emission under actual operating conditions outdoors and to provide cell designers with appropriate information which can be used to optimize the quality and efficiency of triple-junction devices. Luminescent emission under a sun simulator at different voltage bias, temperatures and sun concentrations has been studied and is described in detail here. Furthermore, in order to compare the indoor and outdoor results luminescent emission from the multi-junction device was captured under real outdoor operating conditions.

4.2 State of the art

EL and PL spectroscopy allows a comprehensive study of the optical transitions in solar cells in a wide range of wavelengths and provides a better understanding of the fundamental optical

properties of the materials. EL and PL have been used in several investigations for fast spatially resolved characterization of the electrical properties of crystalline Silicon solar cells [49], [50]. Both methods also allow a quantitative evaluation of the diode quality for state-of-the-art devices [51]. In addition to spatially-resolved EL, spectrally-resolved EL of solar cells has also been investigated [52].

EL and PL methods have been applied to multi-junction devices as well. The correlation of the spectrally-resolved EL with the current/voltage curves of each individual junction in a multi-junction device has been discussed by Kirchartz in [53]: EL data are combined with external quantum efficiency measurements in order to deduce the current/voltage curves and the ideality factor of all individual junctions in a multi-junction device. Similar analysis for the deduction of individual junction I-V characteristics has been carried out in [54]. EL investigation of a multi-junction device has also been considered by Hoheisel [55] who determined the open-circuit voltage degradation of each junction of the tandem through EL spectroscopy and in the presence of photon irradiation.

Radiative losses of multi-junction InGaP/InGaAs/Ge have not been investigated by means of combined EL and PL. Particularly, luminescent emission of the cells under a high intensity solar simulator, which resembles the outdoor operation of the cells, has not been achieved to date. Such measurements would indicate to what extent radiative losses are important for the operation of the device at different voltage, temperature and sun concentration. Furthermore, outdoor results of luminescent emission in the field are of major importance and will provide valuable comparison with the indoor results. Also, EL and PL spectroscopy are required for achieving better understanding of the fundamental optical properties of such cells. Indoor testing at different excitation power and temperature would give valuable information about the material quality and recombination processes involved in the devices under each condition. These issues are considered in this chapter.

4.3 Luminescent emission of multi-junction PV cells under high intensity irradiation

Initially, luminescent emission of multi-junction PV cells has been examined at various operating conditions. Luminescent emission from a multi-junction device can be obtained when

the cell is either excited electrically (EL) or optically (PL). The luminescent emission essentially represents the carriers that are not contributing to photocurrent and are extracted from the device as photons. Thus the amount of luminescent emission represents the amount of carriers "wasted" as radiative losses in the material. The higher the emission, the higher the radiative losses and the higher the amount of carriers being lost. In outdoor operating conditions radiative losses should be kept to a minimum in order to keep the cell's performance to the highest possible value. In order to investigate the presence of luminescent emission of InGaP/InGaAs/Ge triple-junction devices combined EL and PL measurements were conducted indoors. PL was achieved with the use of a high intensity solar simulator while EL excitation was achieved with a voltage source. The measurements simulate the operation of the device in real outdoor operating conditions. Luminescent emission was examined at different sun concentrations and voltage biases. Specifically, at each concentration level measurements at different voltage bias were performed.

The high intensity pulsed solar simulator used for the measurements is installed at the Joint Research Centre (JRC). The pulsed solar simulator beam can be adjusted to provide concentrations from 200 to 2000 suns intensity. Its light source is a Xenon lamp that delivers 5 ms pulses of light with a spatial non-uniformity of ± 2% over an area of 4 x 4 cm^2. An operational amplifier was used for the application of voltage bias to the device and for the appropriate current limitation. A Silicon (Si) spectroradiometer unit that covers the visible and near infrared region (300-1000 nm) with a spectral resolution of 0.5 nm was utilized for the detection of the emission of the device during flashing. The Si spectroradiometer can typically detect the emission of the top two junctions of a triple-junction device. The signal from the bottom (typically Ge) junction cannot be observed in the PL spectrum since it is outside the sensitivity region of this spectroradiometer. Automated triggering of the spectroradiometer provided the collection of the PL signal from the device during flashing whilst a fiber-optic cable collected the emission from the cell. The fiber-optic was located in front of the cell shading part of the cell from the simulator flash. At each concentration level, the short-circuit current and the open-circuit voltage were measured using a Yokagawa scopecorder. The short-circuit current was measured over a calibrated load resistor of 0.05 Ω. The 1-sun I-V curves of the device were carried out under a 1-sun solar simulator at the JRC. The short-circuit current

at 1-sun was used to calculate the irradiance concentration level applied to the device each time. Current-voltage (I-V) characteristics were also captured at each concentration level under examination in order to indicate the maximum power point in each case. I-V curves were taken by a custom made I-V scan which is part of the sun-simulator system. A Keithely 2430 was used for four-point measurements. The schematic of the set-up is shown in Figure 45.

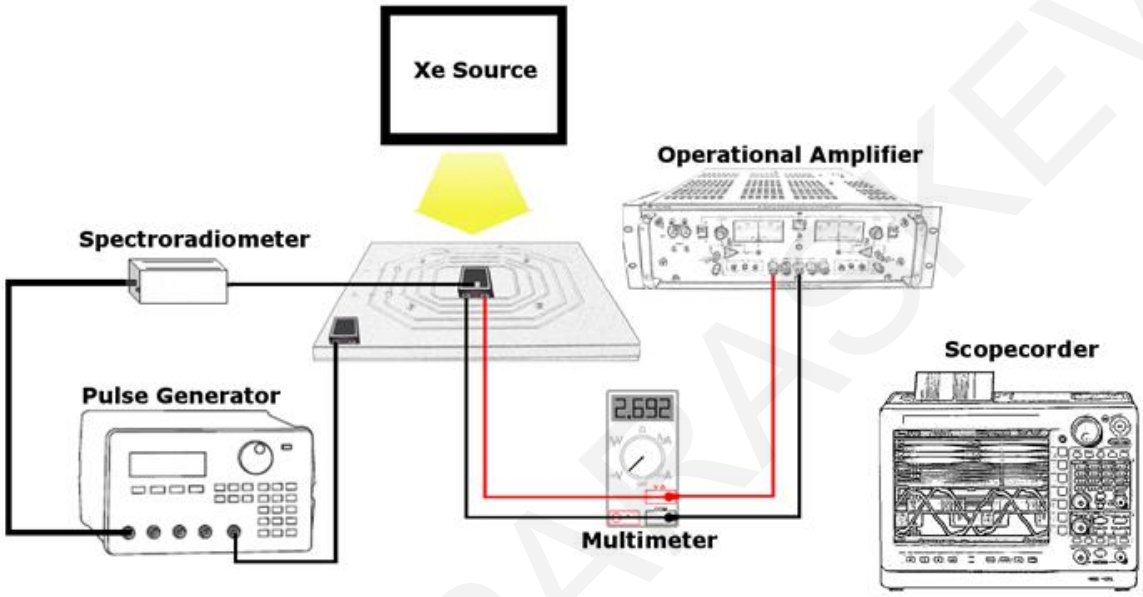

Figure 45: Schematic of the sun simulator set-up

The solar cells used are triple junctions InGaP/InGaAs/Ge manufactured by Azur and with dimensions of 30 mm^2. The band structure of the triple-junction device showing the possible transitions of carriers in the presence of light excitation of 3.1 eV is depicted in Figure 46. That energy excites all the carriers in the structure as in the case of a sun simulator. Procedure 1 presents the direct excitation of the top junction carriers, procedure 2 presents the transition of carriers from the top to the middle junction, procedure 3 presents the direct excitation of the middle junction carriers, procedure 4 presents the carriers transition from the middle to the bottom junction and finally transition 5 presents the direct excitation of the bottom junction carriers.

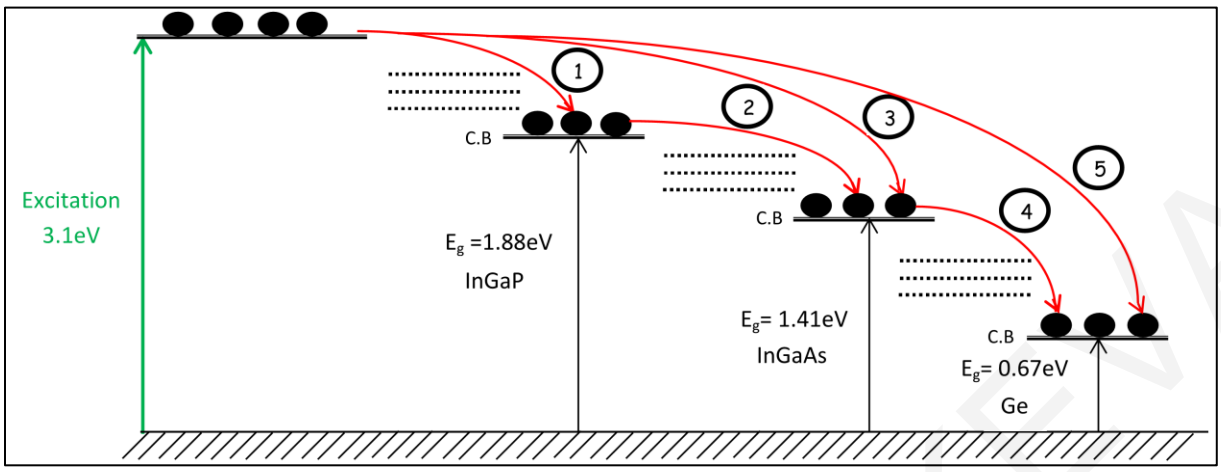

Figure 46: Schematic energy band diagram of the InGaP/InGaAs/Ge solar cell depicting the various relaxation mechanisms and paths following excitation by 3.1eV photons (400nm).

The detection of the signal from the device during the measurements is a non-trivial task due to the high reflection of the Xenon lamp spectrum from the surface of the cell which obscures the actual emitted signal. For that purpose and in order to have a clear indication of the luminescent emission from the cell, the short-circuit current emission was initially captured. Due to the absence of voltage at short-circuit conditions, the emitted signal is very low and differs from the emitted signal taken in the presence of voltage. For that reason the short-circuit spectrum taken from the device was set as the background signal and then the spectrum from the device was taken in the presence of voltage.

4.3.1 Impact of voltage bias

The luminescent emission from the device was investigated at different voltage biases and at a constant temperature in order to establish the impact of voltage bias. A broad range of concentration levels was used, between 200 and 1000 suns. Before performing the optical measurements, the electrical parameters of the device were measured to determine the maximum power point of the device in each case and therefore the voltage region at which the cell should be investigated optically. The electrical characteristics of the device at nominal concentrations of the sun simulator of 400 suns and 1000 suns are given in 6. The temperature of the device was set to 20° C. After performing these measurements, the voltage bias applied to the device was varied between 2.6-2.9 V to specifically include the maximum power point voltage at each concentration level within the range. Voltage dependent emission spectra were

then recorded from the triple-junction cell under test at various voltages at sun concentration between 200 and 1000 suns and at a temperature of 20°C. The results are depicted in Figure 47.

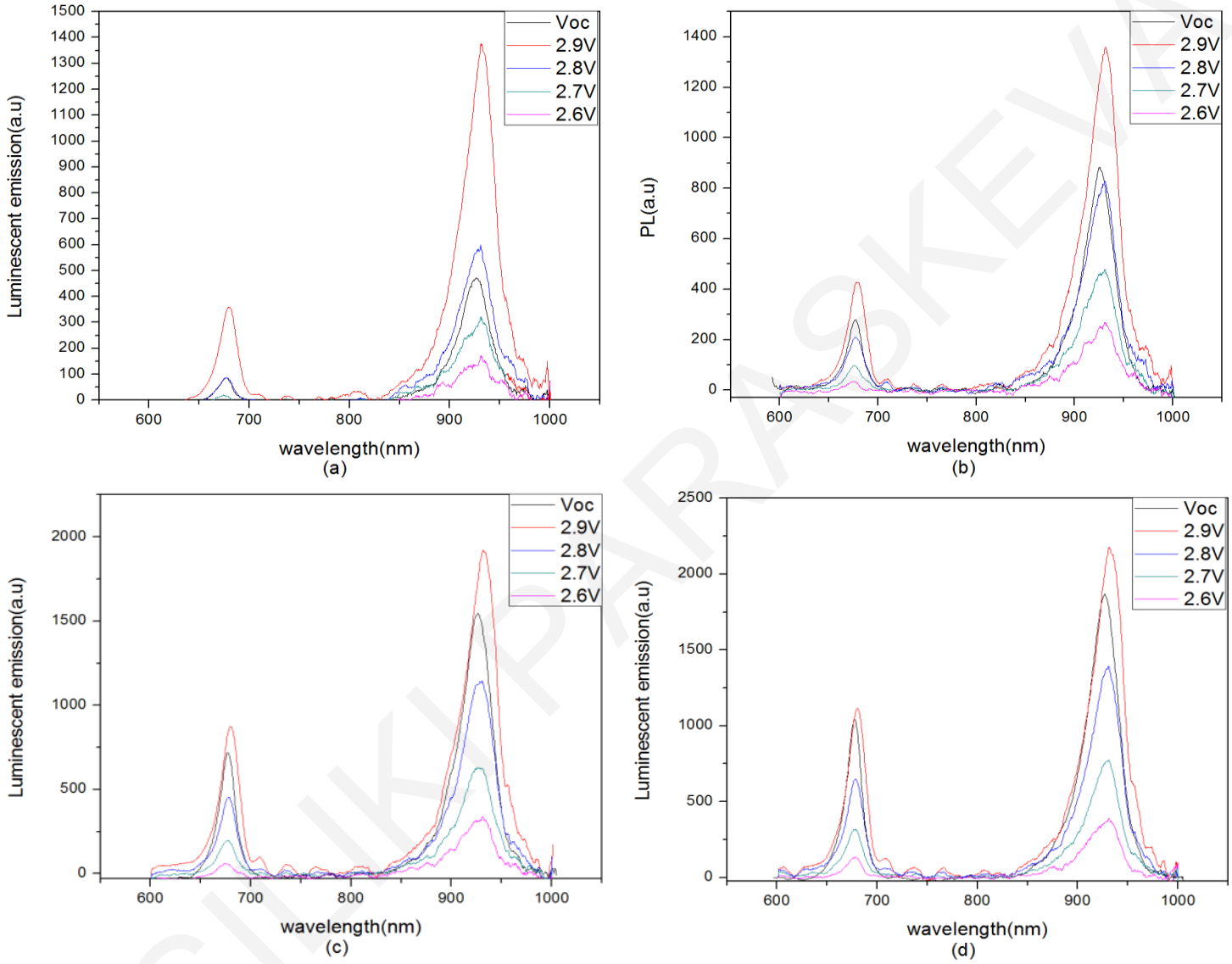

Figure 47: Luminescent emission from the device at different voltage biases at a temperature of 20°C. The spectrum was taken at (a) 200, (b) 400 (c) 800 and (d) 1000 suns.

Table 6: Electrical parameters of the device under examination at different nominal concentration levels. The temperature of the sample was set to 20°C.

Nominal Concentration Level (suns)	V_{oc} (V)	I_{sc} (A)	P_{MPP} (W)	FF (%)	V_{MPP} (V)	I_{mpp} (A)
400	3.06	1.89	4.95	85.20	2.69	1.83
1000	3.15	5.12	13.51	82.40	2.77	4.87

Two emission peaks are present at the band-edges of the two top junctions at 1.33 eV and 1.82 eV at all voltage biases and for both concentration levels under investigation. During light excitation of the cell, radiative recombination of carriers creates photons that can be either emitted from the surface or directed towards the bottom junctions where they can be absorbed. The emission signals observed correspond to the portion of photons that finally escape from the cell. According to previous work a small number of photons is expected to be emitted from the surface since the escape cone of photons at the front of the cell is relatively small. Thus, the vast majority of photons are actually emitted and absorbed into the lower junctions causing coupling effects [16]. The large amount of photons emitted from the band-gap edges of the top and middle junctions in our measurements give an indication of the possibility of the presence of coupling effects in the device. Specifically strong radiative recombination at the band-gap edge of the top InGaP might lead to absorption of photons from the middle InGaAs junction and coupling effects. Similarly, strong emission from the InGaAs junction may lead to absorption of photons in the bottom Ge junction. The observation of a strong radiative signal in Figure 47 from both junctions at maximum power point voltage for both concentration levels gives evidence that coupling effects may occur during outdoor operation of the device in these conditions. Furthermore, higher radiative emission is observed at higher voltages as indicated in Figure 47 since the voltage bias increases the amount of recombination in the device.

As depicted in Figure 47, the radiative emission created by the middle InGaAs junction is considerably higher compared to the amount of luminescent emission produced by the InGaP top junction. The difference in luminescent signals is believed to be attributed to the thickness of the InGaAs middle junction. This is in agreement with the EL emission of the device which

shows that the emission signal from the middle junction is higher than the signal emitted by the top one [56]. Here it should be noted that the radiative signal at 1.33 eV should be a superposition of the actual luminescent emission from the middle junction and the radiative recombination of carriers of the top junction. Specifically, the photons emitted from the top junction are directed towards the middle one via optical interactions and coupling effects. The excited carriers produced by the injected photons are relaxed to ground states and finally to the band-gap edge contributing to the radiative emission at 1.33 eV.

Furthermore, the radiative emission at different voltages shows that the application of higher voltage biases causes shifting of the peak wavelength. This redshift is tentatively attributed to heating of the sample leading to band-gap narrowing effects. Even if the sample temperature was set to 20°C, the lattice temperature rises due to excess carrier density apparent in the device as a result of high biases. The redshift is more pronounced in the case of applied voltage value of 2.9 V where the forward bias is higher. At open-circuit conditions redshift of the spectrum was not observed indicating that the temperature rise is very low in those conditions may be due to the absence of current in the device. At sun concentrations of 400 in Figure 47(b) the band-gap shrinkage of the top junction in the investigated voltage range was measured to be 10.8 meV while the reduction of the band-gap for the middle was 1.2 meV. Similar reduction of the band-gap was observed at even lower sun concentrator levels (200). The band-gap shrinkage at a concentration level of 1000 suns was found to be 4.8 meV for the top and 1 meV for the middle junction. The peak wavelengths against voltage bias for concentration levels of 400 and 1000 are depicted in Figure 48. The top junction appears to have a larger redshift at both concentration levels indicating the higher sensitivity of that junction to the applied voltage and thus to the temperature. Higher sensitivity of the top junction with temperature is a material dependent property and is attributed to the higher temperature coefficient of the InGaP material. This is confirmed by the temperature measurements presented in the next section.

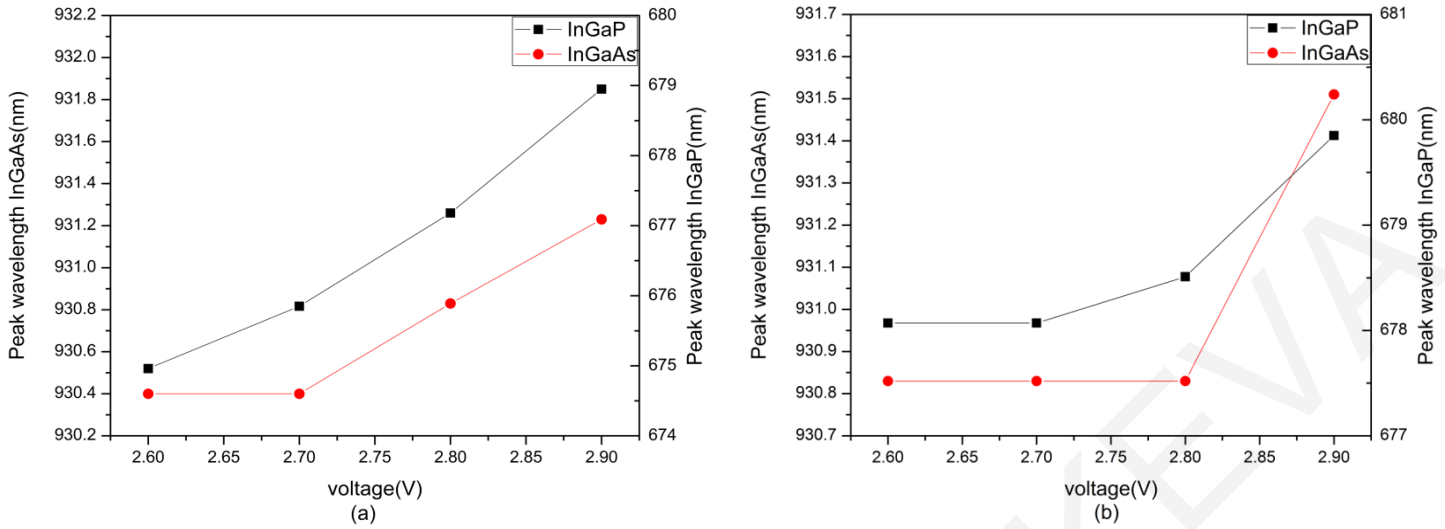

Figure 48: Peak wavelengths against voltage bias at a temperature of 20°C. The dependence of the peak wavelengths with voltage was investigated at (a) 400 and (b) 1000 suns. Redshift of the peaks is more pronounced in the top InGaP junction.

Figure 47 also shows that the emission taken at open-circuit conditions is higher than the emission taken at maximum power point voltage. Under open-circuit conditions, the emission is expected to be higher compared to the one taken at maximum power point voltage since in the absence of current, all the energy of the device is dissipated as emission [42]. One important observation that arises from Figure 47 is that the emission taken at open-circuit conditions is lower compared to the radiative signal emitted from the device in the presence of voltage bias of 2.9 V. So for the conditions investigated here even if the open-circuit voltage value is above 2.9 V the luminescent intensity emitted at open-circuit conditions is not related linearly with the luminescence arising when we apply voltage to the device. The result shows that with voltage bias application of 2.9 V, the carriers created in the device are higher in number compared to the carriers created due to light only (open-circuit conditions). Therefore, although a lower radiative recombination is expected in the presence of voltage (2.9 V) due to current generation, the high number of excited carriers results in significant luminescent emission. Consequently, the emission seems to depend non-monotonically on the bias. However, in the presence of voltage a proportional relation between luminescent intensity and voltage exists. The integrated luminescent signal was found to increase with increasing applied voltage since the presence of voltage moves the operating point of the device towards the forward bias region where the recombination rate increases as mentioned before. The integrated

luminescent emissions of the InGaP and InGaAs against voltage at low (400) and high (1000) sun concentrations are shown in Figure 49.

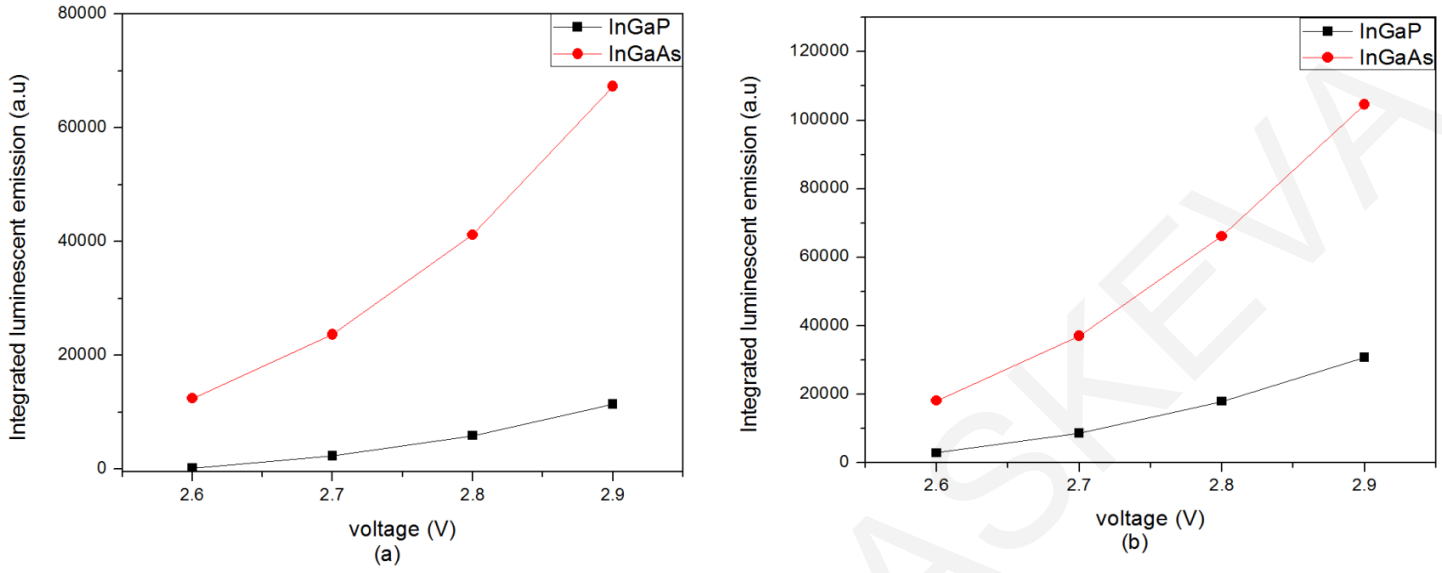

Figure 49: Integrated luminescent emission against voltage bias for both top InGaP and InGaAs junction at sun concentrations of (a) 400 and (b) 1000. The temperature of the sample was set to 20°C.

The dependence of the integrated emission against voltage is exponential for both junctions and concentrations under investigation. Since the emission is linearly related to the recombination current [57] and the recombination current has an exponential dependence with voltage according to the diode equation [33] the emission signal is expected to be exponentially related to the applied voltage. Figure 49 also shows that the increase of the emission with voltage is more pronounced in the top junction at lower concentration levels (400 suns). The higher sensitivity of the top junction to voltage could be attributed to the higher sensitivity of that junction to temperature as discussed above. Higher voltage bias applied on the device leads to increased lattice temperature and thus heating of the sample leading to band-gap reduction. Band-gap shrinkage causes a decrease of the open-circuit voltage of a junction and an increase of the photocurrent [58]. The photocurrent becomes higher due to increased absorption from the lower energy states close to the band-gap edge. Reduction of the open-circuit voltage also occurs due to heating in both junctions and thus the operating voltage comes closer to open-circuit conditions, enhancing the recombination within the device. Since band-gap narrowing is higher in the top junction as indicated by the higher redshift of the PL peak, photocurrent and optical absorption as a function of voltage increase more compared to the middle junction

leading to a higher increase in radiative emission. Furthermore, open-circuit reduction is more pronounced in the top junction and thus the operating voltage comes closer to open-circuit voltage resulting also in higher recombination in the top junction. Another factor that may explain the higher sensitivity of the top junction to voltage could be the dependence of the potential of each junction on the applied voltage. Higher voltage biasing of the device could affect the top junction bias to a greater degree (shifting it closer to open-circuit voltage) than the middle junction and thus increased recombination is observed. Overall, a combination of the above effects may also take place resulting to a higher sensitivity of the top junction to voltage. The above effects are more pronounced at lower concentrations.

In the high voltage region (2.9 V) multiple small peaks are apparent at wavelengths between 700-832 nm. Their presence in the high voltage regime indicates that their existence is related to voltage bias. The exact wavelength positions of the peaks at different concentration levels and at a voltage bias of 2.9 V are given in Table 7.

Table 7: Wavelength position of the peaks apparent in the vicinity of the middle junction at different nominal concentration levels. The voltage bias applied on the device was 2.9 V.

Nominal Concentration Level (suns)	Wavelength (nm)	Wavelength (nm)	Wavelength (nm)	Wavelength(nm)
200	710.0	738.0	768.0	-
400	708.7	737.0	765.0	-
800	708.0	736.5	766.0	809.2
1000	707.8	736.5	765.8	806.2

The small peaks are tentatively attributed to defect luminescence in the top junction. They are apparent at the high voltage regime in all the concentration levels under examination and become more pronounced at high light biases where the junctions become even more forward bias. The forward bias in those conditions is so strong that has the potential to excite mid-gap states in the junctions. The wavelength of the peaks was found to 'blueshift' at higher irradiance concentrations due to band filling effects. The sensitivity of the spectroradiometer used was limited at 1000 nm and therefore the presence of similar peaks in the wavelength region of the middle InGaAs junction could not be observed.

4.3.2 Impact of concentration

The luminescent emission at the maximum power point was measured at different concentration levels in order to study the effect of concentration upon radiative emission from the device. Results are depicted in Figure 50 (a). The integrated emission as a function of concentration for both junctions (InGaP and InGaAs) is shown in Figure 50(b).

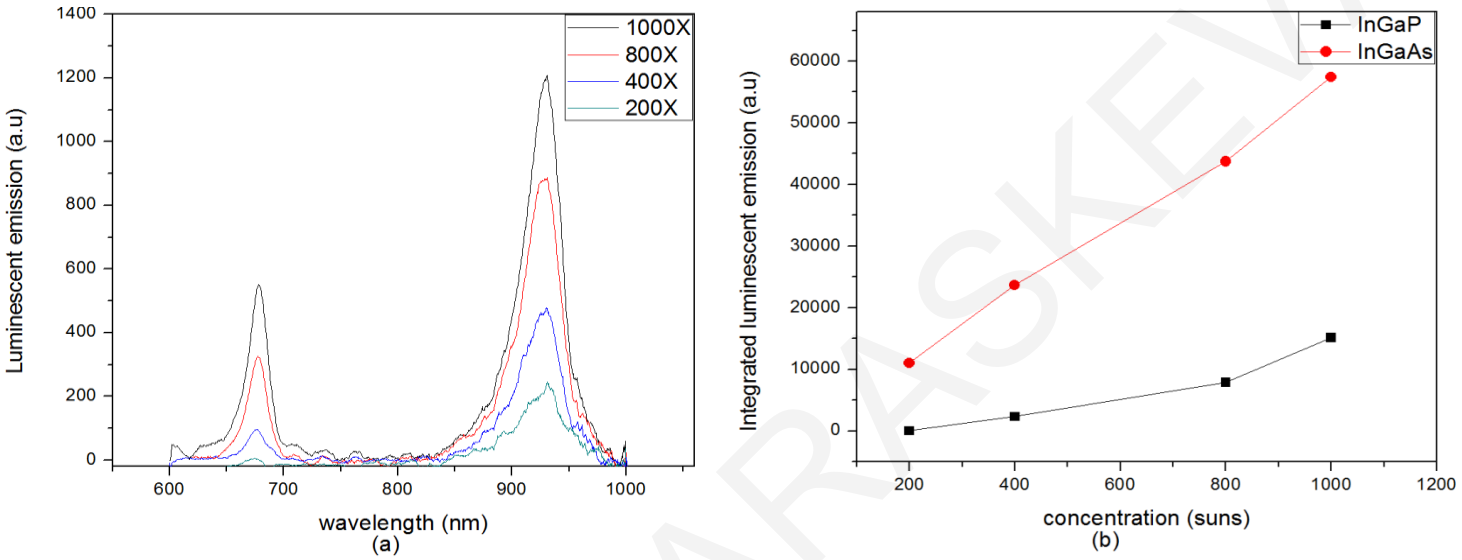

Figure 50: (a) Luminescent emission of the InGaP/InGaAs/Ge device at maximum power point conditions and at sun concentration between 200-1000. The temperature of the device was set to 20°C. (b) Integrated PL of the top InGaP and middle InGaAs junction against concentration at the same voltage and temperature conditions.

A linear relationship of the integrated luminescent emission against concentration is apparent for the InGaAs junction in the investigated concentration range. The measurements were conducted under high carrier injection conditions where radiative recombination is the dominant mechanism [59]. The linear relationship is not apparent for the top InGaP junction probably due to the existence of multiple peaks at the low energy band tail of the junction described above which overestimates the integrated emission at 1000 suns. The increasing rate of the integrated emission of the middle junction against concentration is much higher than the rate observed for the top junction since a higher number of carriers is excited in that junction due to the larger thickness.

Redshift of the PL peak was obtained with increasing sun concentration indicating an increase of the sample temperature due to higher injection levels. The observed redshift fluctuates between 1-6 meV depending on the applied temperature with the higher shift present at lower

temperatures (20°C) and at the top junction. Redshift of the middle junction is very small and almost negligible. The observed redshift is in agreement with recent published results and may be attributed to enhanced carrier-carrier and carrier-lattice collisions [60], [61].

The luminescent emission from open-circuit conditions was also examined at different sun concentrations. The results can be obtained in Figure 51.

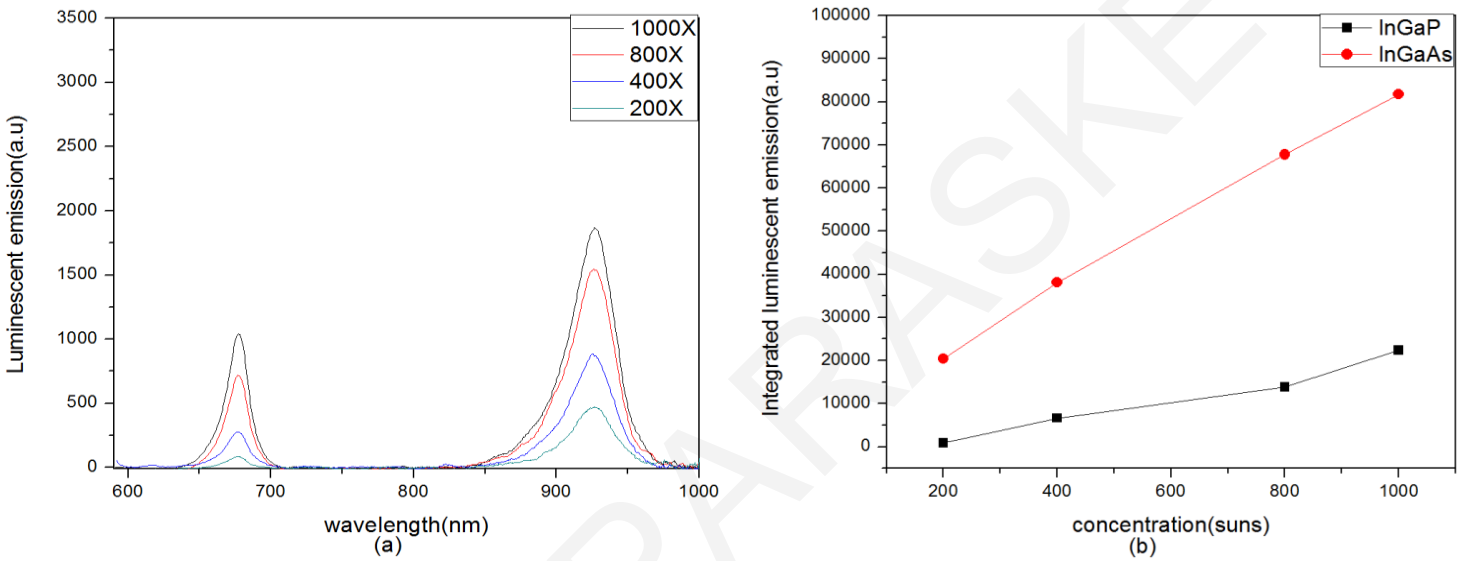

Figure 51: (a) Luminescent emission of the InGaP/InGaAs/Ge device at open-circuit conditions and at sun concentration between 200-1000. The temperature of the device was set to 20°C. (b) Integrated PL of the top InGaP and middle InGaAs junction against concentration at the same voltage and temperature conditions.

A linear relationship of the integrated luminescent emission against concentration is also apparent for both junctions in the investigated concentration range at open-circuit conditions. One interesting aspect is the absence of multiple small peaks at wavelengths between 700-832 nm a fact that indicates that the presence of those peaks is correlated with high excitation levels and voltages. Redshift of the top junction in those conditions was found to be around 1.2 meV while the middle junction didn't exhibit any redshift.

4.3.3 Impact of temperature

To examine the impact of the temperature on the radiative emission, the emission spectrum from the device was captured at various temperatures. The temperature control of the sample was achieved with a Peltier element with measurement uncertainty of 4%. Initially the electrical characteristics were measured at temperatures of 40°C and 60°C and at nominal concentration of 1000 suns as depicted in Table 8. The maximum power point voltage at these temperatures is lower compared to that at lower temperatures (20°C) investigated earlier. In an attempt to indicate differences between luminescent emissions at high and low temperatures, the emission at a specific concentration (1000 suns) and at maximum power point was plotted for three different temperatures 20°C, 40°C, 60°C (Figure 52a). Furthermore for comparison purposes, the radiative emission at open-circuit voltage conditions was also plotted at different temperature levels (Figure 52b). Integrated luminescent emission against temperature is plotted in Figure 52(c) and Figure 52(d) respectively in order to demonstrate the trend of the emission with temperature at maximum power point voltage and open-circuit conditions.

Table 8: Electrical parameters of the device under examination at different temperatures. The nominal concentration level is 1000 suns.

Temperature (°C)	**V_{oc} (V)**	**I_{sc} (A)**	**P_{MPP} (W)**	**FF (%)**	**V_{MPP} (V)**	**I_{mpp} (A)**
40	3.08	5.16	12.93	80.70	2.65	4.89
60	3.01	5.24	12.44	78.90	2.52	4.95

It is observed that luminescent emission from the device is still apparent at 40°C and 60°C indicating that significant radiative recombination takes place in the device and therefore coupling effects may occur at even higher temperatures. Higher temperatures are expected to significantly reduce radiative recombination from the junctions since non-radiative paths become dominant at these conditions [56], [62]. Due to the reduction of the radiative recombination the coupling current directed towards the bottom junctions is likely to be affected significantly.

A linear redshift of the luminescent peaks with temperature is apparent during measurements at open- circuit conditions and in the presence of voltage. The shift of the emission is attributed to heating resulting in band-gap shrinkage effects of the junctions. A linear decrease of band-gap energy with increasing temperature is a typical behaviour of semiconductors for temperatures above roughly 100 K [61], [63]. The band-gap shrinkage of the InGaP due to heating at open-circuit conditions (Figure 53) is 21.4 meV while the corresponding one for the middle junction is 19.6 meV. The corresponding band-gap narrowing per degree celsius for each junction is $5.3x10^{-4}$eV/°C and $4.9x10^{-4}$eV/°C which are in good agreement with previous measurements [20]. As temperature increases, the absorption band energy of the top junction shifts more than that of the middle causing a rise in the current density ratio of top to middle (J_T/J_M) with temperature. The shift to higher J_T/J_M with temperature is advantageous given that higher J_T/J_M is generally more difficult to achieve. Integrated luminescent emission against temperature (Figure 52(c) and Figure 52(d)) demonstrates that the radiative emission of the top junction reduces more than the emission of the middle in both maximum power point and open-circuit conditions as a function of temperature. This indicates the higher sensitivity of the top junction emission with temperature. It is well known that the decrease of the energy gap of the device due to temperature effects leads to reduction of the open-circuit voltage [58]. Since the band-gap reduction of the top junction is higher, the open-circuit voltage drop is larger in that junction. Therefore the luminescent emission of the top InGaP junction at open-circuit conditions will exhibit a higher intensity drop compared to the middle InGaAs in agreement with the observed results. This holds for the luminescence at maximum power point voltage conditions.

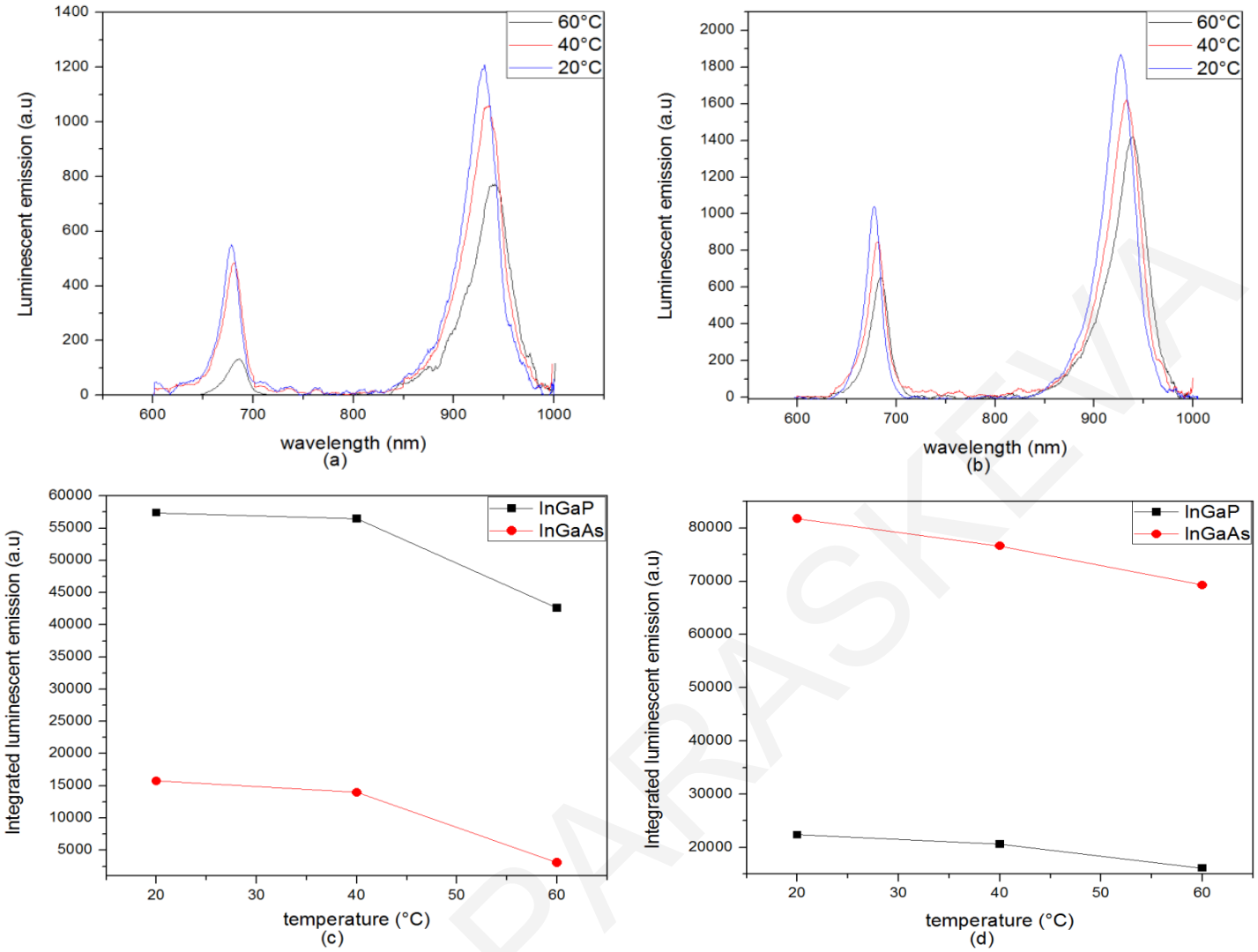

Figure 52: Luminescent emissions of the InGaP/InGaAs/Ge device at a concentration of 1000 suns for three different temperatures at (a) maximum power point and (b) at open-circuit conditions.Integrated PL against temperature at maximum power point and open-circuit conditions are depicted in Figure 52(c) and Figure 52(d) respectively.

The corresponding band-gap shrinkage at maximum power point conditions in both junctions is also shown in Figure 53. Redshift of about 7.9 meV is apparent in the middle junction while redshift of 21.4 meV is apparent in the top junction. The band-gap shrinkage of the middle junction seems to be lower in maximum power point conditions.

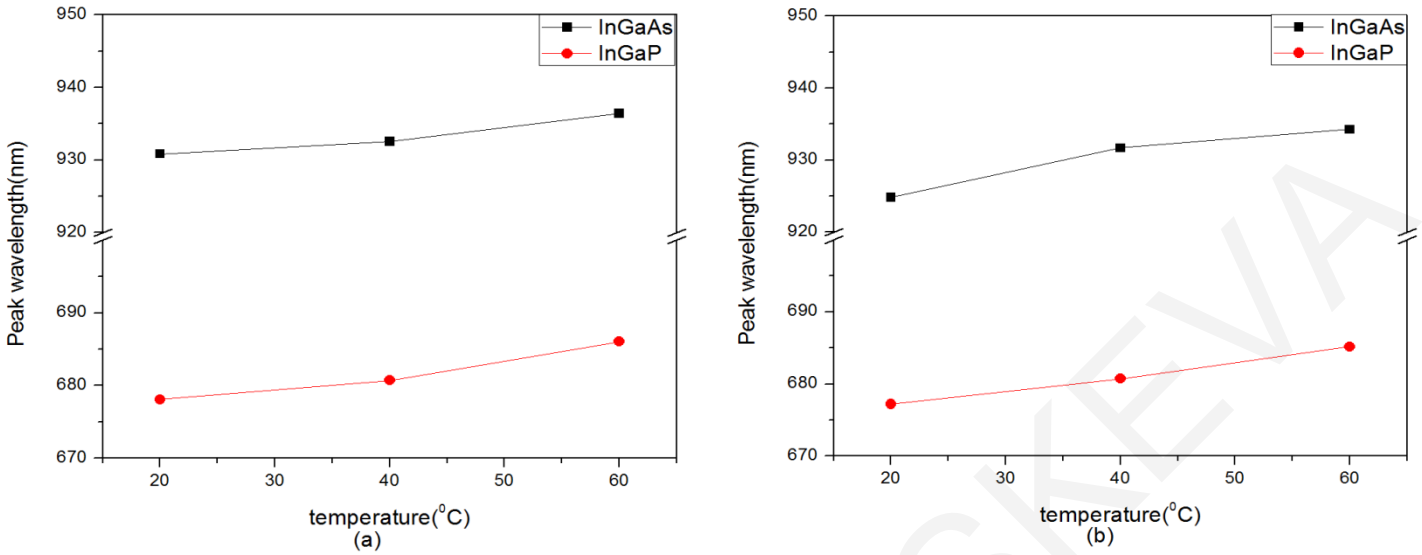

Figure 53: Peak wavelength against temperature at (a) maximum power point and (b) open-circuit conditions.

Besides the energy shift of the luminescence with temperature, another major characteristic of the emission peaks is the exponentially dropping edges. The energetically lower slope remains constant against temperature while the higher one gets flatter with increasing temperature (Figure 54). This is in agreement with recently published results and is attributed to temperature independent density of states below band-gap and Boltzmann distributed carrier emission above that [61]. Specifically, the low energy luminescence is emitted by energetic states in the band-tails below the fundamental band-gap of the semiconductor which is a temperature-independent density of states. However, the high energy luminescence is emitted from Boltzmann distributed carriers which are temperature dependent.

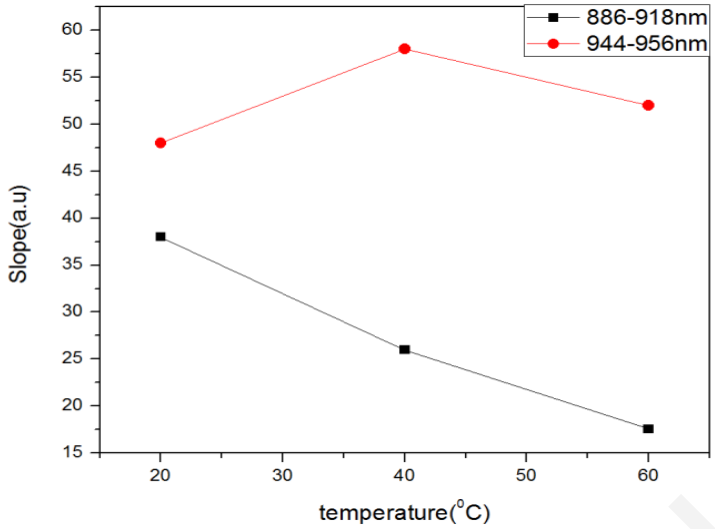

Figure 54: Slope of the higher and lower energy dropping edges of the middle junction. The lower energy dropping edge remains quite constant while the higher energy dropping edge reduces.

4.4 Luminescent emission under outdoor solar irradiance

Outdoor measurements were also performed for the observation of radiative emission under open- circuit and in real solar irradiance conditions. The device was placed on a solar tracker that followed the sun to within an error of 0.1°. The temperature of the cell during the optical measurements was measured to be 30°C. The measurements were performed under open-circuit conditions at midday since at that time the solar irradiation is higher and stable. An irradiance concentration of 6 suns on the device was achieved with a Fresnel lens. The Direct Normal Irradiance taken from the pyrheliometer at the time of the measurement was 777 W/m^2 while the Global Irradiance measured from the pyranometer was 996 W/m^2. The emission was captured by a fiber optic cable used to direct light to a Silicon-CCD spectroradiometer. The outdoor radiative emission spectrum as seen in Figure 55 under concentrated solar irradiation shows clearly the significant radiative recombination of the carriers at the band-edges of the top and middle junctions which indicates that photons are likely to be directed towards and absorbed by middle (InGaAs) and bottom (Ge) junctions respectively. The peak from the Ge is not shown in the graph since it is beyond the sensitivity of the spectroradiometer. The strong emission from the device shows clearly that radiative emission is significant under concentrated solar irradiation and open-circuit conditions confirming the indoor results using the sun simulator. An important observation is that under outdoor illumination the InGaP radiation

peak is relatively increased compared to the InGaAs peak. This is probably attributed to the higher outdoor irradiation below 680 nm compared to the Xenon lamp illumination.

Indoor and outdoor tests of the samples have shown that the presence of radiative emission occurs under broadband solar irradiance and high intensity sun simulator. The results suggest that triple-junction devices used for CPV applications have significant radiative effects that affect the energy yield of the modules and these have to be taken into account.

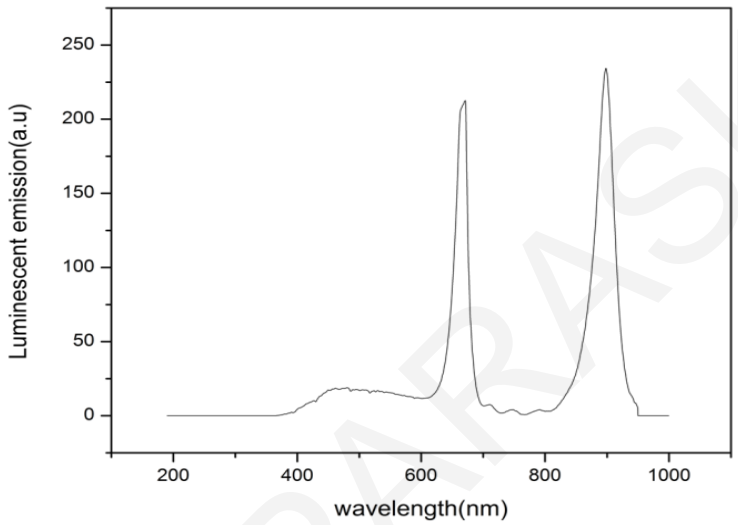

Figure 55: Outdoor emission of the InGaP/InGaAs/Ge under 6 suns. The measurements were performed during midday and under open-circuit conditions.

Conclusions

In summary, combined EL and PL measurements have been used to investigate the radiative recombination and losses from the top junctions in a triple- junction device under a high intensity solar simulator. Such measurements are necessary for the examination of the extent of radiative recombination which can affect the performance of the PV cells. Radiative signals from the band-gap edges of the top InGaP and middle InGaAs are clearly observed at high and low concentrations. The emission signal in the multi-junction device was obtained also at higher temperatures. Outdoor results have demonstrated the presence of luminescent emission from a multi-junction device under real operating conditions.

Chapter 5

Outdoor monitoring of different technology multi-junction devices

5.1 Introduction

Apart from indoor characterization, outdoor investigation of the electrical properties of multi-junction devices has been performed in an attempt to gain knowledge on multi-junction solar cell performance under outdoor field conditions and also to investigate the impact of spectral sensitivity of the cells upon their operating efficiencies in the field. High efficiency multi-junction solar cells are finding promising terrestrial applications within concentrator photovoltaic (CPV) systems that offer to deliver higher overall conversion efficiencies than conventional flat panel photovoltaic installations. Different technologies of multi-junction devices have been tested outdoors in order to demonstrate the advantages of each technology. Lattice matched and upright metamorphic multi-junction cells, which exhibit different spectral responses, have been tested outdoors for several months in order to gather field performance data to evaluate the effect of spectral sensitivity upon the energy yield of multi-junction cells. The spectral content of sunlight over a year varies and as a result significant differences may be apparent on the energy yield of different spectral response multi-junction devices.

Since multi-junction solar cells are more sensitive to the spectral variation of the solar irradiance high quality spectrum measurements are essential for the extraction of the output of the solar cells. Therefore, in order to evaluate the energy yield potential of multi-junction devices at a particular location, spectral measurements should be taken routinely. For that

purpose calibration of spectroradiometers and investigation of measurement uncertainties is essential for understanding and predicting the impact of spectral irradiance upon concentrator photovoltaic technologies that use multiple-junction cells.

Furthermore, comparison of similar technology cells but with different optical elements used for concentration has been performed. Specifically, compound parabolic concentrators have been used to increase cell efficiency through correction of aberrations of the primary optics and demonstrate the potential advantages that such a design can have. The use of appropriate optical elements for light concentration can maximize the module performance at outdoor operating conditions and its examination is necessary.

5.2 State of the art

For high concentration systems, III-V based cells appear more promising compared to Silicon due to the better exploitation of the sunlight energy since the multi-junction cells are being more sensitive to a wider spectrum of the incoming sunlight [64]. The highest full-size PV module concentrator standard test condition (CSTC) efficiency of 38.9% was achieved with a monolithic 4-junction cell (GaInP/GaAs/GaInAs/InP) of 46% efficiency[65]. For the combination of a full-glass lens and a 4-junction cell of 46% efficiency (mono-module), the I-V measurements conducted outdoors resulted in a CSTC efficiency of 43.4% (aperture area of 18.2 cm^2) [66]. The CSTC efficiency of 43.4% is the highest reported value for direct conversion of sunlight to electricity so far. The ongoing efficiency improvements are one reason for today's strong interest in III-V based high concentration CPV systems.

Silicon-on-glass (SOG) Fresnel lenses are the most common optical elements used in concentrator photovoltaics with typical efficiencies of 80-90% [67]. However, SOG Fresnel lenses are not the optical elements with the highest possible efficiency. There are losses due to the geometry of a Fresnel lens and due to material effects like temperature and chromatic aberration [68]–[70]. The use of second stage optical elements in concentrator modules is potentially one way to increase cell efficiency through correction of aberrations of the primary optics and to increase flux concentration levels at the cell. Preliminary measurements with compound parabolic concentrators demonstrated an outdoor module efficiency of 28.5% [71].

Due to increased flux concentration levels higher current in a compound parabolic concentration module was observed in previous measurements [72].

Different types of multi-junction solar cells were used in concentrating photovoltaics [73]. Lattice-matched multi-junction solar cells with efficiencies up to 39% under concentrated light (453 x AM1.5) dominated the market [74]. Detailed balanced calculations, exhibited that the band-gap combination of the lattice matched design was not optimally adjusted to the solar spectrum [75]. For that reason different approaches have been suggested on how to achieve current matching [76], [77]. One useful method to improve solar cell efficiency and keep current matching of all junctions is the use of metamorphic multi-junction solar cells [78]. The upright metamorphic concept lowers the excess current in the bottom cell by lowering the bandgaps of the top and middle junctions [37]. Initial investigations demonstrated an increase in the thermodynamic limit by about 6% compared to lattice matched triple-junction cells [37].

Lattice matched and upright metamorphic multi-junction cells, which exhibit different spectral responses, have been tested outdoors for several months in order to gather field performance data to evaluate the effect of spectral sensitivity upon the energy yield of multi-junction cells. Finally, cells with secondary optics have been tested for the assessment of the increase in performance in the presence of different optical elements within the module.

5.3 Calibration of spectroradiometers for outdoor direct solar spectral irradiance measurements

Prior to the performance investigation of multi-junction devices and its correlation with spectrum measurements, high quality solar spectral measurements are essential. The solar spectrum arriving on a terrestrial PV device varies with the time of day, the season, the weather conditions and also with the position of the receiver [79], [80]. In order to evaluate the energy yield potential of multi-junction devices at a particular location, high quality spectral measurements should be taken routinely. Moreover, many factors introduce uncertainties during the measurement of solar irradiance affecting the measurement procedure. In an attempt to produce a high quality data set of spectra with minimum uncertainties, first the sources of measurement uncertainty needs to be established and quantified. Understanding the origin and nature of the uncertainties will provide an insight into the factors affecting the uncertainties

encountered during outdoor spectral measurements and will thus assist in finding ways of reducing them.

5.3.1 Experimental apparatus

In an attempt to build a reliable spectral measurement system, two sets of calibrated spectroradiometers have been used. These two systems are of the same type and almost identical. They consist of two units, one for performing measurements in the visible and ultraviolet region of the spectrum (using a silicon based CCD) and the second one for measurements in the near infrared region. The two spectra are merged with dedicated software so that the final spectrum irradiance is in the range 300-1700 nm. The irradiance to be measured is then directed into the units through the use of fibre-optic cables that have a cosine corrector, or diffuser, at their entrance aperture. The outdoor measurement system uses a 7 m long fibre-optic cable to direct light from a mounting point on an accurate solar tracker into a climate-controlled cabinet and into the spectroradiometers. The other set of spectroradiometers uses a 1 m long fibre-optic cable. The experimental set-up used outdoors for the calibration can be obtained in Figure 56.

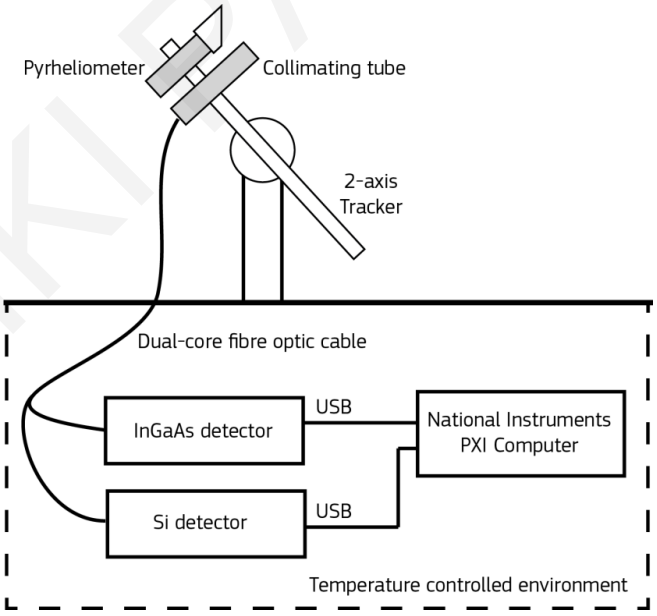

Figure 56: Outdoor measurement set-up used to collect spectrally resolved direct normal solar irradiance data.

To investigate the effect of collimation on the spectrum, a custom-made collimator was fabricated at the Joint Research Centre (JRC) with specifications designed to match those typically found in pyrheliometers (specifically a slope angle of 1 degree and an acceptance angle of ±2.5 degrees). The first spectroradiometer set was calibrated at the JRC under a standard halogen lamp with a NIST-traceable calibration file.

Since it was not possible to perform a direct calibration of the outdoor measurement system, it was necessary to first calibrate the set of spectroradiometers used for indoor measurement at the JRC (System 1), and then to transfer this calibration to the outdoor set (System 2). The original calibration of System 1 was transferred to System 2 by performing a side-by-side measurement of a halogen lamp in the laboratory. In this procedure a number of measurements were performed indoors to determine the uncertainties that may arise from the measurement system, positional sensitivity and lamp stability. After calibration, both spectroradiometers were installed outdoors, and side-by-side measurements were taken again to determine the uncertainties and their origin outdoors. Then a collimator was attached to one of the spectroradiometers and measurements were taken using both collimated and non-collimated systems. Outdoor measurements of global and direct normal irradiance were also taken with a pyranometer and a pyrheliometer respectively and compared with measurements taken with both calibrated spectroradiometers. Any uncertainties introduced at each stage have been calculated.

5.3.2 Results and discussion

5.3.2.1 Indoor calibration

Initially indoor measurements of a standard halogen lamp were performed to calibrate System 1. The results of this procedure are shown in Figure 57.

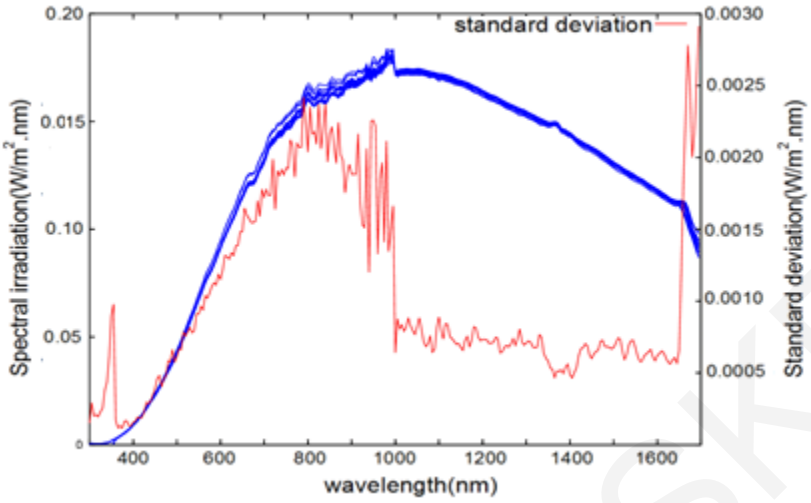

Figure 57: Comparison of repeated spectrum measurements and the associated standard deviation of system 1. Higher deviation in the visible range is clearly observed.

The discontinuity in the middle of the graph indicates the crossover point between the UV-VIS and NIR spectroradiometers used to take the measurements. This discontinuity has been attributed to a combination of noise levels and sensitivity differences (to temperature and perhaps also orientation) and a corresponding higher multiplication factor in the calibration files of this region of the spectrum. Based on the standard deviation calculated as shown, it is clearly observed that the worst-case scenario for uncertainty is obtained in the spectral region between 800-900 nm. This range is very important since it belongs to the spectral region of all types of photovoltaics. Lower noise is seen in wavelengths above 1000 nm, where the NIR detector is used. The uncertainty analysis focused on the following main sources:

1. The measurement equipment (spectroradiometers, lamp, power supplies, fibre optics), which were deemed to affect the measurement repeatability.
2. The positional reproducibility. The transfer of the calibration from one system to another relies on the ability to accurately determine the irradiation falling on a specific plane and to locate both the spectroradiometer input optics on the same plane. The inability to do this perfectly introduces a source of uncertainty.

3. The original calibration uncertainty. System 1 was initially calibrated at JRC. The uncertainty analysis was performed at JRC as part of the internal quality system. The relevant documents report a standard uncertainty level of calibration of ±1.2%.

The estimated values of uncertainties from the indoor analysis are given in Table 9. As seen from Table 9, the largest part of the uncertainty arises from the initial calibration procedure while the uncertainties originating from lamp stability are negligible. The combined standard uncertainty calculated indoors is 1.81%.

Table 9: List of indoor measurement uncertainties of System 1

Source of Uncertainty	Value ±	Prob. Distribution	Divisor	Standard Uncertainty
Initial calibration uncertainty	1.23%	Normal	1	1.23%
Repeatability of measurement	0.29%	Normal	1	0.29%
Accuracy of repositioning of the fiber optic diffuser	2.07%	Rectangular	√3	1.19%
Calibration drift	0.92%	Rectangular	√3	0.53%

Repeated measurements taken from System 2 during calibration indoors are shown in Figure 58. Higher deviation is obseved in the visible range as before. The estimated values of uncertainties in that case are shown in Table 10. The initial calibration uncertainty in that case is the combined standard uncertainty of System 1.

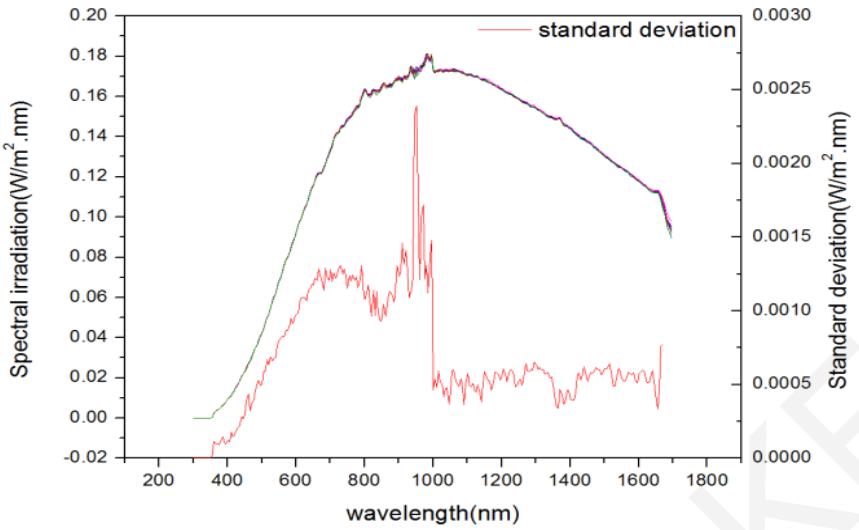

Figure 58: Repeated spectrum measurements and the standard deviation of system 2 taken indoors.

Table 10: List of indoor calibration uncertainties of System 2.

Source of Uncertainty	Value ±	Prob. Distribution	Divisor	Standard Uncertainty
Measurement uncertainty of System 1	1.81%	Normal	1	1.81%
Repeatability of measurement	0.23%	Normal	1	0.23%
Accuracy of repositioning of the fiber optic diffuser	3.59%	Rectangular	√3	2.07%

The combined uncertainty in this case is 2.76% and it is larger than in the case of System 1 as it is expected. The transfer of calibration from one system to another introduces larger uncertainty in spectral measurements.

5.3.2.2 Outdoor operation

After calibration, the two sets of spectroradiometers were installed side-by-side on a solar tracker that followed the sun to within an error of 0.1º. The tracking error is very small but still introduces uncertainty in the spectrum measurements. A typical pair of scans of the global normal spectrum is shown in Figure 59. The measurements showed that the difference in the spectrum varied from 8% to 10% depending on the solar irradiance at the moment of capture. At lower solar irradiance levels the difference was around 8% while at high solar irradiance the

difference could reach 10%. Overestimation of the values of spectral irradiance was observed in system 2.

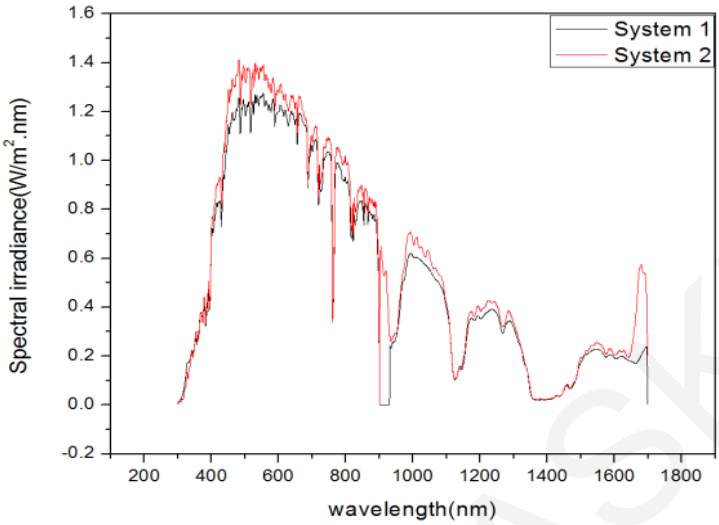

Figure 59: Comparison of the global normal irradiance spectrum taken with both units at midday.

Since both spectroradiometers were calibrated, the difference could be attributed to background noise levels of the devices. As the initial calibration was performed at much lower irradiance levels it was believed that the low signal to noise ratio could account for discrepancies when measuring at higher intensities. For that reason the difference in spectrum between both spectroradiometers at higher irradiance levels is greater whereas at lower irradiances the difference gets smaller.

The units were then calibrated indoors at higher irradiance levels by moving the halogen lamp closer to the spectroradiometer units. The sources of uncertainties remained the same in that case. To confirm the correct operation of the spectroradiometers in an outdoor application the spectroradiometers were again set-up outdoors as in the previous case. Measurements were taken on two different days in order to investigate the stability of the system and the uncertainties introduced by repositioning of the fibre-optic cable (see Figure 60).

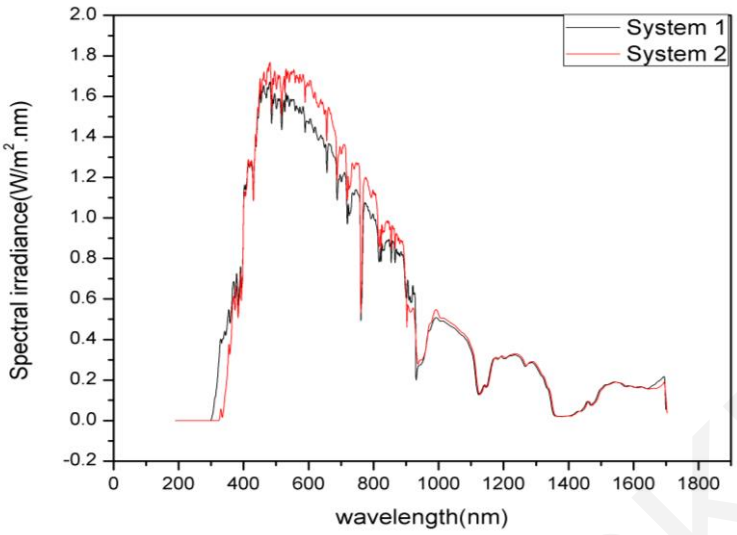

Figure 60: Comparison of global normal irradiance spectrum taken with both units. The calibration of the second unit was performed at higher irradiance levels.

The first measurements demonstrated a 4.4% difference in global irradiance between both spectroradiometers. System 2 presented higher values in the visible range (400-800 nm). The measurements were repeated next day and the difference in solar irradiance between both systems was around 3.5%. The variation of measured spectrum for the first day between both units is present in Figure 61.

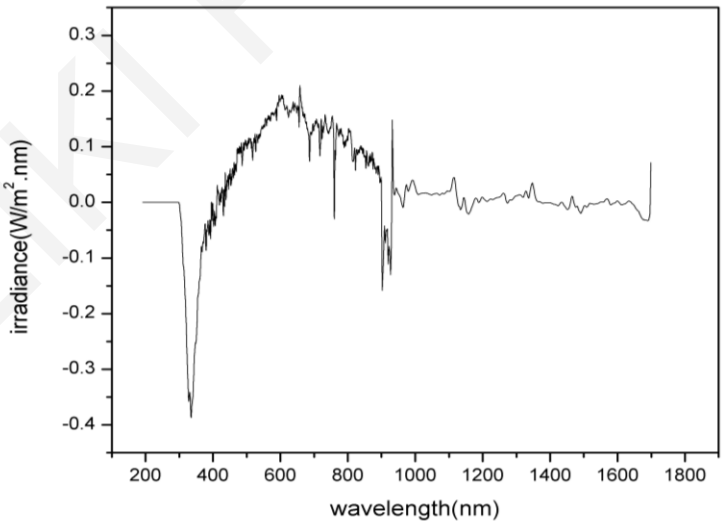

Figure 61: Difference between outputs of both units at each wavelength.

This procedure shows that irradiance levels during calibration have a significant impact on the correct calibration of the systems. This in turn suggests there may be a degree of non-linear behaviour with irradiance intensity, and therefore the calibration of spectroradiometers should be performed close to the irradiance levels under which they will operate. Integration of the spectrum over the entire range results in an average difference of 40 W, which is relatively small and indicates better agreement between data. However, there still remained an unacceptable variation between the two measurement systems, and it was suspected that one significant factor could be the influence of the 7 m long fibre-optic cable.

In an attempt to eliminate the difference between both units and to investigate the effect of the fibre optic cabling we performed the calibration outdoors in-situ. In doing so, it would be possible to reduce the effect of twisting and bending of the fibre optic cable since the whole system would be calibrated with the cable in its normal operating position, apart from a slight change in bending due to tracking over the day. To perform calibration at the actual measurement site (on the solar tracker) calibration was performed during a clear day.

Then an outdoor inter-comparison between units was performed during the day (see Figure 62). Data showed very small differences between the units (around 2%) and this represents the best result obtained.

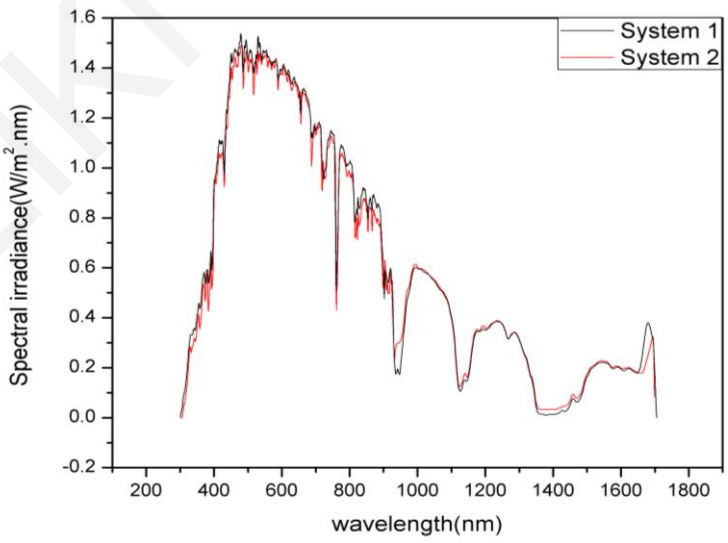

Figure 62: Comparison of irradiance taken with both units. The calibration was performed at the actual measurement site.

Multiple measurements have been carried out at different times of the day. The outdoor inter-comparison showed 1.9% difference between units in the morning, 2% difference during midday and 0.36% in the afternoon where the irradiance levels are low. The measurements show only a small difference over the entire range, mostly in the range covered by the UV-VIS spectroradiometer. Also the estimated values of uncertainties from the outdoor analysis are given in Table 11. In the case of outdoor calibration in-situ the uncertainty due to repositioning is absent since the fibre-optic is not removed during calibration and actual measurement procedures.

The combined standard uncertainty in the case of outdoor calibration is 2.87% and it is slightly higher than in the case of indoor calibration.

Table 11: List of outdoor calibration uncertainties

Source of Uncertainty	Value ±	Prob. Distribution	Divisor	Standard Uncertainty
Measurement uncertainty of System 1	2.20%	Normal	1	2.20%
Repeatability of measurement	1.85%	Normal	1	1.85%

Deviation between both spectroradiometer units at different times of the day is displayed in Figure 63. The average difference between both units is below ±0.1 W/m^2.nm indicating reasonable agreement between measurements. Very small variation of the measurement over time was presented in the infrared region and this indicates stability of the units and systematic effects. However in the visible region the variation over time is larger indicating other sources of uncertainty. This is attributed to changes in the sensitivity of the CCD particularly to variations in ambient temperature and perhaps also total light intensity.

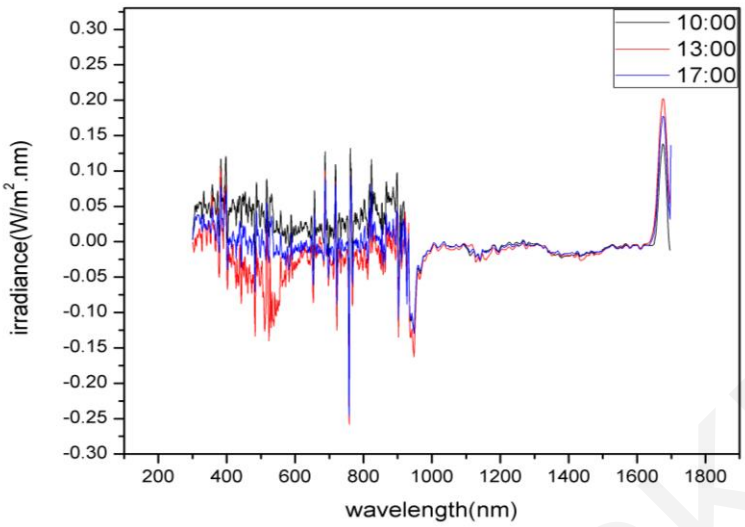

Figure 63: Difference between outputs of both units at each wavelength at different times showing the stability of the measurement.

Comparison of the integrated irradiance of both units with pyranometer measurements indicated differences around 6.4% between data. The comparison cannot be performed directly since the pyranometer has the ability to measure irradiance in wavelengths far beyond 1700 nm. Nonetheless, it is useful to compare relative differences between the sensors because the irradiance over 1700 nm is fairly constant over the conditions of interest.

This comparison showed that performing the calibration at the actual measurement site where the impact of the fibre-optic cabling is minimized appeared to be the best way to reduce errors during the calibration procedure. In all the above cases the sensor integration time was chosen to minimise noise as well as saturation of the measurement. The influence of ambient temperature was suggested as a daily trend in the difference between spectroradiometer and pyranometer measurements. However, this difference was less than 2% over the range of temperatures so far recorded, and therefore did not contribute significantly to the uncertainty of the outdoor measurements.

5.3.2.3 Impact of collimator

Furthermore, a collimator was attached on System 2 outdoors and measurements were taken using both collimated and non-collimated systems to extract the impact of the collimator on spectral measurements. Outdoor data showed reduction of the spectrum in the presence of the

collimator since it cuts out the diffused light, which is mostly of higher energy. Multiple measurements were performed in the presence of the collimator and the corresponding standard deviation was calculated. Higher deviation was present again in the visible region. In an attempt to observe the effect of the dust on the correct operation of the spectroradiometers and to the uncertainties of the system, measurements have been undertaken before and after the cleaning of the collimator (see Figure 64). Measurements after cleaning are almost identical with the measurements taken beforehand. However, the standard deviation of the measurements is much lower after cleaning of the system.

The list of uncertainties in the presence of the collimator is shown in Table 12.

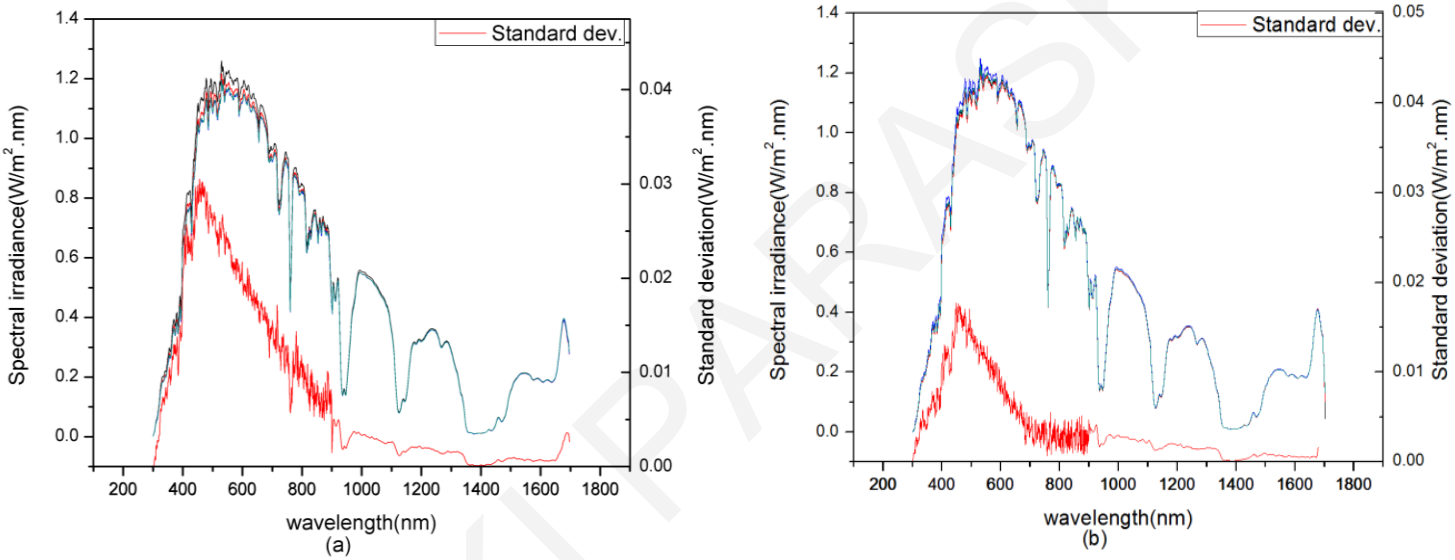

Figure 64: Repeated spectrum measurements and the corresponding standard deviation (a) before cleaning and (b) after cleaning.

Table 12: List of measurement uncertainties in the presence of the collimator.

Source of Uncertainty	Value ±	Prob. Distribution	Divisor	Standard Uncertainty
Initial calibration uncertainty	2.87%	Normal	1	2.87%
Repeatability of measurement	1.75%	Normal	1	1.75%
Accuracy of repositioning of the fiber optic diffuser	3.50%	Rectangular	√3	2.02%

The combined standard uncertainty in the case of the collimated spectroradiometer is therefore 3.92%.

Comparison of the output spectra of the system with the collimator and pyrheliometer has also been performed for short time periods in order to indicate the correct operation of the units as well as calibration drifts that might appear during short-term operation. The spectrum taken with the outdoor unit has been integrated and then compared with the pyrheliometer output. Initially the difference in irradiance between the two units is around 40 W/m^2.nm which corresponds to a difference of 4.4% which is acceptable (Figure 65). After 2 months of continuous operation of the units a comparison was performed again. The difference in irradiance between both systems was found to be 45 W/m^2.nm demonstrating a small drift between the different sensors. The short-term degradation of the operation of the units suggests that periodic validation of the units is required.

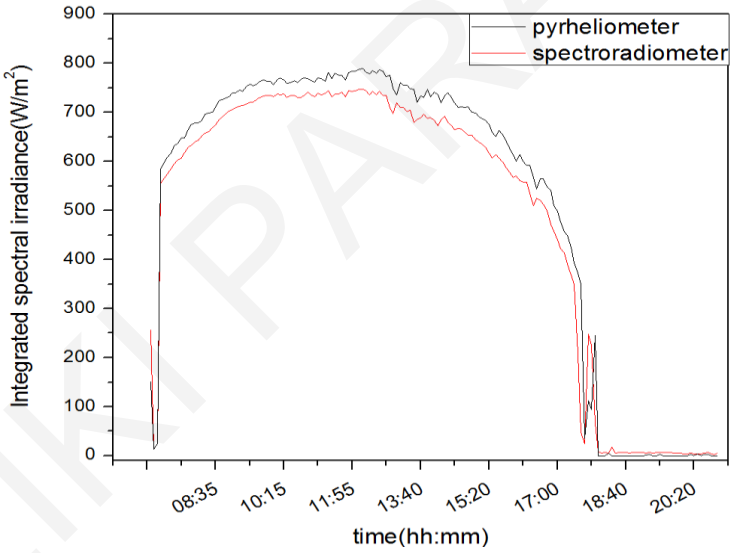

Figure 65: Comparison of integrated spectral irradiance between a pyrheliometer and a spectroradiometer for a day (14/08/2013). The difference between both units reaches 40 W/m^2.nm.

In summary, calibration results showed that there is good measurement repeatability indoors under controlled conditions. Outdoor tests have demonstrated the impact of various factors such as fibre-optic bending and non-linearities on the proper operation of the spectroradiometers. These results showed that calibration at high irradiance levels is required. Non-linearities have been shown to cause significant influence on the correct operation of the spectroradiometers and have to be eliminated. Also calibration on the actual measurement site

has been shown to minimize calibration errors since it may remove errors introduced by twisting/bending of the fibre optic cable.

The results of the calibrated set of spectroradiometer used outdoors are in agreement with broadband measurement devices such as pyranometers and pyrheliometers showing the correct operation of the systems. A comparison of the integrated spectroradiometer data against pyrheliometer and pyranometer measurements differ by around 4.4% for Direct Normal Irradiance (DNI) and 6.4% for Global Normal Irradiance (GNI).

After the calibration of the spectroradiometer units, a high quality set of spectrum measurements is obtained which is required for understanding and predicting the impact of spectral irradiance upon concentrator photovoltaic technologies that use multiple-junction cells.

5.4 Evaluation of Compound Parabolic Concentrators

Next, the impact of secondary optics has been investigated, so two identical solar cells were fabricated but one was constructed with the new secondary optical element and the other was based on the typical Fresnel lens design. The cells have been mounted side-by-side on an accurate solar tracker in Nicosia, Cyprus and connected to a current-voltage characterisation system.

Figure 66(a) shows the normalized power of the two modules. Both current and power were obtained as a function of DNI in order to have an accurate comparison between the modules. The normalised maximum power of both designs is approximately the same. For further investigation of the results and explanation of the behaviour of maximum power, normalised short- circuit current and open-circuit voltage were plotted against the time of day (see Figure 66(b) and Figure 66(c) respectively). Normalised current results showed higher currents for the module with secondary optics indicating better optical efficiency and consequently higher concentration levels. Investigation of the open-circuit voltage of the module with Compound Parabolic Concentrators reveals that it is around 0.05 lower than the module with typical Fresnel configuration. Due to higher concentration levels within the modules with secondary optics the open-circuit voltage is expected to drop to lower values. This is in agreement with

previous investigations which stated an increase of the temperature in the module with compound parabolic concentrators [72]. Likewise, fill factor results indicate the higher operating temperature of the module with Compound Parabolic Concentrators since lower fill factor values have been obtained.

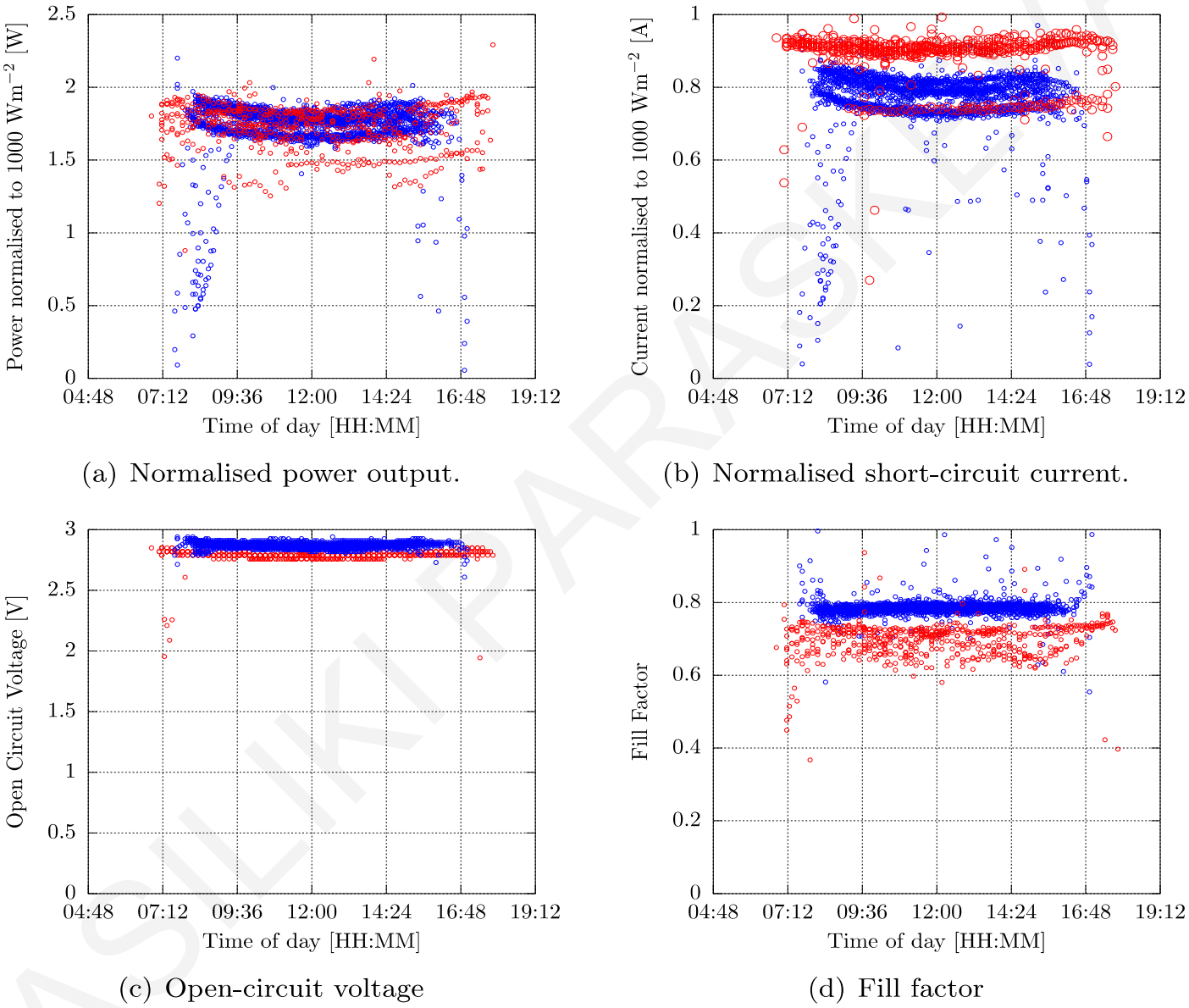

(a) Normalised power output.

(b) Normalised short-circuit current.

(c) Open-circuit voltage

(d) Fill factor

Figure 66: Comparison between the performance of modules with secondary optics (red), and without (blue), against the time of day. The cells under test are quantum well solar cells,

5.5 Evaluation of Lattice Matched (LM) & Upright Metamorphic (UMM) cells

Next outdoor performance of different spectral response solar cells was investigated by using two different design and technology devices. The first technology cell, labelled as type 'A' incorporated a lattice matched structure while cell type 'B' utilized an upright metamorphic structure. The EQE from both cells was measured with the high-resolution EQE set-up and the values of the top and middle junction of both types are shown in Figure 67(b). Type A cells have a narrower response range in both of the junctions compared to the type B cells.

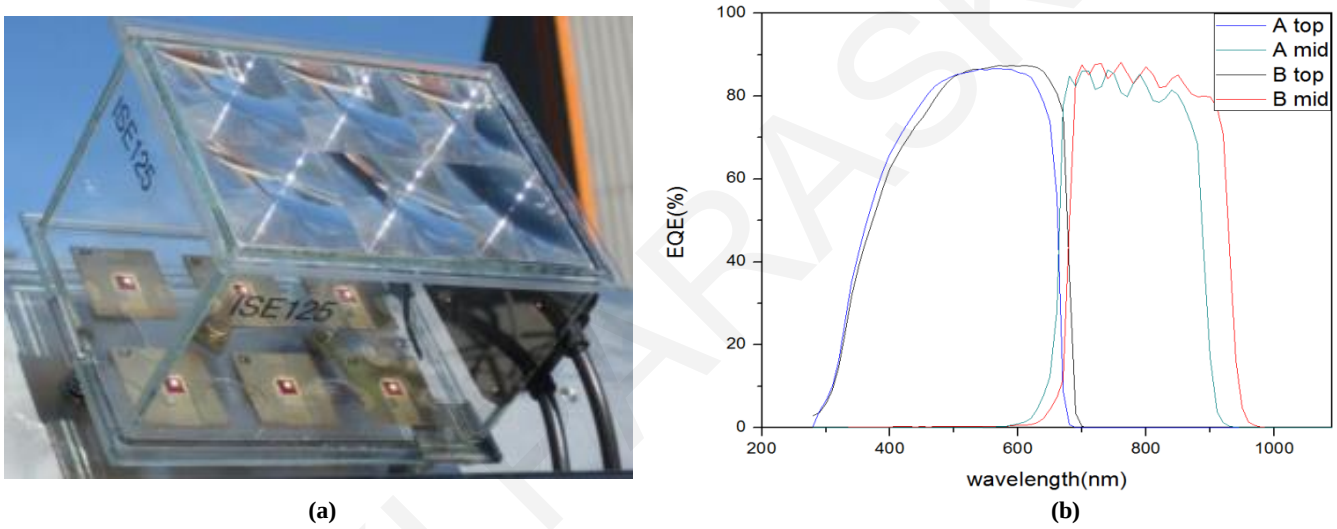

(a) **(b)**

Figure 67: (a) View of one of the modules undergoing outdoor testing, (b) External Quantum Efficiencies of the top and middle junctions measured for the lattice matched (type A) and upright metamorphic (type B) cells. The type B cells exhibit a wider response range for both junctions.

The cells were chosen to be as dimensionally similar as possible, as well as utilizing similar bus-bar designs. The cells were also over-sized for the application to reduce the possibility that slight differences in their characteristics could influence the outdoor performance. View of one module undergoing outdoor testing is provided in Figure 67(a). Four modules were fabricated for outdoor operation incorporating these cells. Two of the modules contained only type A cells while the remaining two modules contained only type B cells. Each module incorporated six triple-junction cells wired in series. The modules were designed to have a low geometric concentration ratio of only 53X to reduce the effect of tracking errors and internal misalignments. The peak irradiance intensity at the centre of the cells was estimated to be

around 2500 suns which was tolerable for both cell types. The modules were an all-glass design and concentration was achieved using SOG Fresnel lenses. They were not hermetically sealed, but allowed an air flow in and out of the enclosure through a filter. The modules characteristics are provided in Table 13. The modules were installed outdoors on a tracker and aligned using a system of spring mounts. Alongside the modules, a pyranometer recording Global Normal Irradiance (GNI), a pyrheliometer for measuring broadband Direct Normal Irradiance (DNI), temperature sensors for measuring back-of-module and ambient temperatures and a collimating tube for collecting light for a spectroradiometer system were installed. The spectroradiometer collected data at a resolution of 2 nm over the range 300-1650 nm with an acquisition time of several milliseconds. A picture of the modules installed on the tracker is provided in Figure 68.

Table 13: Summary of the CPV modules characteristics.

Module ID code	Geometric Concentration	Optical Flux concentration	Active Area	Cell count	Dimensions	Cell Technology
ISE 121	49 X	2000 suns (peak)	96 cm^2	6	L 14, W 10, H 9 cm	Azur 3C40C, Lattice Matched (LM)
ISE 125	49 X	2000 suns (peak)	96 cm^2	6	L 14, W 10 H 9 cm	Azur 3C42C, Upright Metamorphic (UMM)

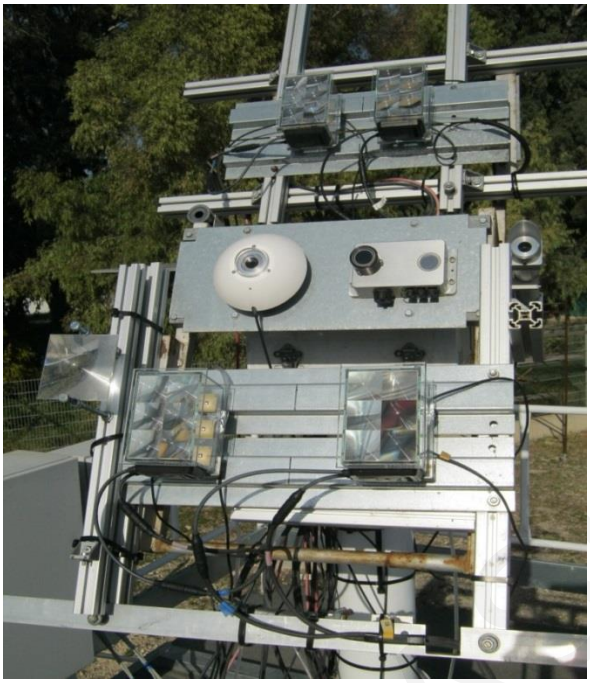

Figure 68: Outdoor measurement apparatus.

The four outdoor test modules were used to collect field data for several months. A custom current-voltage (I-V) tracing system was used to take sequential measurements of the I-V characteristics of each module. The captured I-V curves provided information about open-circuit voltage, short-circuit current, fill factor as well as maximum power of the modules. Simultaneously the ambient operating conditions of the modules were recorded. The spectral data was collected in order to later analyze the output of the modules as a function of the spectral content of the solar irradiance.

In an attempt to validate the spectroradiometer results the short-circuit current of the modules was calculated using (2.6) which is based on the spectral response measurements of each cell type and the measured spectral irradiance at each time step. The simulated and measured short-circuit current for type A cells are shown in Figure 69. As can be seen from the close match of the simulation with the measured current, the modules behave as expected.

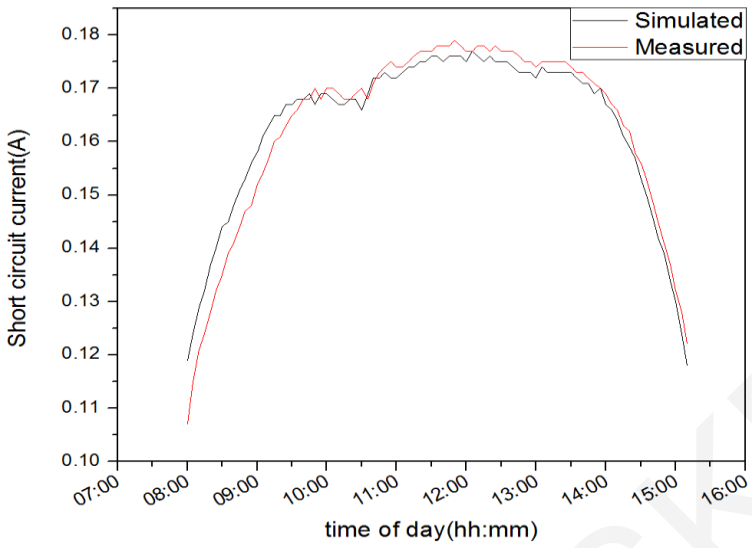

Figure 69: Plot showing the change in measured short-circuit current of the module containing cells of type A on the 23rd of December 2014, alongside a simulation of the current.

The spectral response of the cells as well as the measured spectrum were used for the simulation of the current from each junction in the cells. The simulated short-circuit current for each junction in the type A cells for the 23rd of December is given in Figure 70. A clear change of the limiting junction was obtained at approximately 09:15 and 13:50 indicating a distinct change of the limiting junction on this day. In the morning and in the afternoon the current limiting junction is the top one while in the middle of the day the current of the solar cell is limited by the middle junction. The bottom Ge junction always has a high short-circuit current since its spectral response covers a very broad range of wavelengths.

In order to validate the results the fill factor values were plotted for the same day. As discussed in section 2.11 the minimum of the fill factor indicates the current matching point of junctions in a multi-junction device. The results can be obtained in Figure 71.

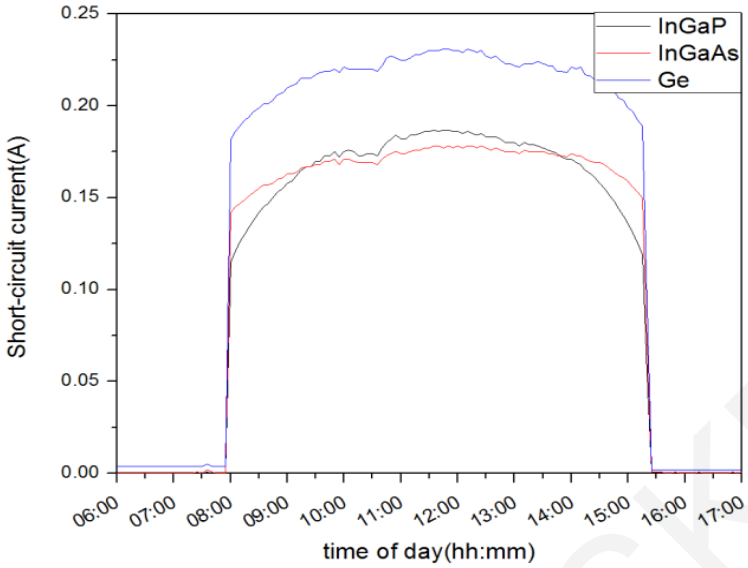

Figure 70: Simulated junction currents for the type A cells, calculated using their spectral response, the measured direct normal irradiance on the 23rd of December 2014 and an estimated lens efficiency.

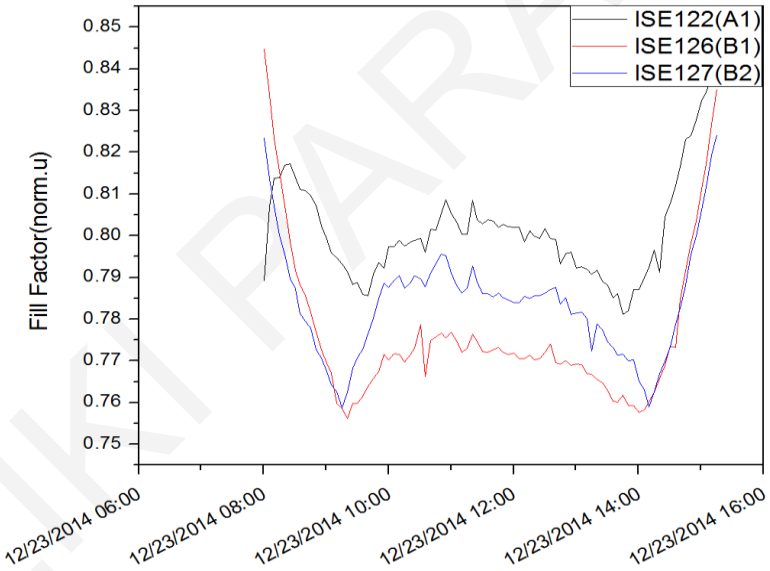

Figure 71: Plots of the change in the fill factor for three modules under test (two of type B and one of type A) on the 23rd of December 2014. The fill factor shows a distinctive inflection where the change in limiting junction occurs.

The plot in Figure 71 shows a clear inflection point where the current generation in the top and middle junctions of the cells is balanced in each module. At either side of the inflection point the top or the middle junction is limiting the current and causes a corresponding increase in the device fill factor. This inflection point happens at different times depending on the spectral response of the cells and as shown in Figure 71 clearly distinguishes one cell type from another. The transition from top to middle current limiting junction in type A cells happens later in the morning and earlier in the afternoon compared to type B cells. Consequently, some differences in the performance ratio of the two cells over the day can be expected.

The performance ratio (PR) was therefore calculated to provide a performance indication for each module relative to its expected output under standard test conditions. The instantaneous performance ratio was calculated for each current-voltage sweep using the performance efficiency of each module at concentrator standard operating conditions (CSOC). The CSOC performance was determined according to the procedure given in the draft standard IEC62670-3 *PV Performance Testing-Performance Measurements and Power Rating*. The data for the analysis was obtained by filtering the entire output dataset for the CSOSC conditions of DNI, ambient temperature, wind speed and spectral matching ratio. The average values for maximum power and efficiency were then obtained from the remaining data. The results are summarized in Table 14.

Table 14: Concentrator Standard Operating Conditions performance summary for the four test modules.

Cell type	Module ID	P_{max} (W)	Efficiency (n_{csoc}) (%)
A	ISE 122	2.306	26.69
A	ISE 123	2.309	26.72
B	ISE 126	2.535	29.36
B	ISE 127	2.594	30.03

The performance ratio was therefore calculated according to (5.1) where n_{CSOC} is the module efficiency at CSOC conditions, G_{DNI} (t) and P_{mpp} (t) are the direct normal irradiance and maximum power of the module at time t respectively and A is the module area.

$$PR = \frac{\sum P_{mpp}(t)}{\sum n_{CSOC}.G_{DNI}(t).A} \quad (5.1)$$

The performance ratio of each module was then determined over the entire measurement period of 8 months and the mean performance ratio of each module was calculated. The final performance ratio values are presented in Table 15 and show close agreement between the different modules, with no discernible difference outside of the standard uncertainty of the measurements.

Table 15: Performance ratio of the modules for eight months.

	Type A module	Type B module
Performance Ratio	0.981	0.983

The close match between the performance ratios of the two cell technologies presented in Table 15 suggests that either the different spectral response of the two cell types has little effect on their energy yield per watt-peak installed or that effect is being obscured by more prominent influences such as temperature and optical efficiencies. On the other hand, as the examination of the module fill factors in Figure 71 has shown, there is a discernible difference in the hourly performance of the different module types. Hence, a closer examination of the dataset is warranted in order to explain the similarity in the final PR value.

The spectral matching ratio (SMR) value can be used to look for trends in performance efficiency of the modules with changing spectral irradiance. The SMR represents the ratio of the carrier generation in the different junctions and becomes unity when the balance is equal to that occurring under AM1.5D spectrum (see 5.2). The most important SMR value is calculated between the top and the middle junctions, as there are almost always the current limiting junctions, and is referred as SMR1.

$$SMR_{j-k} = \frac{i_{j,m}/i_{k,m}}{i_{j,AM1.5}/i_{k,AM1.5}} \quad (5.2)$$

Using the SMR1 value calculated using the spectral response of the cells, the operating efficiency of the modules was calculated and binned in SMR1 steps of 0.02. The average efficiency of each bin has been plotted for two different rear-of-module temperature bands in Figure 72 and shows a set of distinct trends.

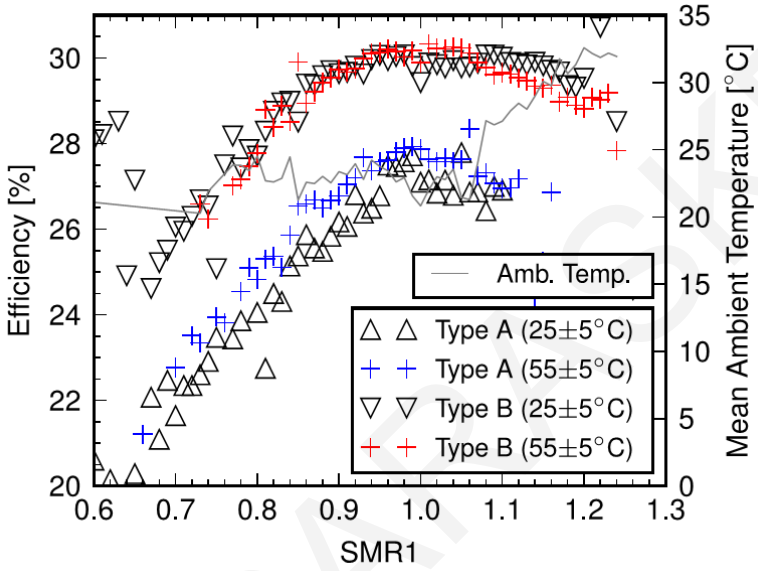

Figure 72: Plot of the mean measured efficiency for the two module types as a function of the spectral matching ratio SMR1. The relationship is plotted for two different rear-of-module temperature bands for each module type. A trend can be discerned with a peak efficiency occurring in each case at the point where the top two junctions are current balanced. For consideration, the mean recorded ambient temperature is also plotted for each SMR1 band.

As expected, the optimum efficiencies seen in the curves of Figure 72 are observed near the SMR=1 line, where the carriers in the two top junctions become current balanced. This is slightly offset in both cases, but particularly in the case of the type B module, which contain cells tuned for a more red-rich spectral distributions. However, that difference is very small indicating that both cells are already operating quite close to their optimum under the spectral resource present in the testing location.

Conclusions

From the investigation of the performance of the improved optical arrangement with Compound Parabolic Concentrators, a number of advantages of the new configuration were arisen. A higher flux concentration in the target area and higher currents of the triple-junction

cell were obtained. However, the higher temperatures apparent in modules with secondary optics lead to the reduction of the overall efficiency of modules with Compound Parabolic Concentrators due to voltage drop.

Comparison of cells with different spectral responses such as lattice matched and upright metamorphic multi-junction cells has established that the different spectral response of cells does not have any influence on the long-term performance of the cells. The analysis has shown that both cell types operate close to their optimum point under the particular testing conditions, which is reflected in the similarly high CSOC performance ratios.

Finally, a detailed investigation of the uncertainties present during spectrum measurements has been provided, thus establishing a reliable system of spectral measurements with known uncertainties.

Chapter 6

Conclusions

Various characterization methods such as Spectral Response (SR), Electroluminescence (EL) and Photoluminescence (PL) were used to gain knowledge on the material and optoelectronic properties of multi-junction devices. Through this work, a deeper understanding of the material properties was achieved. Accurate SR measurements are essential for PV solar cells since they indicate the ability of the material to produce current. Dark SR measurements have been explored giving an insight into the effect of finite shunt resistance in a multi-junction device and are highly recommended before the actual EQE measurements. Investigation of the impact of voltage bias on SR measurements at low and high light intensity conditions has indicated the importance of voltage–light bias on such measurements. The ideal light bias conditions that should be present during SR measurements of the middle junction lie in the range between 0.45mW/cm^{2}and 1.5mW/cm^2. Those values correspond to top junction photocurrents. These conditions are required for the correct characterization of multi-junction PV cells. Finally, the impact of luminescent coupling effects on SR measurements have been revealed and discussed at high light intensity conditions. Those measurements demonstrated that luminescent coupling effects at high light intensity conditions results to EQE reduction and this behavior is more pronounced at the higher material quality samples.

In order to further investigate luminescent coupling effects, PL measurements have been conducted in different quality and structure materials and at different temperatures. Results

demonstrated that coupling current in lower quality materials is lower due to the presence of shunts which act as alternative paths for the current. Specifically, it was found that 2.3% of the recombination current in the top junction is converted to coupling current in the middle junction at high shunt resistance materials while in lower shunt resistance materials the amount of recombination current which converted to coupling current was found to be quite lower and 2.1%. PL measurements were analyzed based on the theoretical approach of the 1-diode model in a double junction device. The model takes into account luminescent coupling effects between junctions. Successful experimental support of the theoretical approach was provided. The coupling efficiency coefficient for different shunt resistance and structure devices has also been calculated based on experimental results. Furthermore, modelling of the shunts has been implemented. A physical model of a junction which takes into account local ohmic shunts has been used to validate the experimental data. Luminescent emissions from the two modelled junctions with different amount of defects were calculated and were compared favourably with experimental observations. PL measurements at different structure multi-junction cells were conducted also in an attempt to establish the impact of material design on coupling effects. Triple-junction solar cells with heterojunctions in the middle junction in combination with lower spacer thickness were found to enhance coupling. Furthermore, cells with larger doping in the emitter on the top junction were found to promote coupling effects. The impact of temperature of coupling effects was also investigated. The experimental results demonstrated a 30% reduction of the initial coupling current at temperature of 45°C.

Subsequently, combined EL and PL measurements under a high intensity sun simulator were carried out in order to investigate radiative losses and consequently the possibility of the presence of luminescent coupling in InGaP/InGaAs/Ge at different operating conditions of the tandem. Examination of radiative losses is required since this can significantly affect the performance of the solar cell. Radiative emission was clearly observed at maximum power point conditions of the tandem indicating its presence during real outdoor operating conditions. Luminescence was detected at high temperatures up to 60°C and at higher concentration levels. An exponential trend was found for the integrated luminescent emission against voltage bias while a linear relationship was obtained for the integrated luminescent emission against

concentration level. Furthermore, the integrated luminescent emission was found to reduce linearly with temperature increase.

Outdoor testing of different technology multi-junction devices is important to indicate the long term energy yield of those cells at real field conditions. Outdoor measurements can demonstrate the impact of the spectral response on the energy yield of devices and show how the "tuning" of the spectral response at different multi-junction devices can lead to better exploitation of the local spectral resource. For the purpose of this research an advanced infrastructure was used that comprised of a solar tracker, outdoor PV operational and meteorological sensors and a data-acquisition system. The acquired and stored data were subsequently used for the analysis of various performance aspects. Different spectral response multi-junction solar cells have been exposed outdoors for the detection of any differences on the energy yield of the cells. No significant difference on the performance of the solar cells was detected indicating that spectral tuning might not be required for the spectral conditions of Cyprus. Furthermore, the impact of secondary optics on the module performance has been examined outdoors. Two similar solar cells, one with compound parabolic concentrator and the other one without have been monitored at the test site. No significant difference was observed on the power performance of the two modules.

Future work

The manufacturing of 4-junction multi-junction solar cell demonstrates a successful pathway for reaching highest conversion efficiencies with III-V multi-junction solar cells. Increasing the number of junctions generally offers the potential to reach even higher efficiencies. However, in that case the material quality and the choice of bandgap energies are of major importance. With the production of 4-junction solar cells challenges have to be met regarding their characterization and the optical interactions between junctions in those devices. The EQE measurements of such devices will be challenging and the appropriate voltage and light bias conditions for each junction have to be addressed. Furthermore, due to the direct band-gap

nature of the junctions in the 4-junction cell, luminescent coupling effects may be obtained at high light bias intensity conditions. The existence or the amount of coupling that might exist in those devices is unknown. The investigation of the carrier dynamics will demonstrate the initial coupling between junctions (if exist) with a femtosecond resolution and will provide an insight towards the carrier's relaxation in the tandem at very short time scales.

Tandem cells combining III-V cells above Silicon or perovskite on Silicon are very promising and merits investigation. Recent work demonstrated tandem solar cells combining Silicon and perovskite absorbers with the potential to outperform state-of-the-art high efficiency silicon single junction devices. The characterization of those novel cells is challenge and the investigation of their material properties essential.

Finally outdoor evaluation of the tandem devices at different ambient conditions will demonstrate the performance degradation of the tandem during their outdoor exposure.

References

[1] T. Tibbits, P. Beutel, E. Oliva, and C. Karcher, "New Efficiency Frontiers with Wafer-Bonded Multi-junction Solar Cells," *Proc.29th Eur. Photovolt. Sol. Energy Conf. Exhib.*, pp. 1975–1978, 2014.

[2] E. D. Jackson, "Areas for improvement of the semiconductor solar energy converter," *Trans. Conf. use Sol. energy,Tuckson,Arizona*, vol. 5, p. 122, 1955.

[3] Y. T. Moon R, James L, Vander H, "Multigap solar cells requirements and the performance of AlGaAs and Si cells in concentrated sunlight," in *13th IEEE Photovoltaic Specialist Conference*, 1978, pp. 859–867.

[4] "International Standard IEC 60904-8, Mesurement of Spectral Response of a Photovoltaic Device, International Electrotechnical Commision," 2007.

[5] "American Standard Test Procedure ASTM E2236-10 2010 Standard Test Methods for Measurement of Electrical Performance and Spectral Response of Nonconcentrator Multijunction Photovoltaic Cells and Modules."

[6] K. Emery, D. Dunlavy, H. Field, and T. Moriarty, "Photovoltaic Spectral Responsivity Measurements," *Proc. 2nd World Conf. Photovolt. Energy Convers.*, pp. 2298–2301, 1998.

[7] J. Burdick and T. Glatfelter, "Spectral Response and I-V measurements of tandem amorphous-silicon alloy solar cells," *Sol. Cells*, vol. 18, pp. 301–314, 1986.

[8] K. Emery, C. R. Osterwald, J. Burdick, G. Virshup, and P. Alto, "A comparison of the errors in determining the conversion efficiency of multi-junction solar cells by various methods," *Sol. Cells*, vol. 24, pp. 371–380, 1988.

[9] S. Arendt and S. Bailey, "Annual Book of ASTM Standards volume 12, E2236-05 Standard Test Method of Measurement of Electrical Performance and Spectral Response of Nonconcentrator Multijunction Photovoltaic Cells and Modules," pp. 868–872, 2005.

[10] M. Meusel, C. Baur, G. Letay, A. W. Bett, W. Warta, and E. Fernandez, "Spectral response measurements of monolithic GaInP/Ga(In)As/Ge triple-junction solar cells: Measurement artifacts and their explanation," *Prog. Photovoltaics Res. Appl.*, vol. 11, no. 8, pp. 499–514, 2003.

[11] C. Baur, M. Meusel, F. Dimroth, A. W. Bett, M. Nell, G. Strobl, S. Taylor, and C. Signorid, "Analysis of the radiation hardness of triple- and quintuple- junction space solar cells," *Proc.31st IEEE Photovoltaics Spec. Conf.*, pp. 548–551, 2005.

[12] G. Siefer and a. W. Bett, “Calibration of III-V Concentrator Cells and Modules,” *2006 IEEE 4th World Conf. Photovolt. Energy Conf.*, pp. 745–748, 2006.

[13] G. Siefer, C. Baur, A. W. Bett, and F. Ise, “External Quantum Efficiency measurements of Germanium bottom subcells: measurement artifacts and correction procedures.,” *Proc.35th IEEE Photovoltaics Spec. Conf.*, pp. 704–707, 2010.

[14] S. H. Lim, K. O’Brien, E. H. Steenbergen, J.-J. Li, D. Ding, and Y.-H. Zhang, “Analysis of spectral photocurrent response from multi-junction solar cells under variable voltage bias,” *Proc.35th IEEE Photovolt. Spec. Conf.*, pp. 712–716, Jun. 2010.

[15] C. J. Hibberd, F. Plyta, C. Monokroussos, M. Bliss, T. R. Betts, and R. Gottschalg, “Voltage-dependent quantum efficiency measurements of amorphous silicon,” *Sol. Energy Mater. Sol. Cells*, vol. 95, no. 1, pp. 123–126, 2011.

[16] S. H. Lim, J. Li, E. H. Steenbergen, and Y. Zhang, “Luminescence coupling effects on multijunction solar cell external quantum efficiency measurement,” *Prog. Photovoltaics Res. Appl.*, vol. 21, pp. 344–350, 2011.

[17] J. Li, S. H. Lim, C. R. Allen, D. Ding, and Y.-H. Zhang, “Combined Effects of Shunt and Luminescence Coupling on External Quantum Efficiency Measurements of Multijunction Solar Cells,” *IEEE J. Photovoltaics*, vol. 1, no. 2, pp. 225–230, 2011.

[18] C. Baur, M. Hermle, F. Dimroth, and A. W. Bett, “Effects of optical coupling in III-V multilayer systems,” *Appl. Phys. Lett.*, vol. 90, no. 19, p. 192109, 2007.

[19] H. Yoon, R. R. King, G. S. Kinsey, S. Kurtz, and D. D. Krut, “Radiative coupling effects in InGaP/GaAs/Ge multijunction solar cells,” *Proc.3rd World Conf. Photovolt. Energy Convers.*, pp. 745–748, 2003.

[20] G. S. Kinsey and K. M. Edmondson, “Spectral Response and Energy Output of Concentrator Multijunction Solar Cells,” *Prog. Photovoltaics Res. Appl.*, vol. 17, pp. 279–288, 2009.

[21] R. Adelhelrn and K. Biicher, “Performance and parameter analysis of tandem solar cells using measurements at multiple spectral conditions,” vol. 50, pp. 185–195, 1998.

[22] S. Nann and K. Emery, “Spectral effects on PV-device rating,” *Sol. Energy Mater. Sol. Cells*, vol. 27, pp. 189–216, 1992.

[23] M. Bliss, T. R. Betts, and R. Gottschalg, “Performance measurements at varying irradiance spectrum, intensity and module temperature of amorphous silicon solar cells,” *Proc.35th IEEE Photovoltaics Spec. Conf.*, pp. 2660–2665, 2010.

[24] F. a. Rubinelli, R. L. Stolk, A. Sturiale, J. K. Rath, and R. E. I. Schropp, “Sensitivity of the dark spectral response of thin film silicon based tandem solar cells on the defective

regions in the intrinsic layers," *J. Non. Cryst. Solids*, vol. 352, no. 9–20, pp. 1876–1879, 2006.

[25] M. Pravettoni and H. Müllejans, "A method for the detection and quantitative estimation of low shunt resistances via the dark spectral response measurements of multijunction photovoltaic cells: theory and results," *Proc.37th IEEE Photovoltaics Spec. Conf.*, pp. 1726–1730, 2011.

[26] M. Pravettoni, "To Bias or Not to Bias? An 'How-To' Guide for Spectral Response Measurements of Thin Film Multi-Junction Photovoltaic Modules," *MRS Proc.*, vol. 1426, p. 10.1557/opl.2012.838, 2012.

[27] M. Pravettoni, R. Galleano, A. Virtuani, H. Müllejans, and E. D. Dunlop, "Spectral response measurement of double-junction thin-film photovoltaic devices: the impact of shunt resistance and bias voltage," *Meas. Sci. Technol.*, vol. 22, no. 4, p. 045902, 2011.

[28] S. Kurtz, K. Emery, and J. Olson, "Methods for analysis of two-functional, two-terminal photovoltaic devices," *Proc.24th IEEE Photovolt. Spec. Conf.*, pp. 1733–1737, 1994.

[29] M. Meusel, R. Adelhelm, F. Dimroth, A. W. Bett, and W. Warta, "Spectral mismatch correction and spectrometric characterization of monolithic III-V multi-junction solar cells," *Prog. Photovoltaics Res. Appl.*, vol. 10, no. 4, pp. 243–255, 2002.

[30] A. S. Brown and M. A. Green, "Radiative coupling as a means to reduce spectral mismatch in monolithic tandem solar cell stacks-theoritical considerations," *Proc.29th IEEE Photovolt. Spec. Conf.*, pp. 868–871, 2002.

[31] G. W. Shu, J. Y. Lin, H. T. Jian, J. L. Shen, S. C. Wang, C. L. Chou, W. C. Chou, C. H. Wu, C. H. Chiu, and H. C. Kuo, "Optical coupling from InGaAs subcell to InGaP subcell in InGaP/InGaAs/Ge multi-junction solar cells.," *Opt. Express*, vol. 21, pp. 123–30, 2013.

[32] G.-W. Shu, N.-N. Ou, P.-Y. Hsueh, T.-N. Lin, J.-S. Wang, J.-L. Shen, C.-H. Wu, and C.-H. Ko, "Measuring Photovoltages of III–V Multijunction Solar Cells by Electroluminescence Imaging," *Appl. Phys. Express*, vol. 6, no. 10, p. 102302, 2013.

[33] D. J. Friedman, J. F. Geisz, and M. A. Steiner, "Analysis of Multijunction Solar Cell Current–Voltage Characteristics in the Presence of Luminescent Coupling," *IEEE J. Photovoltaics*, vol. 3, no. 4, pp. 1429–1436, 2013.

[34] D. J. Friedman, J. F. Geisz, and M. a. Steiner, "Effect of Luminescent Coupling on the Optimal Design of Multijunction Solar Cells," *IEEE J. Photovoltaics*, vol. 4, no. 3, pp. 986–990, 2014.

[35] M. A. Steiner and J. F. Geisz, "Non-linear luminescent coupling in series-connected multijunction solar cells," *Appl. Phys. Lett.*, vol. 100, no. 25, p. 251106, 2012.

[36] M. A. Steiner, J. F. Geisz, T. E. Moriarty, R. M. France, W. E. McMahon, J. M. Olson, S. R. Kurtz, and D. J. Friedman, "Measuring IV Curves and Subcell Photocurrents in the Presence of Luminescent Coupling," *IEEE J. Photovoltaics*, vol. 3, no. 2, pp. 879–887, 2013.

[37] W. Guter, R. Kern, W. Kostler, T. Kubera, R. Lockenhoff, M. Meusel, M. Shirnow, G. Strobl, F. Dimroth, S. Kurtz, G. Sala, and A. W. Bett, "III-V Multijunction Solar Cells—New Lattice-Matched Products And Development Of Upright Metamorphic 3J Cells," *Proc. 7th Int. Conf. Conc. Photovolt. Syst.*, vol. 1407, pp. 5–8, 2011.

[38] R. R. King, D. Bhusari, D. Larrabee, X. Liu, E. Rehder, K. Edmondson, H. Cotal, R. K. Jones, J. H. Ermer, C. M. Fetzer, D. C. Law, and N. H. Karam, "Solar cell generations over 40 % efficiency," *Prog. Photovoltaics Res. Appl.*, vol. 20, pp. 801–815, 2012.

[39] S. Sze, "Physics of Semiconductor Devices," 2006.

[40] D. Abou-Ras, T. Kirchartz, and U. Rau, *Advanced Characterization Techniques for Thin Film Solar Cells*. 2011.

[41] M. Kasemann, B. Walter, T. Trupke, and W. Warta, "Shunt detection capabilities of luminescence imaging on silicon solar cells," *Proc.22nd EUPVSEC*, pp. 394–397, 2007.

[42] G. Smestad and H. Ries, "Luminescence and current-voltage characteristics of solar cells and optoelectronic devices," *Sol. Energy Mater. Sol. Cells*, vol. 25, no. 1–2, pp. 51–71, 1992.

[43] U. Rau, "Reciprocity relation between photovoltaic quantum efficiency and electroluminescent emission of solar cells," *Phys. Rev. B*, vol. 76, no. 8, p. 085303, 2007.

[44] N. Armani, G. Abagnale, M. Cornelli, G. Timò, E. Malvisi, F. Farina, G. Carbi, F. Rossi, F. Fabbri, and L. Nasi, "Low Growth Temperature MOCVD InGaP for Multi-junction Solar Cells," *Energy Procedia*, vol. 84, pp. 34–40, Dec. 2015.

[45] V. Paraskeva, C. Lazarou, M. Hadjipanayi, M. Norton, M. Pravettoni, G. E. Georghiou, M. Heilmann, and S. Christiansen, "Photoluminescence analysis of coupling effects: The impact of shunt resistance and temperature," *Sol. Energy Mater. Sol. Cells*, vol. 130, pp. 170–181, Nov. 2014.

[46] K. Kitahara, T. Ishii, J. Suzuki, T. Bessyo, and N. Watanabe, "Characterization of Defects and Stress in Polycrystalline Silicon Thin Films on Glass Substrates by Raman Microscopy," *Int. J. Spectrosc.*, vol. 2011, pp. 1–14, 2011.

[47] D. Lan, J. F. Geisz, M. a. Steiner, I. Garcia, D. J. Friedman, and M. a. Green, "Improved modeling of photoluminescent and electroluminescent coupling in multijunction solar cells," *Sol. Energy Mater. Sol. Cells*, vol. 143, pp. 48–51, Dec. 2015.

[48] D. Lan and M. A. Green, “Photoluminescent and electroluminescent couplings in monolithic tandem solar cells,” *Prog. Photovoltaics Res. Appl.*, vol. DOI:10.100, 2016.

[49] O. Breitenstein, J. Bauer, and J. P. Rakotoniaina, “Material-induced shunts in multicrystalline silicon solar cells,” *Semiconductors*, vol. 41, no. 4, pp. 440–443, 2007.

[50] O. Breitenstein, J. P. Rakotoniaina, M. H. Al Rifai, and M. Werner, “Shunt types in crystalline silicon solar cells,” *Prog. Photovoltaics Res. Appl.*, vol. 12, no. 7, pp. 529–538, 2004.

[51] M. Glatthaar, J. Haunschild, R. Zeidler, J. Rentsch, S. Rein, O. Breitenstein, and D. Hinken, “Luminescence imaging for quantitative solar cell material and process,” *Proc.25th EU Photovolt. Sol. Energy Conf. Exhib.*, pp. 1825–1827, 2010.

[52] M. de Kersauson, R. Jakomin, M. El Kurdi, G. Beaudoin, N. Zerounian, F. Aniel, S. Sauvage, I. Sagnes, and P. Boucaud, “Direct and indirect band gap room temperature electroluminescence of Ge diodes,” *J. Appl. Phys.*, vol. 108, no. 2, p. 023105, 2010.

[53] T. Kirchartz, U. Rau, M. Hermle, A. W. Bett, A. Helbig, and J. H. Werner, “Internal voltages in GaInP/GaInAs/Ge multijunction solar cells determined by electroluminescence measurements,” *Appl. Phys. Lett.*, vol. 92, no. 12, p. 123502, 2008.

[54] S. Roensch, R. Hoheisel, F. Dimroth, and A. W. Bett, “Subcell I-V characteristic analysis of GaInP/GaInAs/Ge solar cells using electroluminescence measurements,” *Appl. Phys. Lett.*, vol. 98, no. 25, p. 251113, 2011.

[55] R. Hoheisel, S. Messenger, D. Scheiman, and P. Jenkins, “Analysis of radiation hardness and subcell I-V characteristics of GaInP/GaAs/Ge solar cells using electroluminescence measurements,” *Proc.SPIE*, vol. 8256, 2012.

[56] V. Paraskeva, M. Hadjipanayi, G. Itskos, and G. E. Georghiou, “Electroluminescence and Photoluminescence Spectroscopy of qunatum well solar cells,” *Proc.28th EUPVSEC*, pp. 327–331, 2013.

[57] S. H. Lim, J. Li, C. R. Allen, and Y. Zhang, “Quantitative measurement and modeling of spondaneous emission efficiency of forward biased multi-junction solar cells,” *Proc.37th IEEE Photovoltaics Spec. Conf.*, pp. 1721–1725, 2011.

[58] M. A. Green, *Solar Cells: Operating Principles, Technology and System Applications*. 1998, p. 274.

[59] J.Nelson, “The physics of solar cells,” *Imp. Coll. Press*, 2003.

[60] A. Braun, B. Hirsch, A. Vossier, E. A. Katz, and J. M. Gordon, “Temperature dynamics of multijunction concentrator solar cells up to ultra-high irradiance,” *Prog. Photovoltaics Res. Appl.*, vol. 21, no. 2, pp. 202–208, 2013.

[61] C. Karcher, H. Helmers, M. Schachtner, F. Dimroth, and A. W. Bett, "Temperature-dependent electroluminescence and voltages of multi-junction solar cells," *Prog. Photovoltaics Res. Appl.*, vol. 22, no. 7, pp. 757–763, 2013.

[62] S. A. Lourenço, I. F. L. Dias, L. C. Poças, J. L. Duarte, J. B. B. de Oliveira, and J. C. Harmand, "Effect of temperature on the optical properties of GaAsSbN/GaAs single quantum wells grown by molecular-beam epitaxy," *J. Appl. Phys.*, vol. 93, no. 8, p. 4475, 2003.

[63] Y. P. Varshni, "Temperature dependence of the energy gap in semiconductors," *Phisica*, vol. 34, no. 1, pp. 149–154, 1967.

[64] A. W. Bett, B. Burger, F. Dimroth, and G. Siefer, "High-concentration PV using III-V solar cells," *Proc.4th IEEE World Conf. Photovolt. Energy Convers.*, vol. 1, pp. 615–620, 2006.

[65] S. Van Riesen, M. Neubauer, A. Boos, M. M. Rico, C. Gourdel, S. Wanka, R. Krause, P. Guernard, and A. Gombert, "New module design with 4-junction solar cells for high efficiencies," *Proc.AIP Conf.*, vol. 1679, p. 100006, 2015.

[66] M. Steiner, G. Siefer, T. Schmidt, M. Wiesenfarth, F. Dimroth, and A. W. Bett, "43 % Sunlight to Electricity Conversion Efficiency Using CPV," *IEEE J. Photovoltaics*, vol. 6, no. 4, pp. 1020–1024, 2016.

[67] M. Wiesenfarth, M. Steiner, J. Wolf, T. Schmidt, and A. W. Bett, "Investigation of different Fresnel lens designs and methods to determine the optical efficiency," *Proc. AIP Conf.*, vol. 97, no. 2014, pp. 97–101, 2014.

[68] G. Peharz and A. W. Bett, "High-Concentration Fresnel Lens Assemblies and Systems," 2010, pp. 331–335.

[69] T. Hornung and P. Nitz, "Light diffraction by concentrator Fresnel lenses," *Opt. Express*, vol. 1, no. May, pp. 686–704, 2014.

[70] T. Hornung, P. Kiefel, and P. Nitz, "The Distance Temperature Map as Method to Analyze the Optical Properties of Fresnel Lenses and their Interaction with Multi-Junction Solar Cells," *Proc. AIP Conf.*, vol. 1679, pp. 1–5, 2015.

[71] J. Jaus, P. Nitz, G. Peharz, G. Siefer, T. Schult, O. Wolf, M. Passig, T. Gandy, A. W. Bett, and F. Ise, "Second stage reflective and refractive optics for concentrator photovoltaics," *Proc.33rd IEEE Photovolt. Spec. Conf.*, pp. 1–5, 2008.

[72] Y. Jinshe and W. Mingyue, "Experimental research on photovoltaic module for asymetrical compound paravolic concentrator," *Proc. ISES World Cogress*, pp. 1561–1563, 2007.

[73] J. F. Geisz, D. J. Friedman, J. S. Ward, a. Duda, W. J. Olavarria, T. E. Moriarty, J. T. Kiehl, M. J. Romero, a. G. Norman, and K. M. Jones, "40.8% Efficient Inverted Triple-Junction Solar Cell With Two Independently Metamorphic Junctions," *Appl. Phys. Lett.*, vol. 93, no. 12, p. 123505, 2008.

[74] R. R. King, D. C. Law, K. M. Edmondson, C. M. Fetzer, G. S. Kinsey, H. Yoon, R. a. Sherif, and N. H. Karam, "40% efficient metamorphic GaInP/GaInAs/Ge multijunction solar cells," *Appl. Phys. Lett.*, vol. 90, no. 18, p. 183516, 2007.

[75] W. Guter, J. Schöne, S. P. Philipps, M. Steiner, G. Siefer, A. Wekkeli, E. Welser, E. Oliva, A. W. Bett, and F. Dimroth, "Current-matched triple-junction solar cell reaching 41.1% conversion efficiency under concentrated sunlight," *Appl. Phys. Lett.*, vol. 94, no. 22, p. 223504, 2009.

[76] J. M. Olson, S. R. Kurtz, a. E. Kibbler, and P. Faine, "A 27.3% efficient Ga0.5In0.5P/GaAs tandem solar cell," *Appl. Phys. Lett.*, vol. 56, no. 7, p. 623, 1990.

[77] J. F. Geisz, D. J. Friedman, J. Olson, and S. Kurtz, "1-eV solar cells with GaInNAs active laye," *J. Cryst. Growth*, vol. 195, p. 409, 1998.

[78] R. R. King, D. Bhusari, D. Larrabee, X. Liu, E. Rehder, K. Edmondson, H. Cotal, R. K. Jones, J. H. Ermer, C. M. Fetzer, D. C. Law, and N. H. Karam, "Solar cell generations over 40 % efficiency," *Prog. Photovoltaics Res. Appl.*, vol. 20, no. April, pp. 801–815, 2012.

[79] S. Nann and C. Riordan, "Solar spectral irradiance under overcast skies," *Proc. 21st IEEE Photovolt. Spec. Conf.*, vol. 2, pp. 1110–1115, 1990.

[80] F. Fabero and F. Chenlo, "Variance in the solar spectrum with the position of the receiver surface during the day for PV applications," *Proc. 22nd IEEE Photovolt. Spec. Conf.*, pp. 812–817, 1991.

APPENDICES

LIST OF PUBLICATIONS

[1] V.Paraskeva, M.Norton, M.Hadjipanayi, M.Pravettoni, G.E.Georghiou, "Voltage and light bias dependent quantum efficiency measurements of GaInP/GaInAs/Ge triple junction devices" Sol. Energy Mater. Sol. Cells vol. 116, pp. 55-60, 2013

[2]V.Paraskeva, C.Lazarou, M.Hadjipanayi, M.Norton, M. Pravettoni, G.E.Georghiou, M.Heilmann, S.Christiansen "Photoluminescence analysis of coupling effects: The impact of shunt resistance and temperature" Sol. Energy Mater. Sol. Cells vol. 130, pp. 170–181, 2014

[3] V.Paraskeva, M.Norton, M.Hadjipanayi, M. Pravettoni, G.E.Georghiou "Luminescent emission of multi-junction InGaP/InGaAs/Ge PV cells under high intensity irradiation" Sol. Energy Mater. Sol. Cells vol. 134, pp. 175–184, 2015

[4] V.Paraskeva, N.Armani, A.Malchiodi, F.Trespidi. G.Timo, and G.E.Georghiou "Coupling effects in InGaP/InGaAs/Ge triple junction PV cells of different structure" (submitted in IEEE Journal of Photovoltaics, 2016)

[5] M.Norton, V.Paraskeva, R.P.Kenny, G.E.Georghiou "Field investigation of the effect of spectral response upon photovoltaic energy yields" IEEE Journal of Photovoltaics vol. 6, pp. 739–745, 2016

[6] V.Paraskeva, M.Hadjipanayi, M.Norton, M. Pravettoni, G.E.Georghiou "The effect of shunt resistance on External Quantum Efficiency measurements at high light bias conditions" Proc. 40th IEEE Photovoltaic Specialist Conference (2014) pp.3664-3669

[7] M.Norton, V.Paraskeva, R.Galleano, G.Makrides, R.Kenny, G.E.Georghiou "High quality measurements of the solar spectrum for simulation of multi-junction photovoltaic cell yields" Proc. 29th EUPVSEC (2014) pp. 2002-2007

[8] V.Paraskeva, M.Norton, M.Hadjipanayi, G.E.Georghiou “Calibration of Spectroradiometers for Outdoor Direct Solar Spectral Irradiance Measurements” Proc 28th EUPVSEC (2013) pp.3466-3471

[9]V.Paraskeva, M.Hadjipanayi, G.Itskos, G.E.Georghiou "Electroluminescence and Photoluminescence Spectroscopy of Quantum Well Solar Cells" Proc. 28th EUPVSEC (2013) pp.327-331

[10] V.Paraskeva, M.Norton, M.Hadjipanayi, G.E.Georghiou “Electroluminescence and Spectral Photocurrent Response from Spectrally Tuned Quantum Well Solar Cells” Proc.27th EUPVSEC (2012) pp.397-402

[11] V.Paraskeva, M.Norton, A.Dobbin, T.Tibbits, S.Chonavel, G.E.Georgiou “On the Modelling and Evaluation of Spectrally Tuned Quantum Well Solar Cells: Initial Field Results” Proc.26thEUPVSEC(2011)pp.380-383